THERMOMECHANICS OF SHAPE MEMORY POLYMERS AND COMPOSITES

by

Qi Ge

B. Sc., Tongji Univeristy, China, 2006

M. Sc. Zhejiang Univerity, China, 2008

A thesis submitted to the

Faculty of the Graduate School of the

University of Colorado in partial fulfillment

of the requirement for the degree of

Doctor of Philosophy

Department of Mechanical Engineering

2012

This thesis entitled:
Thermomechanics of Shape Memory Polymers and Composites
written by Qi Ge
has been approved for the Department of Mechanical Engineering

H. Jerry Qi

Martin L. Dunn

Date

The final copy of this thesis has been examined by the signatories, and we
Find that both the content and the form meet acceptable presentation standards
Of scholarly work in the above mentioned discipline.

Ge, Qi (Ph.D., Mechanical Engineering)

Thermomechanics of Shape Memory Polymers and Composites

Thesis directed by Associate Professor H. Jerry Qi and Professor Martin L. Dunn

This dissertation presents studies with a combination of experiment, theory, and simulation on a broad range of polymeric material systems (both established and emerging), that exhibit the shape memory (SM) effect. The goals of the studies are to understand complex thermomechanical behaviors of shape memory polymers (SMPs), develop constitutive models to describe the behaviors and use the developed models to advance the development and deployment of SMPs. The general approach used in the studies is independent of the material system and consists of: i) sample fabrication and thermomechanical experiments including dynamic mechanical analysis (DMA), stress-strain behaviors and thermal strain tests; ii) development of micromechanics-inspired constitutive models incorporate large deformation and anisotropy; iii) comparison of experiment and theory and parametric studies. The studies have resulted in many major/key findings: a) for shape memory elastomeric composites (SMECs) consisting of elastomeric matrix and crystallizable fibers, a sophisticated thermomechanical constitutive was developed to describe the shape memory behaviors based on the melt-crystal transition of the fibers. b) For triple shape polymeric composites (TSPCs) consisting amorphous SMP based matrix and crystallizable fibers, a constitutive model separately considering the glassy transition of the matrix and the melt-crystal transition of fibers, was developed to describe triple shape memory behaviors of the composites. c) For printed shape memory composites (PSMCs), the fabrication approach for anisotropic shape memory elastomeric composites (ASMECs) was developed. A thermomechanical constitutive model was also built to describe the fiber orientation dependent shape memory behaviors.

CONTENTS

APPENDIX

CHAPTER I

INTRODUCTION

1.1 Background

Environmental activated shape memory polymers (SMPs) have been investigated intensively because of their capability to recover a large predeformed shape in response to an environmental stimulus, such as heat (Lendlein and Kelch, 2002, 2005, Liu, et al., 2007, Xie, 2010), light (Jiang, et al., 2006, Koerner, et al., 2004, Lendlein, et al., 2005, Li, et al., 2003, Scott, et al., 2006, Scott, et al., 2005), moisture (Huang, et al., 2005), magnetic field (Mohr, et al., 2006) etc. Compared with shape memory alloys, SMPs is of low density, inexpensive to fabricate and able to exhibit larger deformation in excess of 1100% (Lendlein and Kelch, 2002, 2005). These advantages allow SMPs to be used in many applications such as microsystem actuation components, recoverable surface patterns, biomedical devices, aerospace deployable structure, and morphing structures (Lendlein and Kelch, 2002, 2005, Liu, et al., 2006, Liu, et al., 2004, Thomas and Lendlein, 2002, Tobushi,Hara, et al., 1996, Williams, et al., 1955, Yakacki, et al., 2007).

For environmental activated SMPs, the mechanism can be either chemical or physical. For example, for the photo-induced SMPs, the shape memory (SM) effects are mostly achieved by changing chemical structure to create or eliminate additional crosslinking under certain wavelength UV irradiations (Jiang, et al., 2006, Koerner, et al., 2004, Lendlein, et al., 2005, Li, et al., 2003, Scott, et al., 2006, Scott, et al., 2005); for the water driven SMPs, water absorbed in SMPs binds the polymer and weakens the hydrogen bonding, leading the significant decrease of glass transition temperature (Huang, et al., 2005); for the SMPs activated by magnetic field, the SM effect is realized by incorporating magnetic nanoparticle in SMPs and inductive heating of these compounds in alternating magnetic fields (Mohr, et al., 2006). The latter two cases are considered as indirect thermally activated behaviors. Compared to other environmental activated

SMPs, the thermally triggered SMPs are the primary focus in the SMP research field and the most widely used and investigated (Yakacki, et al., 2007).

1.2 One-way and two-way shape memory effects

For thermally activated SMPs, a typical four-step SM cycle is used to achieve the SM behavior as shown in Fig. 1: At Step 1 (S1), the SM cycle is initiated by deforming the material at a temperature T_H, where $T_H > T_{trans}$ and T_{trans} can be glass transition temperature, crystallization temperature or other phase transition temperatures. Then at Step 2 (S2), the material is cooled down to a temperature $T_L < T_{trans}$ while maintaining the load causing the initial deformation. At Step 3 (S3), the programmed shape is fixed after unloading at T_L. At Step 4 (S4), the SM effect is activated by increasing the temperature above T_{trans} and the initial shape is recovered by heating back to T_H. It is pointed out that once the material recovers, it requires an additional programming step for any further recovery. Therefore, this is referred to as a one-way shape memory (1W-SM) effect.

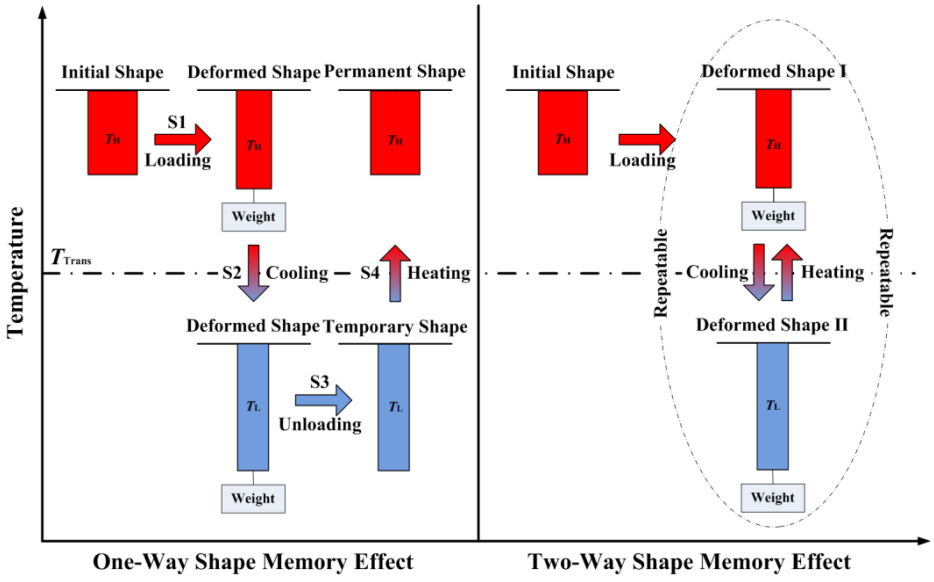

Fig. 1 Schematic showing difference between the one-way and two-way shape memory effects.

The significant drawback of 1W-SM effects is the SM cycle is not repeatable: one more programming step is required to exhibit another SM cycle, which would be restricted in some applications. Recently, the SMP with the capability of exhibiting the two-way shape memory (2W-SM) effect was developed (Chung, et al., 2008). For the 2W-SM behavior, as shown in Fig. 1, the material is deformed (deformed shape I) under a constant weight at T_H; then cooling to T_L with the same load, the stretch increase due to phase transition such as stretch induced crystallization (SIC), the material reaches a new deformed state (deformed shape II). Once it is heated back to T_H under the constant weight, the material recovers to the deformed shape I. The process is repeatable to switch deformed shape I and II by cooling to T_L or heating to T_H, as long as the constant load is on.

1.3 Tripe shape memory effect

SMPs capable of fixing one temporary shape are referred to as dual-shape SMPs. Recently, the triple-shape SMPs were developed, which are able to fix two temporary shapes and recover sequentially from one temporary shape to the other, and ultimately to the permanent shape under heating (Bellin, et al., 2006, Bellin, et al., 2007, Luo and Mather, 2010). Fig. 2 illustrates steps to achieve the tripe-shape SM effects: At Step 1 (S1), the sample is initially deformed at a temperature T_H, where T_H is higher than $T_{trans\,I}$ and $T_{trans\,II}$. Then at Step 2 (S2), the temperature is decreased to T_{L1}, while maintaining the load leading the initial deformation. At Step 3 (S3), the first temporary shape is fixed at T_{L1}. At Step 4 (S4), the sample is deformed differently from S1 at T_{L1}. At Step 5 (S5), the material is cooled to T_{L2}, while maintaining the load causing the deformation at S4. At Step 6 (S6), after unloading, the second temporary shape is

fixed at T_{L2}. At Step 7 (S7), as heating back to T_{L1}, the material recovers to its first temporary shape. At Step 8 (S8), the material returns into its permanent shape by heating to T_H.

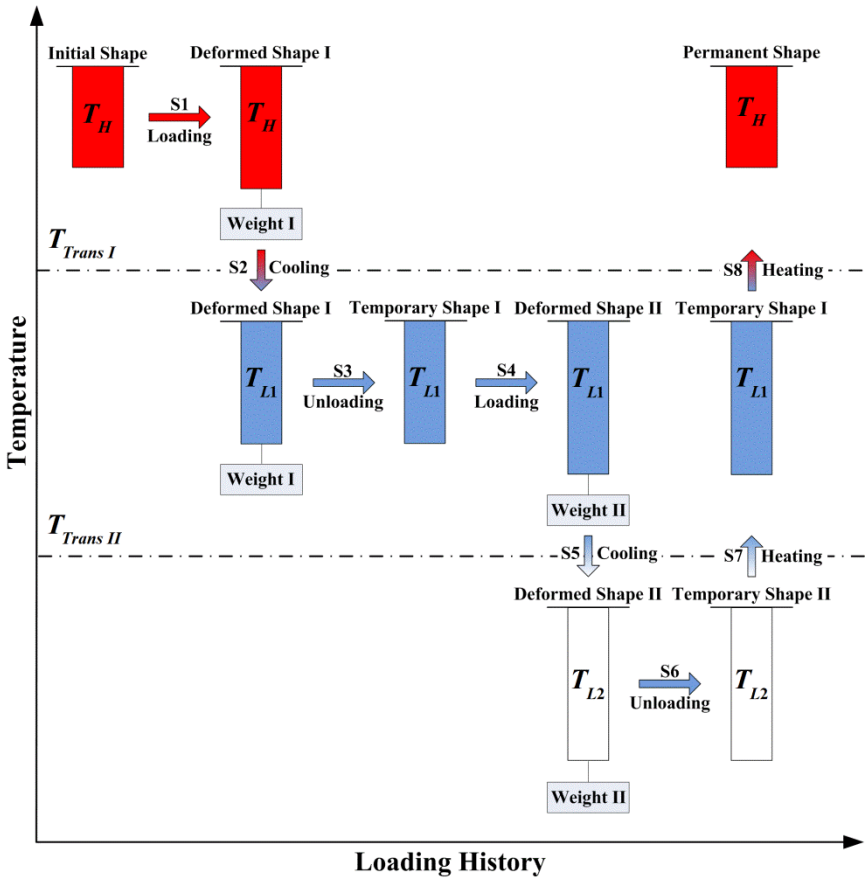

Fig. 2 Schematics of steps to achieve the triple-shape SM effect.

1.4 Fabrications for shape memory composites

In thermal activated SMPs, the most common mechanism is the second order transition from the rubbery state to the glassy state (Nguyen, et al., 2008, Qi, et al., 2008a), which is accompanied by a large change in material modulus from a few MPa to a few GPa. This large change in modulus offers the advantage of easy programming as the temporary shape is formed by deforming the material at a high temperature where the material modulus is low. However, in

some applications, especially in biomedical applications such as biomimetic sensing and actuation, soft materials are desirable. Recently, Luo and Mather (2009) reported a novel approach to develop a shape memory elastomeric composite (SMEC) by embedding a crystallizable thermoplastic fiber network into an elastomeric matrix (Luo and Mather, 2009). In the SMEC system the elastomeric matrix provides rubber elasticity, while the fiber network serves as a reversible "switch phase" for shape fixing and recovery through the crystal-melt transition.

Recently, based on the fabrication of shape memory elastomeric composites (SMECs) (Luo and Mather, 2009), Luo and Mather (Luo and Mather, 2010) introduced a new and broadly applicable method for designing and fabricating triple shape polymeric composites (TSPCs) with well controlled properties. In the TSPC, an amorphous SMP (epoxy with $T_g \approx 20$ °C – 40 ℃, depending on the precise composition) works as the matrix providing overall elasticity and provides one phase transition temperature and non-woven PCL (poly(ε-caprolactone)) microfibers produced by electrospinning and incorporated into the matrix provides the other phase transition temperature due to the crystal-melt transition of PCL ($T_m \approx 50$ °C). Compared with methods reported previously, the approach for fabricating polymeric composites is quite flexible, since one can tune the functional components separately to optimize material properties, opening up the potential to design for a variety of applications (Luo and Mather, 2010).

A natural paradigm for SMECs is then to control the shape memory behavior via the architecture of the fibers; indeed Mather et al. has demonstrated anisotropic shape memory behavior by creating composites with aligned electrospun fibers embedded in an elastomeric matrix. Instead of fabricating composites through electrospinning, we pursue the general idea of control of macroscopic shape memory behavior via control of the composite architecture by introducing a new paradigm enabled by recent advances in digital manufacturing of multimaterial architectures – printed shape memory composites (pSMCs). We present a method based on three-

dimension (3D) printing technique to fabricate composite materials with precisely-controlled fiber architectures that lead to complex, anisotropic shape memory behavior. Using the 3D printing technique, a kind of pSMC laminas referred to as anisotropic shape memory elastomeric composites were fabricated, which consists of an elastomeric matrix and oriented PCL fibers that undergo a melt-crystallization phase transformation during heating or cooling, and exhibits anisotropic mechanical properties and shape memory behaviors. The 3D printing technique can be used to fabricate pSMC laminates with much more complex, but highly-tailorable, behavior.

1.5 Models for shape memory polymers

In the design of SMP applications, theoretical models are desired to predict the SM behaviors. In the past, several models were developed. For example, 1D model by Liu et al (Liu, et al., 2006), 3D finite deformation model by Qi et al (Qi, et al., 2008a)and a constitutive theory by Chen et al (Chen and Lagoudas, 2008a, b) for SMPs. These models attribute the SM effect to the formation of phases during cooling which serve to lock the temporary shape and the loss of the phases during heating recover the permanent shape, and only consider phenomenological for amorphous SMPs but no physical meanings. In amorphous SMPs, the SM effect is due to the glass transition where the shape deformed at high temperatures can be fixed at low temperatures as chain mobility decreasing dramatically and the material enters the nonequilibrium state (glassy state). Several models were developed based on this concept and include the early model by Tobushi (Tobushi,Hara, et al., 1996) and recent models by Nguyen et al. (Nguyen, et al., 2008) and Castro et al. (Castro, et al., 2010). In semi-crystalline SMPs, the mechanism of SM effect is due to the crystallization of amorphous phases, and the shape deformed at high temperatures is fixed at low temperatures where crystalline phases formed and serve as crosslinks to lock the temporary shape. Several models (Barot, et al., 2008, Ma and Negahban, 1995a, Ma and Negahban, 1995b, Negahban, 1993, Negahban, et al., 1993, Westbrook,Parakh, et al., 2010) were developed. For detailed descriptions of kinetics for non-isothermal crystallization and melting, for

the triple-shape memory effect with dual transition temperatures and for SMPs exhibiting anisotropic shape memory behaviors, to the author's best knowledge, none models have been reported to data.

1.6 The objective of this dissertation

The objective of my research is to develop rigorous experiment-verified models to describe thermo-mechanical phenomena in new emerging shape memory polymers and composites. The general approach used in the studies is independent of the material system and consists of: i) sample fabrication and thermomechanical experiments including dynamic mechanical analysis (DMA), stress-strain behaviors and thermal strain tests; ii) development of micromechanics-inspired constitutive models incorporate large deformation and anisotropy; iii) comparison of experiment and theory and parametric studies. The studies have resulted in many major/key findings: a) for shape memory elastomeric composites (SMECs) consisting of elastomeric matrix and crystallizable fibers, a sophisticated thermomechanical constitutive was developed to describe the shape memory behaviors based on the melt-crystal transition of the fibers. b) For triple shape polymeric composites (TSPCs) consisting amorphous SMP based matrix and crystallizable fibers, a constitutive model separately considering the glassy transition of the matrix and the melt-crystal transition of fibers, was developed to describe triple shape memory behaviors of the composites. c) For printed shape memory composites (PSMCs), the fabrication approach for anisotropic shape memory elastomeric composites (ASMECs) was developed. A thermomechanical constitutive model was also built to describe the fiber orientation dependent shape memory behaviors.

This dissertation primarily introduces the studies of the different shape memory composites. In Chapter 2, we discuss the thermomechanical behaviors of SMEC. In the chapter, experiments of material properties and characterization of SM behaviors are introduced, a three dimensional (3D) thermomechanical constitutive model with kinetics of non-isothermal

crystallization and melting is developed and results are presented by treating both matrix and fiber crystals as incompressible neo-Hookean materials. In Chapter 3, the thermomechanical behaviors of TSPC is presented, including experiments for mechanical and thermal responses, characterization of triple SM behaviors, a one dimensional (1D) thermomechanical constitutive model with glass transition of the matrix and crystal-melt transition of fiber network, and analysis of stress distribution on components of the TSPC. Chapter 4 introduces the fabrication process, anisotropic thermomechanical properties and anisotropic shape memory behaviors for ASMECs. A 3D anisotropic thermomechanical constitutive model was developed to capture the anisotropic shape memory behaviors. In appendix, we also introduce a simplified model for prediction of temperature-dependent free recovery behaviors of amorphous SMPs and a theoretical model for the two-way shape memory composite actuator.

CHAPTER II

SHAPE MEMORY ELASTOMERIC COMPOSITE (SMEC)

2.1 Introduction

In SMPs triggered by temperatures, the undeformed sample is heated to $T_H > T_{trans}$, deformed to the desired shape, and then cooled to $T_L < T_{trans}$. After unloading at T_L, the sample is fixed into the temporary shape. Heating back to T_H deploys the sample and recovers to the permanent shape. The most common mechanism in thermally triggered SMP is the second order transition from the rubbery state to the glassy state (Nguyen, et al., 2008, Qi, et al., 2008b), which is accompanied by a large change in material modulus from a few MPa to a few GPa. This large change in modulus offers the advantage of easy programming as the temporary shape is formed by deforming the material at a high temperature where the material modulus is low. However, in some applications, especially in biomedical applications such as biomimetic sensing and actuation, soft materials are desirable. Recently, several attempts have been made to create new soft and elastomeric SMPs. Rousseau and Mather (2003) developed a smectic-C liquid crystalline elastomer (LCE) exhibiting the shape memory effects based on the smectic-C-to-isotropic transition of the LCE (Ingrid A. Rousseau and Patrick T. Mather, 2003); Weiss et al (2008) introduced a new type of SMP consisting of an elastomeric ionomer and low mass fatty acids (FA) or their salts, where ionomer provided a strong intermolecular bond between the FA crystal and the polymer, and FA was used to produce secondary network, where T_{trans} was related to the melting point of the FA (Weiss, et al., 2008). However, these two materials involves some custom synthesis, which presents an inherent challenge for large scale production (Luo and Mather, 2009).

Recently, Luo and Mather (2009) reported a novel approach to develop a shape memory elastomeric composite (SMEC) by embedding a crystallizable thermoplastic fiber network into an elastomeric matrix (Luo and Mather, 2009). In the approach by Luo and Mather (2009), a poly (ε-

caprolactone) (PCL; M_w = 65000g/mol, Sigma-Aldrich, St Louis, MO), is first electrospun into a fiber network (or mat). This fiber network is then immersed into a silicone rubber (Sylgard 184, Dow Corning Corp., Midland, MI) pre-polymer solution, which is then chemically crosslinked to produce a SMEC system: Sylgard serves as an elastomeric matrix and provides rubber elasticity, while the PCL fiber serves as a reversible "switching phase" for shape fixing and recovery through the crystal-melt transition. In a thermo-mechanical cycle, the SMEC is heated to $T_H > T_{trans}$ (T_{trans} is T_m , the melting temperature of PCL), deformed at T_H , then cooled to $T_L < T_{trans}$ while maintaining the external load. During cooling, PCL undergoes a phase change from a polymer melt to a semicrystalline polymer. After unloading at T_L , the temporary shape is fixed due to the crystallized PCL. Heating back to T_H , where PCL melts and the stress stored in semicrystalline PCL is released, the SMEC recovers its permanent shape. Meanwhile, during the same SM cycle, Sylgard behaves as an elastomer with its entropic elastic modulus proportional to the temperature. Because the operational temperatures for a SM cycle are much higher than the glass transition temperatures for Sylgard and PCL, the modulus of SMEC is a few MPa at $T_H > T_{trans}$ and ~10 MPa at $T_L < T_{trans}$.

The approach developed by Luo and Mather for Sylgard/PCL SMEC provides a paradigm for developing a wide array of smart polymer composites with different chemistries that utilize melt-crystal transition in polymers to achieve the shape memory effect. It is therefore important to understand the thermo-mechanical behaviors and to develop corresponding material models. In this paper, a three-dimension (3D) constitutive model is developed to describe the shape memory behavior of the novel SMECs. This model includes a kinetic description of non-isothermal crystallization and melting. The assumption that the newly formed crystalline phase is in an undeformed state is used to track the kinematics of evolving phases. In order to improve the computational efficiency, the effective phase model (EPM) developed by the authors is adopted.

2.2 Materials and experiments

2.2.1 Materials

The SMEC was prepared using a silicone rubber (Sylgard 184, Dow Corning Corp., Midland, MI) as the elastomeric matrix and a poly (ε-caprolactone) (PCL; M_w = 65000g/mol, Sigma-Aldrich, St Louis, MO) as fiber reinforcements . A two-step process in Luo and Mather (Luo and Mather, 2009) was followed: PCL was first electrospun from a 15 wt% chloroform/DMF (volume ratio=8:2) solution. The resulting nonwoven fiber mat was then immersed in a two-part mixture of Sylgard 184 (base: agent mixing ratio = 10:1) and in order to ensure complete infiltration of Sylgard 184 into the PCL fiber mat, vacuum-assisted infiltration process was conducted. After removing the excess Sylgard 184 resin on the surface, the infiltrated Sylgard/PCL was cured at room temperature for more than 48 hours. The morphology of the Sylgard/PCL SMEC was studied by scanning electron microscopy (SEM). The surfaces of the as-spun PCL fiber mat (Fig. 3a) and Sylgard/PCL composite (Fig. 3b) clearly show that the infiltration was complete with all the original voids occupied by Sylgard 184, while the fiber structures were preserved. More details about the material sample preparation were described in Luo and Mather (2009)

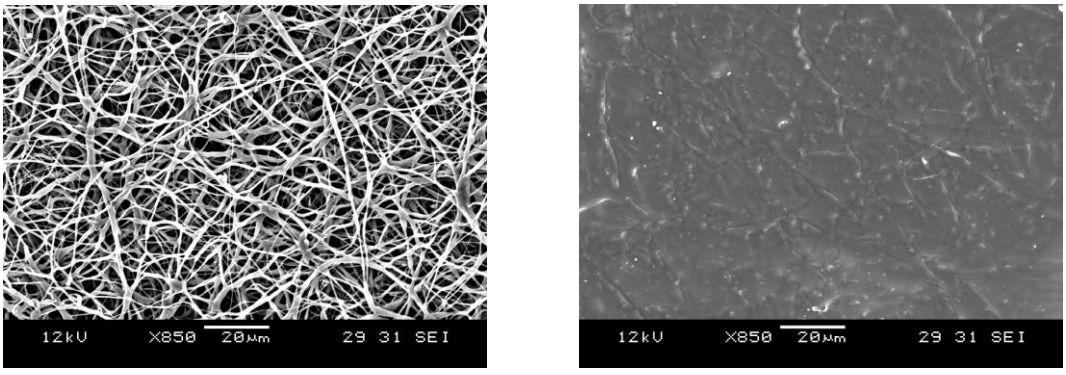

(a) (b)

Fig. 3 Scanning electron microscope (SEM) images showing: (a) the surface of as-spun PCL fiber mat (fiber diameter =0.69±0.36µm); (b) The surface of Sylgard/PCL composite. (Luo and Mather, 2009)

2.2.2 DMA experiments

DMA test was conducted using a dynamic mechanical analyzer (Q800 DMA, TA Instruments). The Sylgard/PCL SMEC (a 13.86×2.7×0.68mm rectangular film) was loaded by a dynamic tensile load at 1Hz and the temperature was lowered at a rate of 2 ℃/min from 120 ℃ to -145 ℃. Fig. 4a and b show the tensile storage modulus and tensile loss tangent tanδ of SMEC and neat Sylgard, respectively. The transition temperatures were determined by the peaks of tanδ. For the neat Sylgard, there are two distinct transitions observed in the given temperature range, which are attributed to the glass transition ($T_g^{Syl} = -127.2°C$) and the melt-crystal transition ($T_c^{Syl} = -65.9°C$) (Clarson, et al., 1985, Mark, 1999). In contrast, the SMEC has four transitions: the glass transition of Sylgard ($T_g^{Syl} = -127.2°C$), the melt-crystal transition of Sylgard ($T_c^{Syl} = -65.9°C$), the glass transition of PCL ($T_g^{PCL} = -49.5°C$) and the melt-crystal transition of PCL ($T_c^{PCL} = 27.2°C$). Since the melt-crystal transition of Sylgard (-65.9 ℃) and the glass transition of PCL (-49.5 ℃) are very close, there is just one obvious peak of tanδ of SMEC observed around -50 ℃. At the temperature of 5 ℃, the SMEC has a storage modulus of 12.7MPa and a low tanδ value of 0.06, indicating that the material is soft and has low viscosity. The storage modulus of the composite drops to 1.4MPa at 80 ℃ (above the melting temperature of PCL), which is lower than that of neat Sylgard (3.16MPa) at this same temperature.

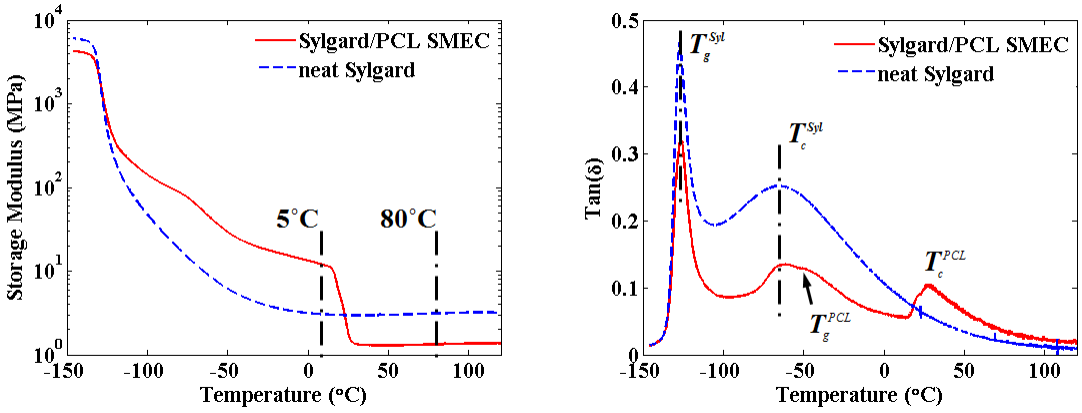

(a) (b)

Fig. 4 Dynamic Mechanical Analysis (DMA) of the Sylgard/PCL SMEC and neat Sylgard: (a) Storage modulus and (b) tanδ as functions of temperature.

2.2.3 Shape memory behavior

To exhibit the SM behavior, the Sylgard/PCL SMEC undergoes a four-step thermo-mechanical loading-unloading cycle, as illustrated in Fig. 5. In Step 1 (S1), the SMEC is isothermally predeformed (stretched in this paper) at $T_H > T_m$ (the melting temperature of PCL). Step 2 (S2) cools the material to $T_L > T_c$ (the crystallization temperature of PCL) whilst the stretching force is maintained to be a constant. After unloading (Step 3, S3), the SMEC is fixed at (or programmed to) the temporary shape at T_L. The SMEC can maintain this shape as long as the temperature does not change. In the final step (Step 4, S4), the SM effect is activated by raising temperature to T_H and the initial shape is recovered.

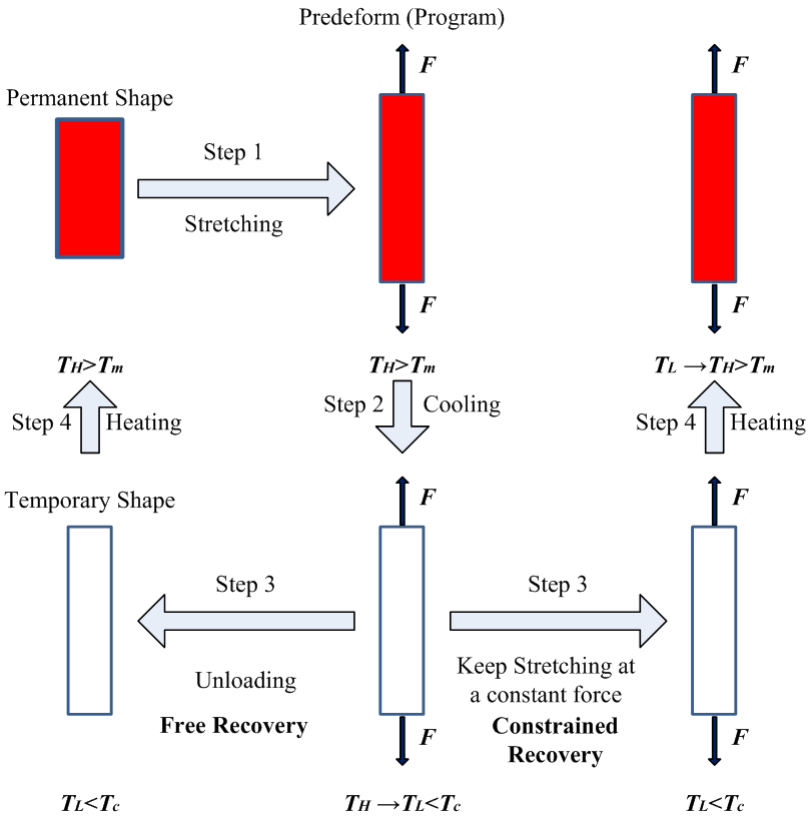

Fig. 5 The schematics of the free/constrained recovery experiment. The left-side part shows the thermo-mechanical loading-unloading cycle for free recovery. The right-side part shows the constrained recovery cycle.

The SM behaviors of the Sylgard/PCL SMEC were investigated on the DMA machine. They are shown in stress-temperature-strain (Fig. 6a) and strain-temperature plots (Fig. 6b), under three different imposed nominal stresses (0.1MPa, 0.15MPa, 0.2MPa). In S1, the sample was stretched at 80 ℃ (T_H) by gradually ramping the tensile stress at a loading rate 0.1MPa/min to the predefined value (0.1MPa, 0.15MPa, and 0.2MPa in three different cases, respectively). In S2, the temperature was decreased to 5 ℃ (T_L) at a rate of 2 ℃/min while the nominal stress was fixed. Fig 6a and b show, when lowering the temperature, the strain initially increased for 0.15MPa, and 0.2MPa cases, while decreased for the 0.1MPa case. At the temperature around 30 ℃, the strain dropped by ~1% due to crystallization of PCL. In S3, the stress was quickly released at 5 ℃. Here, whilst most of the deformation was fixed, a slight contraction of the sample can be observed. In S4, the unconstrained strain recovery was triggered by heating back to 80 ℃ at a rate of 2 ℃/min.

In order to further qualify the SM behavior, the fixing ratio R_f and the recovery ratio R_r are used as following (Luo and Mather, 2009, Rousseau, 2008):

$$R_f = \frac{\varepsilon_u}{\varepsilon_m} \times 100\%,\ R_r = \frac{\varepsilon_u - \varepsilon_p}{\varepsilon_u - \varepsilon_0} \times 100\%, \quad (1)$$

where ε_m and ε_u are the strains before and after unloading at T_L, ε_p is the permanent strain after heat induced recovery and ε_0 is initial strain at T_H. The calculated R_f and R_r are listed in Table 1 for the three different imposed nominal stress cases. As shown in Table 1, the recovery ratios R_r for the three cases are very high (>98%), indicating that the material has a high capability of recovery to the initial shape. On the other hand, the fixing ratios R_f are ~80%, which is lower than these (>97%) reported by Luo and Mather (Luo and Mather, 2009). In fact, the fixity of SMEC can be tuned by changing the Sylgard/PCL composition. This will be discussed later.

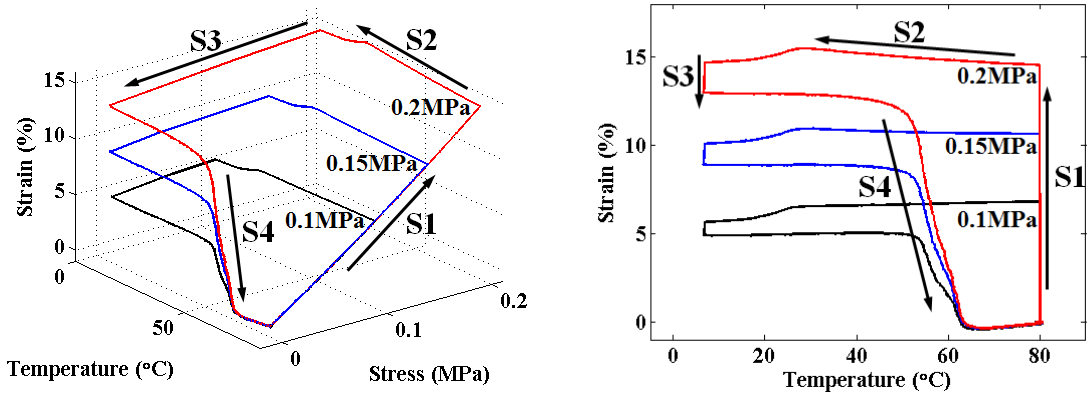

(a) (b)

Fig. 6 Shape memory behaviors of Sylgard/PCL SMEC with different imposed stresses: (a) Stress-Temperature-Strain plot showing the 3D shape memory cycles. (b) Strain-Temperature plot.

Table1. List of R_f and R_r

	0.1MPa	0.15MPa	0.2MPa
R_f	84.0%	88.4%	88.8%
R_r	98.2%	99.2%	99.7%

The constrained recovery experiment (schematically shown in Fig. 5) was also conducted. The sample was isothermally stretched (S1) at T_H, cooled (S2) to T_L, finally heated back (S4) to T_H. During cooling and heating, the external load was maintained. Note that the only difference between free recovery and constrained recovery is that the constrained recovery does not have the unloading step (S3). Fig. 7a and b show the results of the constrained recovery experiment with the imposed nominal stress 0.15MPa. In S1, the sample was first stretched at 80℃ (T_H) by gradually ramping the tensile stress to 0.15MPa. At S2, the temperature was decreased to 5℃ (T_L) at a rate of 2℃/min while the stress was fixed as a constant. In S4, the stretched sample was heated back to 80℃ at a rate of 2℃/min. The strain increased initially when increasing temperature. At about 60℃, the strain decreased with increasing temperature. At 80℃, the sample was recovered to the stretched shape in S1. In Fig. 7b, comparing S2 and S4, the crystallization of PCL started about 20℃ lower than its melting, which was due to the hysteresis in crystallization and melting of polymers.

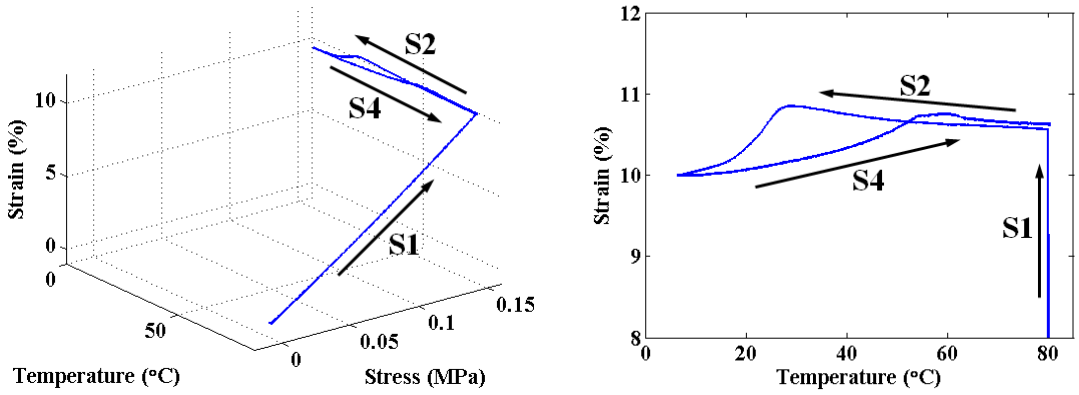

(a) (b)

Fig. 7 The constrained recovery of Sylgard/PCL SMEC: (a) Stress-Temperature-Strain plot. (b) Strain-Temperature plot.

2.2.4 Thermal contraction/expansion experiment

The thermal contraction/expansion test (Fig. 4a) was conducted using the DMA machine. A small stretching force (1×10^{-4}N) was applied to ensure the sample was straight. Temperature was decreased from 80 ℃ to -10 ℃ with the rate of 2 ℃/min and heating back to 80 ℃ with the same rate. In Fig. 4, the material first contracted linearly with coefficient of thermal expansion (CTE) 2.66×10^{-4}/ ℃, and then dropped by about 1% at a temperature range from about 25 ℃ to 15 ℃. After the nonlinear dropping, the material contract with a low CTE 1.57×10^{-4}/ ℃. The thermal strain at 5 ℃ is -2.11%, which will be used for parameter fitting. When heating back from -10 ℃ to 80 ℃, the material expanded roughly linearly and then ascended abruptly about 1% due to melting at a narrow temperature range from about 50 ℃ to 60 ℃. After melting finished, the material expanded almost linearly and closed the loop.

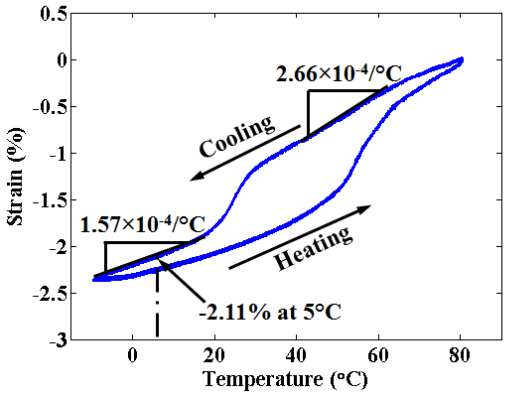

Fig. 8 The experimental result of the thermal contraction/expansion test.

2.2.5 Effects of thermal rates

In order to investigate the effect of thermal rates on SM behaviors, four different thermal rates (1 ℃/min, 2 ℃/min, 5 ℃/min and 10 ℃/min) with a 0.15MPa nominal stress were applied to free recovery experiments (Fig. 9a and b). In a previous study (Westbrook,Castro, et al., 2010), it was found that the main factors affecting the temperature distribution within the sample are the size of the sample and the contact between the sample and fixture. For a cylindrical sample (10mm in diameter and height) with improved fixture design, the maximum

temperature difference within the sample is 5.3 ℃ for a thermal rate of 10 ℃/min). Since the sample used in this paper is a thin film under a tensile testing setup, we expect that the temperature difference within the sample is very small. For the 1 ℃/min case and 2 ℃/min case, the curves show similar trend and about 90% of deformation can be fixed after unloading. For the 5 ℃/min case and 10 ℃/min case, because the crystallization did not finish completely, the 5 ℃/min case just held about 60% temporary shape and the 10 ℃/min case just fixed about 40% (Fig. 9b).

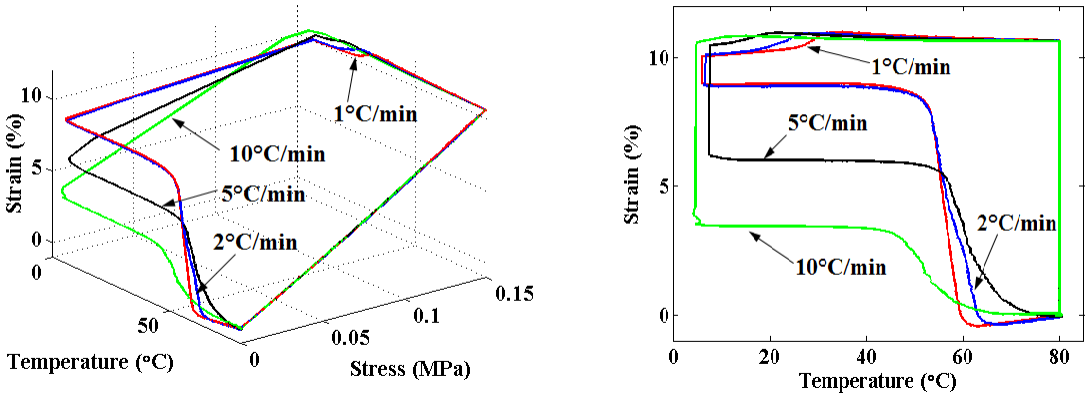

(a) (b)

Fig. 9 Shape memory behavior with different thermal rates (1 ℃/min (red), 2 ℃/min (blue), 5 ℃/min (black) and 10 ℃/min (green)): (a) Stress-Temperature-Strain plot. (b) Strain-Temperature plot.

2.3 Model description

2.3.1 Overall model

In this section, a continuum thermo-mechanical constitutive model frame for the Sylgard/PCL SMEC is developed by treating matrix and fiber network as a homogenized system of multiple phases. The matrix is taken as a conventional elastomer and the fiber network is taken to be an aggregate of melt and crystalline regions; it is a melt at high temperature and is an elastic solid at low temperatures. The evolution of the fiber aggregate is described by existing theories of crystallization. The goal is to develop a modeling approach for this class of materials. At this

point, some levels of detailed understanding are sacrificed in favor of a simple way to describe the complex thermo-mechanical phenomena and therefore several assumptions are made:

(i) Since PCL melts behave like liquids, it can only carry hydraulic pressure under compressive conditions. In addition, since the PCL sits an interconnected network, some PCL may leak out of the SMEC under hydraulic pressure. To simplify the model, we assume that PCL do not carry loads in its melting state. Future studies should consider the load carrying capability of PCL melts.

(ii) Since the melting temperature of PCL is much higher than its glass transition temperature, the relaxation time of PCL melts is fast at the temperature near its melting temperature. Therefore, it is assumed that the external loading does not affect the morphology of PCL crystals.

(iii) During crystallization, PCL crystals are formed in a stress-free (natural) configuration (Rajagopal and Srinivasa, 1998a, b). PCL crystals formed at different times have different deformation history.

(iv) During crystallization, the deformation transfer is simplified by an averaging scheme that assumes both Sylgard and PCL crystals will undergo a small deformation increment.

(v) Since deformation on PCL crystals are limited (~1% tensile at S2 and ~1% compressive at S3) in a shape memory cycle, inelastic deformation of PCL crystals is not considered.

(vi) Considering microstructure of the Sylgard/PCL system, the concept of stress concentration factors is introduced. For the sake of simplicity, stress concentration factors are assumed to be constants.

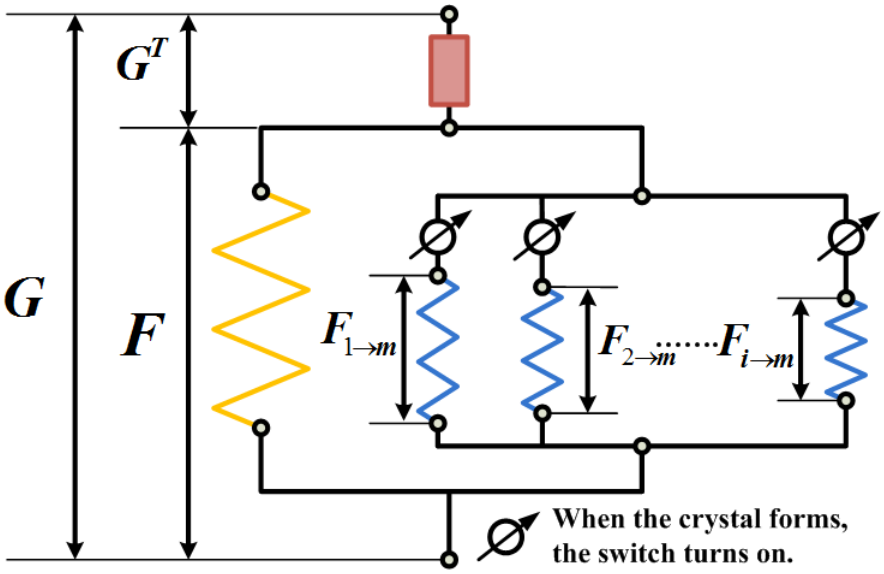

Fig. 10 1D analogy of the constitutive model for the Sylgard/PCL SMEC: The block on the top represents the thermal stretch due to thermal expansion and contraction. The left spring represents Sylgard matrix as an elastomer with modulus NkT. The right multiple springs represents PCL crystals formed at different time. When PCL crystallized, the switch turns on and PCL with modulus μ; when PCL melted, the switch turns off and modulus of PCL is negligible.

The model decomposes the deformation of the material into thermal deformation and mechanical deformation (as shown in Fig. 10):

$$\mathbf{G}=\mathbf{G}^M\mathbf{G}^T=\mathbf{F}\mathbf{G}^T,\mathbf{F}=\mathbf{G}^M, \tag{2}$$

where G is the total deformation gradient, G^M is the mechanical deformation gradient and gives rise to stress, G^T is the deformation gradient due to thermal expansion. For the convenience of model description, we set $\mathbf{F}=\mathbf{G}^M$ and use F to represent mechanical deformation gradient. The mechanical contribution from Sylgard matrix is represented by a hyperelastic spring in Fig. 10, because it is always in the rubbery state with a low tanδ (=0.06) during the temperature cycle. The PCL network changes its crystallinity with temperature: When $T>T_m$, PCL melts do not carry load; when $T<T_c$, PCL crystallizes and can carry load. Since crystallization of PCL is a continuous and time dependent process, we further divide PCL crystals into small phases formed at different times with volume fraction Δv_i^c with a deformation gradient of $\mathbf{F}_{i\to m}$. More details will be described in the next section of the 3D generalized theory.

For the Sylgard/PCL system, the simplest model arranges stresses on Sylgard and PCL in parallel (as shown in Fig. 10) and the total Cauchy stress $\boldsymbol{\sigma}^{total}$ is given by:

$$\boldsymbol{\sigma}^{total} = v_{Syl}\boldsymbol{\sigma}^{Syl} + v_{Syl}\boldsymbol{\sigma}^{PCL}, \tag{3}$$

where $\boldsymbol{\sigma}^{Syl}$ and $\boldsymbol{\sigma}^{PCL}$ are the stresses in the Sylgard matrix and the PCL network, v_{Syl} and v_{PCL} are volume fractions of the Sylgard matrix and the PCL fibers, which are determined by fabrication and $v_{Syl} + v_{PCL} = 1$.

In reality, the stress distribution depends on the microstructure and the geometry of how two phases spatially arranged. Directly adding up the stresses in the two phases with respective volume fraction is not the case. Dunn (1998) proposed the concept of stress concentration factors, which can be used to redistribute stresses/strains in the composite by considering the real microstructure (Dunn, 1998). Here by introducing stress concentration factors, the total Cauchy stress $\boldsymbol{\sigma}^{total}$ may be rewritten as:

$$\boldsymbol{\sigma}^{total} = \gamma_{Syl}v_{Syl}\boldsymbol{\sigma}^{Syl} + \gamma_{PCL}v_{PCL}\boldsymbol{\sigma}^{PCL}, \tag{4}$$

where γ_{Syl} and γ_{PCL} are stress concentration factors of the Sylgard matrix and the PCL fibers. Based on Dunn (1998), $\gamma_{Syl}v_{Syl} + \gamma_{PCL}v_{PCL} = 1$. For the sake of convenience, $\gamma_{Syl}v_{Syl}$ and $\gamma_{PCL}v_{PCL}$ are denoted by $\bar{v}_{Syl}$ and $\bar{v}_{PCL}$.

2.3.2 Crystallization and melting

Since the crystal-melt transition imparts the SM effect into the SMEC, it is essential for the model to capture the kinetics of crystallization and melting of PCL. The classic theory to describe crystallization kinetics is the Avrami's phase transition theory (Avrami, 1941, 1939, 1940). The original derivations by Avrami was simplified by Evans with the "raindrop" theory (Evans, 1945), in which one considers the wave (fronts of crystals) created by a drop falling down

at time τ propagates from τ to t. The probability that i-th waves pass over point P is given by Poisson's equation (Ozawa, 1971):

$$p_i = \frac{e^{-E} E^i}{i!}, \tag{5}$$

where E is the expectancy and is equal to the average number of such wave fronts. In the crystallization process, a point in melt state is the point that is not passed over by any growing front. Therefore, the valid probability is that of $i = 0$ (Ozawa, 1971):

$$p_0 = e^{-E}, \tag{6}$$

In the case of crystallization, the expectancy E is equal to the volume fraction of crystals without impingement V(t) (Sperling, 2006). Therefore, the relative volume fraction of amorphous phase is (Sperling, 2006):

$$1 - \chi(t) = e^{-V(t)}, \tag{7}$$

where $\chi(t)$ is the relative degree of crystallinity. For $V(t)$, one first considers the case where the nuclei all develop immediately upon cooling the polymer to the temperature of crystallization then expands it to the case of sporadic nucleation (Sperling, 2006).

In the first case, the nucleation density is a constant. The volume growth rate is:

$$\frac{dV(t)}{dt} = AN\frac{(Gt)^n}{t}, \tag{8}$$

where N is the nucleation density, G is the growth rate of crystals (for the isothermal crystallization, G is a constant at a certain temperature), A and n are constants related to the dimension of the crystal. For one-dimension rods, $A = \pi d^2 / 4$, $n = 1$, d is the thickness of crystal domain; for two-dimension discs, $A = 2\pi d$, $n = 2$; for three-dimension spheres, $A = 4\pi$, $n = 3$. Integrating Eq. (8) over t from 0 to t_c (the time point during crystallization):

$$V(t_c) = BN(Gt_c)^n, \tag{9}$$

and $B = A/n$.

For the sporadic nucleation case, the nucleation density is a function of time $N(t)$. From τ to $\tau + d\tau$, the number of newly formed nucleus per volume is $\frac{dN(\tau)}{d\tau}d\tau$ and the volume fraction of these crystalline phases at t (t>τ) is $B\frac{dN(\tau)}{d\tau}\left[G\cdot(t-\tau)\right]^n d\tau$. Integrating from 0 to t_c (the time in crystallization), the volume fraction without impingement is:

$$V(t_c) = B\int_0^{t_c} \frac{dN(\tau)}{d\tau}\left[G\cdot(t_c-\tau)\right]^n d\tau . \tag{10}$$

Eq. (10) describes the isothermal crystallization process. In reality, non-isothermal crystallization might be more common. For example, in the case of this paper, the temperature is lowered continuously to a temperature lower than the crystallization temperature. As the nucleation density and the growth rate of crystals are function of temperature during the non-isothermal crystallization, the nucleation density and the growth rate are the function of temperature and time, expressed as N[T(t)] and G[T(t)] respectively. Eq. (9) can be modified as:

$$V(t_c) = B\int_0^{t_c} \frac{dN[T(\tau)]}{d\tau}\left\{\int_\tau^{t_c} G\left[T(s)\right]ds\right\}^n d\tau . \tag{11}$$

For G[T(t)], Hoffman-Lauritzen expression is widely adopted to describe the growth rate (Lauritzen and Hoffman, 1973):

$$G[T(t)] = G_0 \exp\left\{-\frac{U}{R[T(t)-T_\infty]}\right\}\exp[-\frac{K_g}{T(t)\Delta Tf}], \tag{12}$$

where the pre-exponential factor of crystalline growth rate G_0 is almost independent of temperature (Angelloz, et al., 2000, Isayev and Catignani, 1997). The first exponential term of Eq. (12) reflects the chain mobility in the melt, where U is the diffusional activation energy for the transport of crystallizable segments at the liquid-solid interface (Liu, et al., 2010), R is the universal gas constant, T_∞ is the temperature about $T_g - 30K$ (Angelloz, et al., 2000, Isayev and

Catignani, 1997). The second exponential term contains the secondary nucleation effect on the crystal growth front (Angelloz, et al., 2000). In the term, K_g is the nucleation constant (Liu, et al., 2010), $\Delta T = T_m^0 - T(t)$ is the undercooling, where T_m^0 is the equilibrium melting temperature; $f = 2T(t)/\left[T_m^0 + T(t)\right]$ is a correction factor used for the variation of the heat of fusion with temperature (Angelloz, et al., 2000).

The evolution of the number of nuclei can be empirically described by the following equation (Angelloz, et al., 2000, Isayev and Catignani, 1997):

$$N[T(t)] = N_0 \exp\left\{\beta\left[T_m{}^0 - T(t)\right]\right\}, \tag{13}$$

where N_0 is pre-exponential factor of nucleation density and β an empirical parameter.

Based on the understanding of kinetics of crystallization, the melting kinetics can be developed. During the melting processing, the volume of the existing crystals decreases until it becomes zero. Assume melting starts at time $t = t_{ms}$, the volume fraction at time $t = t_{ms} + t_m$ during melting can be described by:

$$V(t_m) = B \cdot \int_0^{t_{ce}} \frac{dN\left[T(\tau)\right]}{d\tau} \left\{\int_\tau^{t_{ce}} G\left[T(u)\right]du - \int_{t_{ms}}^{t_m} C\left[T(u)\right]du\right\}^n \cdot d\tau, \tag{14}$$

where t_{ce} is the moment when crystallization ends; in general, $t_{ce} = t_{ms}$. C(t) is the rate of decrease of crystal size; in this paper, it is treated as a constant in terms of a low heating rate (2 ℃/min) and narrow temperature range of melting (~35 ℃ to ~65 ℃).

By using Eq. (7) with Eqs. (11)-(14), the relative degree of crystallinity $\chi(t)$ can be calculated. However, in reality, polymer crystallinity cannot reach 100%, so the crystallinity of polymers should be expressed as:

$$v(t) = H_\infty \chi(t), \tag{15}$$

where H_∞ is the saturated crystallinity of a polymer when under a certain condition. According to Kweon et al. (Kweon, et al., 2003), for the PCL fiber network, under similar condition of this paper, $H_\infty = 25\%$.

Fig. 11 shows the simulations of kinetics of crystallization and melting of PCL. It is seen the observable crystallization starts at ~30 ℃ and finishes at ~20 ℃. During melting, observable volume change starts at ~35 ℃ and finishes at ~65 ℃.

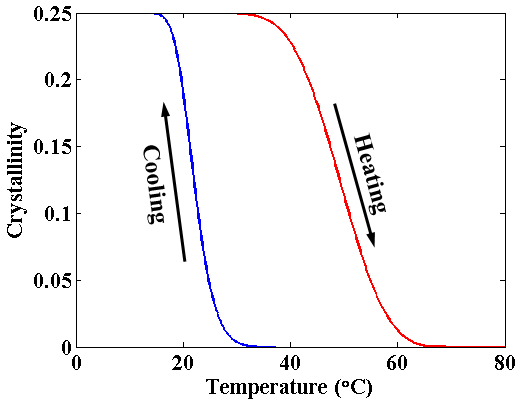

Fig. 11 The simulation of kinetics of crystallization and melting.

2.3.3 Mechanical behavior

As described and shown in Fig. 5, a SM cycle of SMEC involves four distinct thermo-mechanical steps. During cooling and heating steps, mechanical deformation can be coupled with crystallization/melting processes. It therefore becomes a natural choice to describe material behaviors under two thermo-mechanical scenarios: mechanical deformation during crystallization and mechanical deformation during melting. In these two cases, we consider the one-way coupling case where crystallization/melting can affect the concurrent mechanical deformation. The coupling in the reverse direction where mechanical deformation affects crystallization/melting kinetics is not considered. This assumption is valid for two reasons: First, during crystallization, the material deformation rate is much larger than the relaxation time of

polymer melts so that any nonequilibrium deformation can be relaxed and thus mechanical deformation will not influence crystallization. Second, during melting, mechanical deformation in the semicrystalline PCL is relatively small so that the melting kinetics will not be influenced.

For convenience we take both the matrix and fiber network to be hyperelastic solids. In our case the matrix, Sylgard, is in its rubbery state during a shape memory cycle, while the PCL crystals, although linear elastic, can be idealized as hyperelastic. As such there exist free energy functions so that the Cauchy stresses can be obtained as:

$$\begin{aligned} \boldsymbol{\sigma}^{Syl}\left(\mathbf{F}^{Syl}\right) &= J^{-1}\left(\mathbf{F}^{Syl}\right)\frac{\partial W^{Syl}(\mathbf{F}^{Syl})}{\partial \mathbf{F}^{Syl}}\left(\mathbf{F}^{Syl}\right)^{T} \\ \boldsymbol{\sigma}^{C-PCL}\left(\mathbf{F}^{C-PCL}\right) &= J^{-1}\left(\mathbf{F}^{C-PCL}\right)\frac{\partial W^{C-PCL}(\mathbf{F}^{C-PCL})}{\partial \mathbf{F}^{C-PCL}}\left(\mathbf{F}^{C-PCL}\right) \end{aligned}, \tag{16}$$

where the superscripts Syl and C-PCL indicate the quantities associated with Sylgard and PCL crystals, respectively; W is the free energy density function; $\boldsymbol{\sigma}$ is the Cauchy stress tensor; F is the mechanical deformation gradient. It is noted that $\boldsymbol{\sigma}^{Syl}$ is stress contribution from Sylgard matrix, $\boldsymbol{\sigma}^{C-PCL}$ is the Cauchy stress in the PCL semicrystalline phases

As shown in Fig. 11, crystallization and melting are continuous processes and functions of temperature and time. Our basic assumption here is that when a small fraction of polymer crystals is formed, it is in a stress-free state. In order to satisfy the boundary conditions, either overall or locally, however, this small fraction will deform immediately. This stress-free state for new born crystals phases was referred as natural configuration by Rajagapol (Rajagopal and Srinivasa, 1998a, b), and was used by many researchers to study crystallizing polymers (Ma and Negahban, 1995a, Ma and Negahban, 1995b, Negahban, 1993, Negahban and Wineman, 1992), rubbers with thermally induced scissoring and reformation (Tobolsky, 1960, Wineman, 1999, 2005, Wineman and Min, 2000, 2003, Wineman and Shaw, 2008), shape memory polymers (Barot and Rao, 2006, Barot, et al., 2008, Qi, et al., 2008b), and light induced activated polymers (Long, et al., 2009). In this session, we deal with mechanics during crystallization. In addition, we

will provide an efficient calculation scheme later. During a SM cycle, crystallization can occur during cooling (S2) and unloading at low temperature (S3). As indicated below, the method in this section is also applied to the case where there is no crystallization, such as the high temperature loading step (S1).

To better illustrate the physics and the mechanics, we use an incremental approach. Considering at time $t = t_0$, all PCL crystals are melted, and mechanical deformation gradient is F_0. Since only Sylgard carries load at this moment, $\mathbf{F}^{Syl} = \mathbf{F}_0$, and

$$\boldsymbol{\sigma}_0^{total} = \bar{v}_{Syl}\boldsymbol{\sigma}^{Syl}\left(\mathbf{F}_0\right). \tag{17}$$

After time $t = t_0$, crystallization starts. At $t = t_0 + \Delta t$, a small amount of crystal phase forms from PCL melts with a volume fraction of Δv_1^c. As stated above, we assume that this newly formed crystal phase is initially undeformed and stress-free. Simultaneously, a mechanical deformation may occur. One reason for this mechanical deformation could be due to mechanical loading change during crystallization. For example, in a SM cycle, crystallization process can easily extend into S3, which is the unloading step at the temperature below the crystallization temperature. Another reason could be attributed to modulus change of Sylgard due to its dependence on temperature (entropic elasticity). The deformation and load transfer from matrix to polymer crystals can be very complicated (Ma and Negahban, 1995a, Ma and Negahban, 1995b, Negahban, 1993, Negahban and Wineman, 1992); for example, they may depend on the shape, spatial distribution of the crystals. Here, we simplify this deformation transfer by assuming both Sylgard and PCL crystals will undergo a small incremental deformation gradient $\Delta\mathbf{F}_1$. Then, the deformations in the Sylgard and the PCL crystal become

$$\mathbf{F}^{Syl} = \Delta\mathbf{F}_1\mathbf{F}_0,\ \mathbf{F}_{1\to 1} = \Delta\mathbf{F}_1, \tag{18}$$

and the total stress is

$$\boldsymbol{\sigma}_1^{total} = \bar{v}_{Syl}\boldsymbol{\sigma}^{Syl}\left(\Delta\mathbf{F}_1\mathbf{F}_0\right) + \bar{v}_{PCL}\Delta v_1^c\boldsymbol{\sigma}^{C-PCL}\left(\mathbf{F}_{1\to 1}\right). \tag{19}$$

Here, the subscript in $\mathbf{F}_{1\to1}$ represents the deformation gradient at the time of the 1st time increment for the crystal phases formed during the 1st time increment. In order to better demonstrate incremental process before and during crystallization, schematics are shown in Fig. 12.

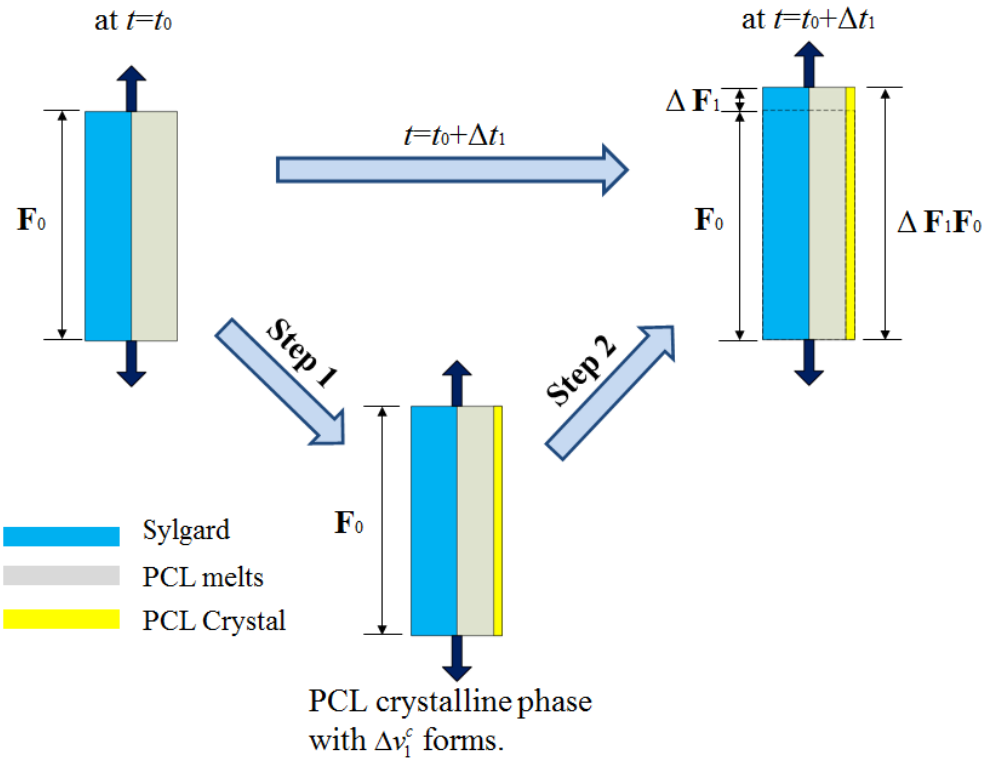

Fig. 12 Schematics of mechanics during crystallization: At $t=t_0$, all PCL is melted and only Sylgard carries load. During crystallization starts at $t=t_0+\Delta t$, a PCL crystalline phase with Δv_1^c is formed in a undeformed and stress-free state (Step 1); then, a mechanical incremental deformation gradient $\Delta\mathbf{F}_1$ is applied to both Sylgard and PCL crystal, as the changing external load or the entropic elasticity of Sylgard (Step 2).

As the crystallization proceeds, more small volume fractions of PCL crystals form. Each of them has no deformation in its new-born state but deforms after its birth due to the reasons discussed above. Following the above discussion, at time $t=t_0+m\Delta t$, deformation gradient in the crystalline phase formed at time $t=t_0+i\Delta t$ can be expressed as:

$$\mathbf{F}_{i\to m}=\Delta\mathbf{F}_m\mathbf{F}_{i\to m-1}=\prod_{j=i}^{m}{}^{L}\,\Delta\mathbf{F}_j\,, \tag{20}$$

where $\prod_{i=1}^{n}{}^{L}(\ )_i$ means the multiplicative operation goes toward left, or $\prod_{i=1}^{n}{}^{L}(\ )_i = (\ )_n \cdots (\ )_2 (\ )_1$; $\Delta\mathbf{F}_j$ is the incremental deformation gradient at $t = t_0 + j\Delta t$ when the j-th crystal forms; $\mathbf{F}_{i\to m}$ represents the deformation gradient at time $t = t_0 + m\Delta t$ for the PCL crystals formed at time $t = t_0 + i\Delta t$. Note that $\Delta\mathbf{F}_i$ has its reference configuration occupying the spatial configuration at time $t = t_0 + (i-1)\Delta t$, so does $\mathbf{F}_{i\to m}$. The deformation gradient in the Sylgard matrix is

$$\mathbf{F}^{Syl} = \left(\prod_{j=1}^{m}{}^{L} \Delta\mathbf{F}_j \right) \mathbf{F}_0 = \mathbf{F}_{1\to m}\mathbf{F}_0 . \tag{21}$$

The total stress is

$$\boldsymbol{\sigma}_m^{total} = \bar{v}_{Syl}\boldsymbol{\sigma}^{Syl}\left(\mathbf{F}_{1\to m}\mathbf{F}_0\right) + \bar{v}_{PCL}\sum_{i=1}^{m}\Delta v_i^c \boldsymbol{\sigma}^{C-PCL}\left(\mathbf{F}_{i\to m}\right). \tag{22}$$

Note that Eq. (22) can also be applied to the case where there is no new crystalline phase formed by simply setting $\Delta v_i^c = 0$.

During melting, the crystalline phases vanish gradually. According to the kinetics description of melting process, the portion of crystal domains that grows at a later time melts first (as they are closer to the crystal-melt boundary). Assuming at the time when melting starts ($t = t_{ms}$), the total number of crystal phases (which is equal to the total number of time increments during crystallization) is m_e. At time $t = t_{ms} + \Delta t$, $\Delta v_{m_e}^c$ melts. Here, for the sake of brevity, we assume that within Δt, $\Delta v_{m_e}^c$ volume fraction of crystals melts. Concurrently to melting, a small incremental deformation gradient $\Delta\mathbf{F}_1^{melt}$ is induced. This deformation, for example, could be due to shape recovery in the heating step of a SM cycle. Following the same assumption for mechanical deformation during crystallization, we assume that the incremental deformation

gradient $\Delta\mathbf{F}_1^{melt}$ is applied to all the phases, except of m_e-th crystalline phase, which just melted and cannot carry load. Therefore, the total stress is

$$\boldsymbol{\sigma}^{total} = \bar{v}_{Syl}\boldsymbol{\sigma}^{Syl}\left(\Delta\mathbf{F}_1^{melt}\mathbf{F}_{1\to m}\mathbf{F}_0\right) + \bar{v}_{PCL}\sum_{i=1}^{m_e-1}\Delta v_i^c\boldsymbol{\sigma}^{C-PCL}\left(\Delta\mathbf{F}_1^{melt}\mathbf{F}_{i\to m}\right), \tag{23}$$

Following the same argument, at time $t = t_{ms} + n\Delta t$, the crystal with volume fraction $\Delta v^c_{m_e-n+1}$ melts and the deformation gradient is increased by $\Delta\mathbf{F}_n^{melt}$. The total stress is:

$$\begin{aligned}\boldsymbol{\sigma}^{total} &= \bar{v}_{Syl}\boldsymbol{\sigma}^{Syl}\left(\mathbf{F}_{1\to n}^{melt}\mathbf{F}_{1\to m}\mathbf{F}_0\right) + \bar{v}_{PCL}\sum_{i=1}^{m_e-n}\Delta v_i^c\boldsymbol{\sigma}^{C-PCL}\left(\mathbf{F}_{1\to n}^{melt}\mathbf{F}_{i\to m}\right),\\ \mathbf{F}_{1\to n}^{melt} &= \prod_{i=1}^{n}{}^{L}\,\Delta\mathbf{F}_i^{melt}.\end{aligned} \tag{24}$$

Depending on boundary conditions, Eq. (24) can be solved for $\Delta\mathbf{F}_n^{melt}$ if a constant stress is applied, (load control) or for $\boldsymbol{\sigma}^{total}$ if is $\Delta\mathbf{F}_n^{melt}$ given (displacement control).

2.3.4 Effective phase model (EPM)

The mechanics discussed above is computationally expensive as it requires the deformation gradient in each fraction of crystals to be updated in each time increment and is stored as internal variables. This can quickly exhaust computer CPU time and memory resources. In order to enhance computational efficiency, Long et al (2010) developed an effective phase model (EPM) to capture the mechanics of material with evolving phases (Long, et al., 2010). In the EPM, behaviors of the new phases formed at different time are combined into an effective phase with an effective deformation. The effective phase and its effective deformation are continuously updated to account for the response of each new phase that would normally develop under the general loading conditions (Long, et al., 2010). In this paper, the EPM theory is used to improve the efficiency.

During crystallization at time $t = t_0 + m\Delta t$, there are m PCL crystalline phases during crystallization beginning at $t = t_0$. In the EPM, it is assumed that the mechanical deformation in these m crystal phases can be represented by an effective phase with a combined volume fraction of $v_m^c = \sum_{i=1}^{m} \Delta v_i^c$ and an effective deformation gradient $\bar{\mathbf{F}}_m$. The total stress in SMEC is therefore:

$$\boldsymbol{\sigma}_m^{total} = \bar{v}_{Syl}\boldsymbol{\sigma}^{Syl}(\mathbf{F}_m) + \bar{v}_{PCL}v_m^c\boldsymbol{\sigma}^{C-PCL}(\bar{\mathbf{F}}_m), \tag{25}$$

At time $t = t_0 + (m+1)\Delta t$, a new crystalline phase with volume fraction Δv_{m+1}^c is formed. Accompanying this new crystalline phase, the SMEC undergoes a further deformation with $\Delta\mathbf{F}_{m+1}$ and the total stress is now calculated as:

$$\boldsymbol{\sigma}_{m+1}^{total} = \bar{v}_{Syl}\boldsymbol{\sigma}^{Syl}(\Delta\mathbf{F}_{m+1}\mathbf{F}_m) + \bar{v}_{PCL}\left[v_m^c\boldsymbol{\sigma}^{C-PCL}(\Delta\mathbf{F}_{m+1}\bar{\mathbf{F}}_m) + \Delta v_{m+1}^c\boldsymbol{\sigma}^{C-PCL}(\Delta\mathbf{F}_{m+1})\right]. \tag{26}$$

Applying Eq. (25) to the time $t = t_0 + (m+1)\Delta t$, we have

$$\boldsymbol{\sigma}_{m+1}^{total} = \bar{v}_{Syl}\boldsymbol{\sigma}^{Syl}(\mathbf{F}_{m+1}) + \bar{v}_{PCL}v_{m+1}^c\boldsymbol{\sigma}^{C-PCL}(\bar{\mathbf{F}}_{m+1}), \tag{27}$$

where $\mathbf{F}_{m+1} = \Delta\mathbf{F}_{m+1}\mathbf{F}_m$ and $\bar{\mathbf{F}}_{m+1} = \Delta\bar{\mathbf{F}}_{m+1}\bar{\mathbf{F}}_m$. Comparing Eqs. (26) and (27), we have

$$v_{m+1}^c\boldsymbol{\sigma}^{C-PCL}(\Delta\bar{\mathbf{F}}_{m+1}\bar{\mathbf{F}}_m) = v_m^c\boldsymbol{\sigma}^{C-PCL}(\Delta\mathbf{F}_{m+1}\bar{\mathbf{F}}_m) + \Delta v_{m+1}^c\boldsymbol{\sigma}^{C-PCL}(\Delta\mathbf{F}_{m+1}), \tag{28}$$

For a given $\Delta\mathbf{F}_{m+1}$ and with a calculation of Jacobian, Eq. (28) can be solved using Newton-Raphson scheme for the deformation increment in the effective phase $\Delta\bar{\mathbf{F}}_{m+1}$. The same process can be applied to melting and is not discussed here. In order to help readers better understand the EPM theory, schematics are presented in Fig. 13.

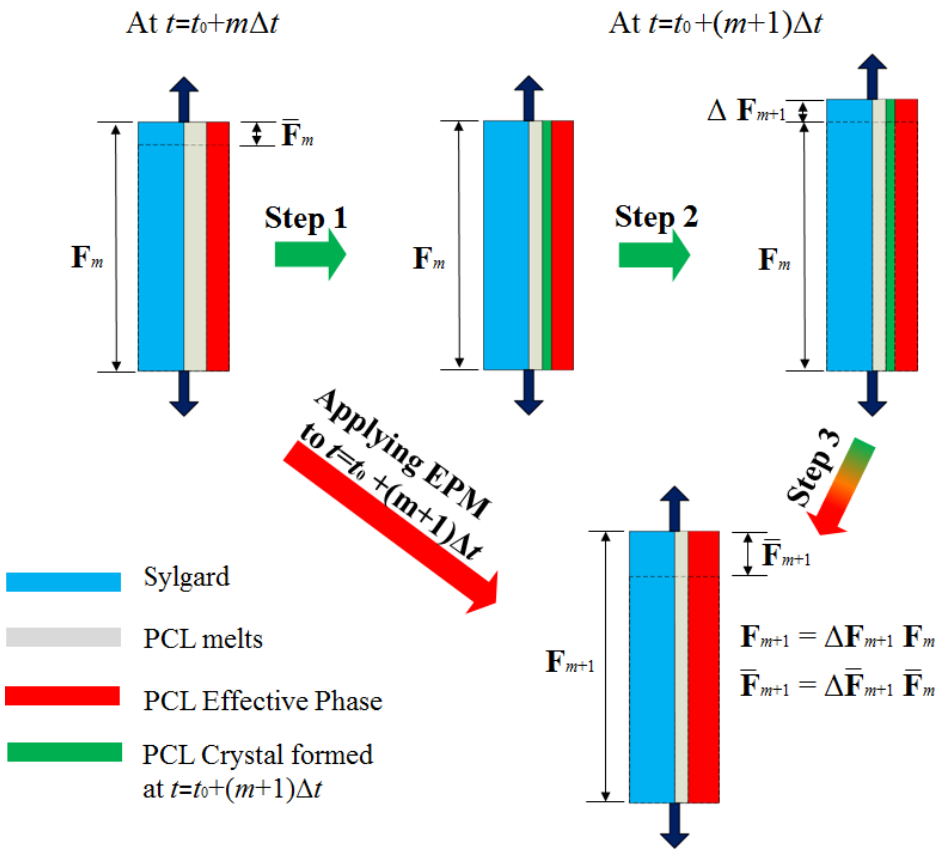

Fig. 13 Schematics of EPM: at $t=t_0+m\Delta t$, there is an effective phase with volume fraction v_m^c and effective deformation $\bar{\mathbf{F}}_m$. At $t=t_0+(m+1)\Delta t$, a PCL crystalline phase with Δv_{m+1}^c is formed in a undeformed and stress-free state (Step 1); then, a mechanical incremental deformation gradient $\Delta\mathbf{F}_{m+1}$ is applied to Sylgard, PCL effective phase and the newly formed PCL crystalline phase (Step 2); at Step 3, the newly formed PCL crystalline phase is merged into the existing PCL effective phase. If directly applying the EPM theory to $t=t_0+(m+1)\Delta t$, there is an effective phase with volume fraction v_{m+1}^c and effective deformation $\bar{\mathbf{F}}_{m+1}$.

2.3.5 Thermal contraction/expansion

Thermal contraction/expansion in SMEC consists of thermal contractions/expansions of Sylgard and PCL network, where the latter can be further attributed to melts, crystals, and volume changes due to crystal-melt phase transition. Here, we assume thermal contraction/expansion is always isotropic, therefore:

$$\mathbf{G}^T=J^T\mathbf{I}=\left(\lambda^T\right)^3\mathbf{I}, \tag{29}$$

where λ^T is the linear stretch ratio due to thermal contraction/expansion.

Base on the thermal contraction/expansion experiment in 2.4, there are three region of the thermal strain: (i) the high temperature linear CTE (α_1) region where PCL is completely melted; (ii) the nonlinear strain drop or rise ($\Delta\lambda_{PT}$) region corresponding to the crystal-melt transition of PCL; (iii) the low temperature linear CTE (α_2) region where PCL is crystallized.

At high temperatures, where PCL melts completely and SMEC contracts or expands linearly with α_1, thermal stretch is:

$$\lambda^T = 1 + \alpha_1 \left(T - T_H \right), \tag{30}$$

where T_H is the temperature where the experiment starts.

During the crystal-melt phase transition, where v^c increasing from 0 towards the saturated crystallinity H_∞ and the thermal deformation can be expressed by combining the linear and nonlinear thermal behavior:

$$\lambda^T = 1 + \alpha_1 \left(T_m^0 - T_H \right) + \lambda_{PT}\, v^c \left(T \right) / H_\infty , \tag{31}$$

where T_m^0 is the equilibrium melting temperature in Eq. (12) where crystallization or melting starts and H_∞ is the saturated crystallinity in Eq. (15).

At low temperature, where PCL crystallizes completely and $v^c = H_\infty$, SMEC contracts or expands linearly with α_2, thermal stretch is:

$$\lambda^T = 1 + \alpha_1 \left(T_m^0 - T_H \right) + \alpha_2 \left(T - T_r \right) + \Delta\lambda_{PT} \tag{32}$$

where T_r is a reference temperature corresponding to the time increment where the crystallinity reaches H_∞.

Fig. 14 shows the comparison between experimental data and simulation. Overall, the model captures the thermal contraction/expansion behavior. The largest error occurs during heating from 10 ℃ to 50 ℃: The model predicts a linear expansion whilst the experiment shows a slightly nonlinear behavior.

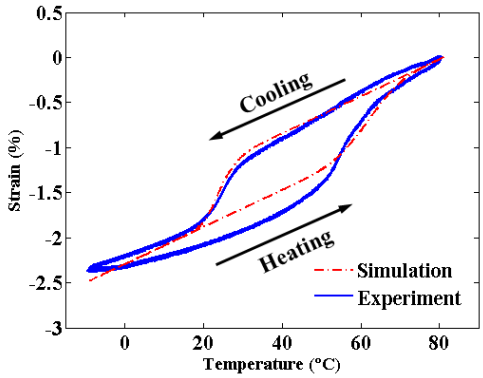

Fig. 14 Comparison of experiment and simulation of thermal contraction and expansion.

2.4 Results

2.4.1 Mechanical behaviors under uniaxial loading

Before reporting results, we briefly describe the above model with simple material behaviors and under uniaxial loading conditions.

For Sylgard tested, the maximum stretch of the sample was with 1.15 and the stress-strain behavior did not exhibit the non-Gaussian type of behaviors. For PCL semicrystalline polymer, as will be shown later, the strain is low. For the sake of brevity, we assume that both Sylgard and PCL semicrystalline polymers follow the incompressible neo-Hookean behavior with the strain energy function as (Treloar, 1958):

$$W^{Syl} = \frac{1}{2} NkT(\lambda_1^2 + \lambda_2^2 + \lambda_3^2 - 3),\ W^{C-PCL} = \frac{1}{2}\mu(\lambda_1^2 + \lambda_2^2 + \lambda_3^2 - 3)\,, \tag{33}$$

where λ_i are the applied stretches in the three principal directions, N is the chain density, k is Boltzmann's constant, T is temperature, μ is the shear modulus of semicrystalline PCL. Under the uniaxial loading condition and considering the material incompressibility, the Cauchy stress of each phase is:

$$\begin{aligned}\sigma^{Syl} &= \lambda\frac{\partial W_{Syl}(\lambda)}{\partial\lambda} = NkT\left(\lambda^2 - 1/\lambda\right)\\ \sigma^{C-PCL} &= \lambda\frac{\partial W_{PCL}(\lambda)}{\partial\lambda} = \mu\left(\lambda^2 - 1/\lambda\right)\end{aligned}, \tag{34}$$

where λ is the mechanical stretch in the uniaxial stretching direction and it is defined as λ=1+ε, ε is the strain. Note that for Sylgard, the stress is also a function of temperature T. In addition, the total stretch of the material should include the thermal contraction/expansion, i.e, $\lambda^{total} = \lambda^T\lambda$. The mechanical stretch during the SM cycle can be solved by general model and the EPM theory is used to improve the computational efficiency.

Before crystallization, only Sylgard carries load. Therefore,

$$\sigma_0^{total} = \bar{v}_{Syl}\sigma^{Syl}(\lambda_0, T_0). \tag{35}$$

During crystallization, at time $t = t_0 + m\Delta t$, a small amount of crystal phase forms from melting phase with volume fraction Δv_m^c and induces a small stretch increment $\Delta\lambda_m$. Deformation in the crystalline phase formed at any $t = t_0 + i\Delta t$ is:

$$\lambda_{i\to m} = \lambda_{i\to m-1}\Delta\lambda_m = \prod_{j=i}^{m}\Delta\lambda_j. \tag{36}$$

The total stress is given by:

$$\sigma_m^{total} = \bar{v}_{Syl}\sigma^{Syl}\left(\Delta\lambda_m\lambda_{m-1}, T_m\right) + \bar{v}_{PCL}\sum_{i=1}^{m}\Delta v_i^c\sigma^{C-PCL}\left(\Delta\lambda_m\lambda_{i\to m-1}\right), \tag{37}$$

where $\lambda_{m-1} = \lambda_{1\to m-1}\lambda_0$ and T_m is the temperature at $t = t_0 + m\Delta t$. The above equation can be solved according to the boundary conditions applied. For the case of stretch controlled deformation, the stress can be calculated; for the case where the sample is subject to a constant external force, or a constant nominal stress $\bar{s}_0$, and the Cauchy stress σ_m^{total} becomes $\Delta\lambda_m\lambda_{m-1}\bar{s}_0$, $\Delta\lambda_m$ can be solved by following methods.

As long as the time increment is restricted to be sufficiently small, $\Delta\lambda_m$ can be rewritten as:

$$\Delta\lambda_m = 1 + \Delta\varepsilon, \tag{38}$$

where $\Delta\varepsilon \ll 1$. The Cauchy stress for Sylgard and PCL crystalline phases may be Taylor expanded to first-order in $\Delta\varepsilon$:

$$\begin{aligned}
&\sigma^{Syl}\left(\Delta\lambda_m\lambda_{m-1}\right) = \sigma^{Syl}\left[\left(1+\Delta\varepsilon\right)\lambda_{m-1}\right] \approx \sigma^{Syl}\left(\lambda_{m-1}\right) + \sigma^{Syl\prime}\left(\lambda_{m-1}\right)\lambda_{m-1}\Delta\varepsilon,\\
&\sigma^{C-PCL}\left(\Delta\lambda_m\lambda_{i\to m-1}\right) \approx \sigma^{C-PCL}\left(\lambda_{i\to m-1}\right) + \sigma^{C-PCL\prime}\left(\lambda_{i\to m-1}\right)\lambda_{i\to m-1}\Delta\varepsilon,\\
&\sigma^{C-PCL}\left(\Delta\lambda_m\right) \approx \sigma^{C-PCL\prime}\left(1\right)\Delta\varepsilon,
\end{aligned} \tag{39}$$

where $\sigma'(\lambda) = \dfrac{\partial\sigma(\lambda)}{\partial\lambda}$. Inserting Eq. (39) into Eq. (37), the total Cauchy stress would be rewritten as:

$$\begin{aligned}
\left(1+\Delta\varepsilon\right)\lambda_{m-1}\bar{s}_0 &= \bar{v}_{Syl}\sigma^{Syl}\left(\lambda_{m-1},T_m\right) + \bar{v}_{PCL}\sum_{i=1}^{m-1}\Delta v_i^c\sigma^{C-PCL}\left(\lambda_{i\to m-1}\right)\\
&+\left\{\bar{v}_{Syl}\sigma^{Syl\prime}\left(\lambda_{m-1},T_m\right)\lambda_{m-1} + \bar{v}_{PCL}\left[\sum_{i=1}^{m-1}\Delta v_i^c\sigma^{C-PCL\prime}\left(\lambda_{i\to m-1}\right) + \Delta v_m^c\sigma^{C-PCL\prime}\left(1\right)\right]\right\}\Delta\varepsilon
\end{aligned}. \tag{40}$$

Therefore, $\Delta\lambda_m$ is:

$$\Delta\lambda_m = 1 + \frac{\lambda_{m-1}\bar{s}_0 - \bar{v}_{Syl}\sigma^{Syl}\left(\lambda_{m-1},T_m\right) - \bar{v}_{PCL}\sum_{i=1}^{m-1}\Delta v_i^c\sigma^{C-PCL}\left(\lambda_{i\to m-1}\right)}{\bar{v}_{Syl}\sigma^{Syl\prime}\left(\lambda_{m-1},T_m\right)\lambda_{m-1} + \bar{v}_{PCL}\left[\sum_{i=1}^{m-1}\Delta v_i^c\sigma^{C-PCL\prime}\left(\lambda_{i\to m-1}\right) + \Delta v_m^c\sigma^{C-PCL\prime}\left(1\right)\right] - \lambda_{m-1}\bar{s}_0} \tag{41}$$

In order to better understand the process of numerical implementation, a flowchart about calculation of stretch under stress control at time $t = t_0 + m\Delta t$ during crystallization for the general mechanics theory is presented in Fig. 15.

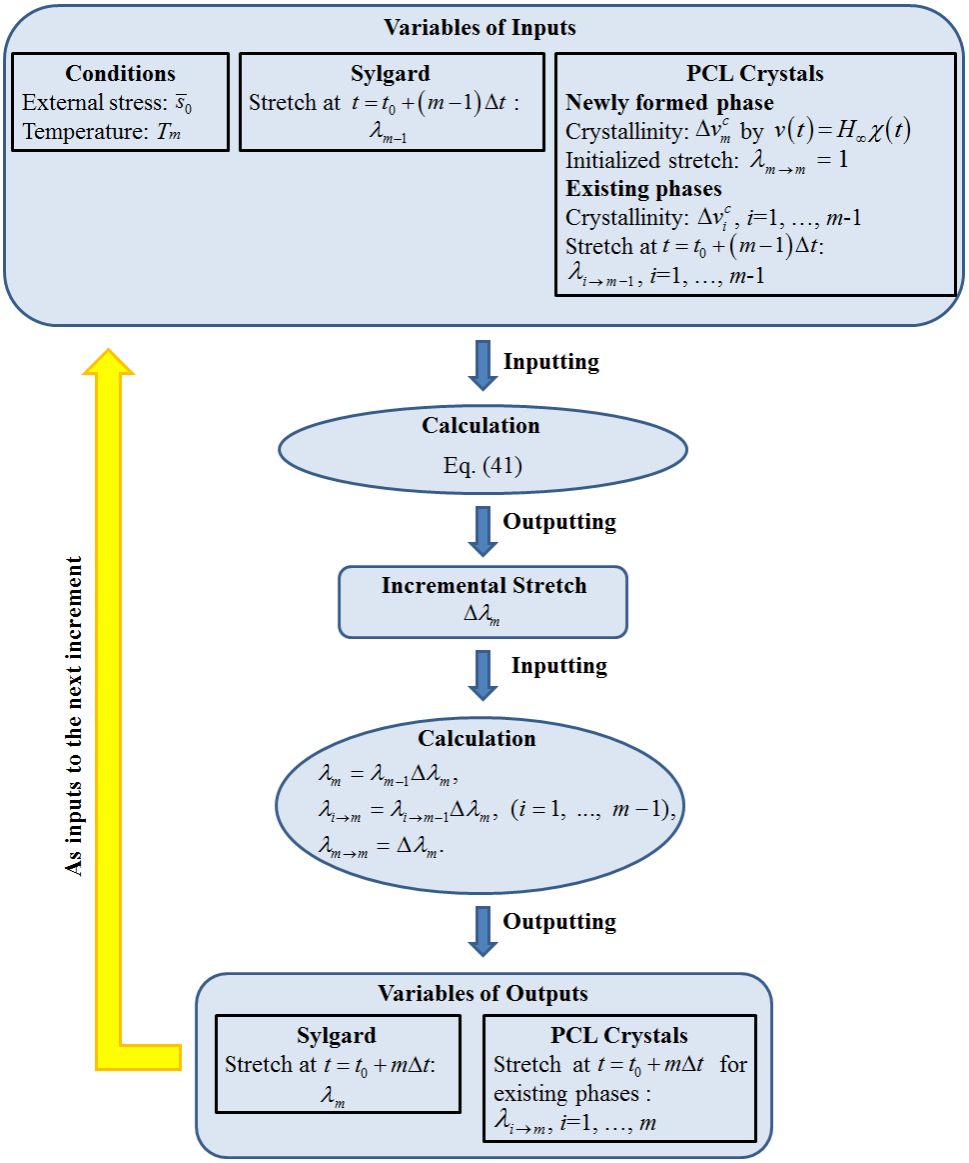

Fig. 15 The flowchart shows the procedure to calculate stretch under stress control at time $t = t_0 + m\Delta t$ during crystallization by using the general theory.

During melting, at time $t = t_{ms} + n\Delta t$, after several crystalline phases melt, the existing crystal phases with volume fraction $\sum_{i=1}^{m_c - n} \Delta v_i^c$ and the Sylgard matrix should deform $\Delta\lambda_n^{melt}$ to satisfy the boundary conditions. Deformation of the crystalline phases formed at time $t = t_0 + i\Delta t$ is:

$$\lambda_{i\to n}=\Delta\lambda_n^{melt}\lambda_{i\to n-1},\ \lambda_{i\to n-1}=\lambda_{i\to ms}\lambda_{1\to n-1}^{melt},\ \lambda_{1\to n-1}^{melt}=\prod_{j=1}^{n-1}\Delta\lambda_j^{melt}\ , \tag{42}$$

and the total stress is

$$\sigma_n^{total}=\bar{v}_{Syl}\sigma^{Syl}\left(\Delta\lambda_n^{melt}\lambda_{1\to n-1}^{melt}\lambda_{ms},T_n\right)+\bar{v}_{PCL}\sum_{i=1}^{m_e-n}\Delta v_i^c\sigma^{C-PCL}(\Delta\lambda_n^{melt}\lambda_{i\to n})\,. \tag{43}$$

Similarly with Eq. (37), $\Delta\lambda_n^{melt}$ can be solved:

$$\Delta\lambda_n^{melt}=1+\frac{\lambda_{1\to n-1}^{melt}\lambda_{ms}\bar{s}_0-\bar{v}_{Syl}\sigma^{Syl}\left(\lambda_{1\to n-1}^{melt}\lambda_{ms}\bar{s}_0,T_n\right)-\bar{v}_{PCL}\sum_{i=1}^{m_e-n}\Delta v_i^c\sigma^{C-PCL}\left(\lambda_{i\to n-1}\right)}{\bar{v}_{Syl}\sigma^{Syl\prime}\left(\lambda_{1\to n-1}^{melt}\lambda_{ms},T_n\right)\lambda_{m-1}+\bar{v}_{PCL}\sum_{i=1}^{m_e-n}\Delta v_i^c\sigma^{C-PCL\prime}\left(\lambda_{i\to n-1}\right)-\lambda_{1\to n-1}^{melt}\lambda_{ms}\bar{s}_0}\,. \tag{44}$$

Eq. (41) and Eq. (44) provide the solution of stretch increments during crystallization and melting. However the drawback of the general mechanics model is all deformations for the existing PCL crystalline phase should be stored as internal variables, which would quickly exhaust computer CPU time and memory resources. Here, EPM can be applied to improve the efficiency. The total stress during crystallization at time $t=t_0+m\Delta t$ is:

$$\sigma_m^{total}=\bar{v}_{Syl}\sigma^{Syl}\left(\lambda_{m-1}\Delta\lambda_m,T_m\right)+\bar{v}_{PCL}\left[v_{m-1}^c\sigma^{C-PCL}(\bar{\lambda}_{m-1}\Delta\lambda_m)+\Delta v_m^c\sigma^{C-PCL}(\Delta\lambda_m)\right], \tag{45}$$

where $v_{m-1}^c=\sum_{i=1}^{m-1}\Delta v_i^c$ is the volume fraction for the effective phase at $t=t_0+(m-1)\Delta t$, $\bar{\lambda}_{m-1}$ is the effective deformation on the effective phase at $t=t_0+(m-1)\Delta t$. At $t=t_0+m\Delta t$, a new crystalline phase with volume fraction Δv_m^c is formed and the entire material deforms by a small stretch increment $\Delta\lambda_m$ due to the changing of conditions such as unloading or entropic elasticity of Sylgard. $\Delta\lambda_m$ can be solved similarly with Eq. (37):

$$\Delta\lambda_m=1+\frac{\lambda_{m-1}\bar{s}_0-\bar{v}_{Syl}\sigma^{Syl}\left(\lambda_{m-1},T_m\right)-\bar{v}_{PCL}v_{m-1}^c\sigma^{C-PCL}\left(\bar{\lambda}_{m-1}\right)}{\bar{v}_{Syl}\sigma^{Syl\prime}\left(\lambda_{m-1},T_m\right)\lambda_{m-1}+\bar{v}_{PCL}\left[\sigma^{C-PCL\prime}\left(\bar{\lambda}_{m-1}\right)\bar{\lambda}_{m-1}+\Delta v_m^c\sigma^{C-PCL\prime}(1)\right]-\lambda_{m-1}\bar{s}_0}\,. \tag{46}$$

According to EPM, at $t=t_0+m\Delta t$, the newly formed phase can be merged into the existing effective phase. Therefore, total stress at $t=t_0+m\Delta t$ may be rewritten as:

$$\sigma_m^{total} = \overline{v}_{Syl}\sigma^{Syl}\left(\lambda_{m-1}\Delta\lambda_m, T_m\right) + \overline{v}_{PCL}\left[v_m^c\sigma^{C-PCL}(\overline{\lambda}_{m-1}\Delta\overline{\lambda}_m)\right], \tag{47}$$

where $\Delta\overline{\lambda}_m$ is the incremental deformation for the effective phase. Comparing Eqs. (45) and (47), one obtains:

$$v_m^c\sigma^{C-PCL}(\overline{\lambda}_{m-1}\Delta\overline{\lambda}_m) = v_{m-1}^c\sigma^{C-PCL}(\overline{\lambda}_{m-1}\Delta\lambda_m) + \Delta v_m^c\sigma^{C-PCL}(\Delta\lambda_m), \tag{48}$$

and $\Delta\overline{\lambda}_m$ can be calculated:

$$\Delta\overline{\lambda}_m = 1 + \frac{v_{m-1}^c\sigma^{C-PCL}(\overline{\lambda}_{m-1}\Delta\lambda_m) + \Delta v_m^c\sigma^{C-PCL}(\Delta\lambda_m) - v_m^c\sigma^{C-PCL}(\overline{\lambda}_{m-1})}{v_m^c\sigma^{C-PCL'}(\overline{\lambda}_{m-1})\overline{\lambda}_{m-1}}. \tag{49}$$

Similar process can be applied to the melting process. The flowchart in Fig. 16 illustrates the calculation procedure of stretch under stress control at time $t = t_0 + m\Delta t$ during crystallization using the EPM theory.

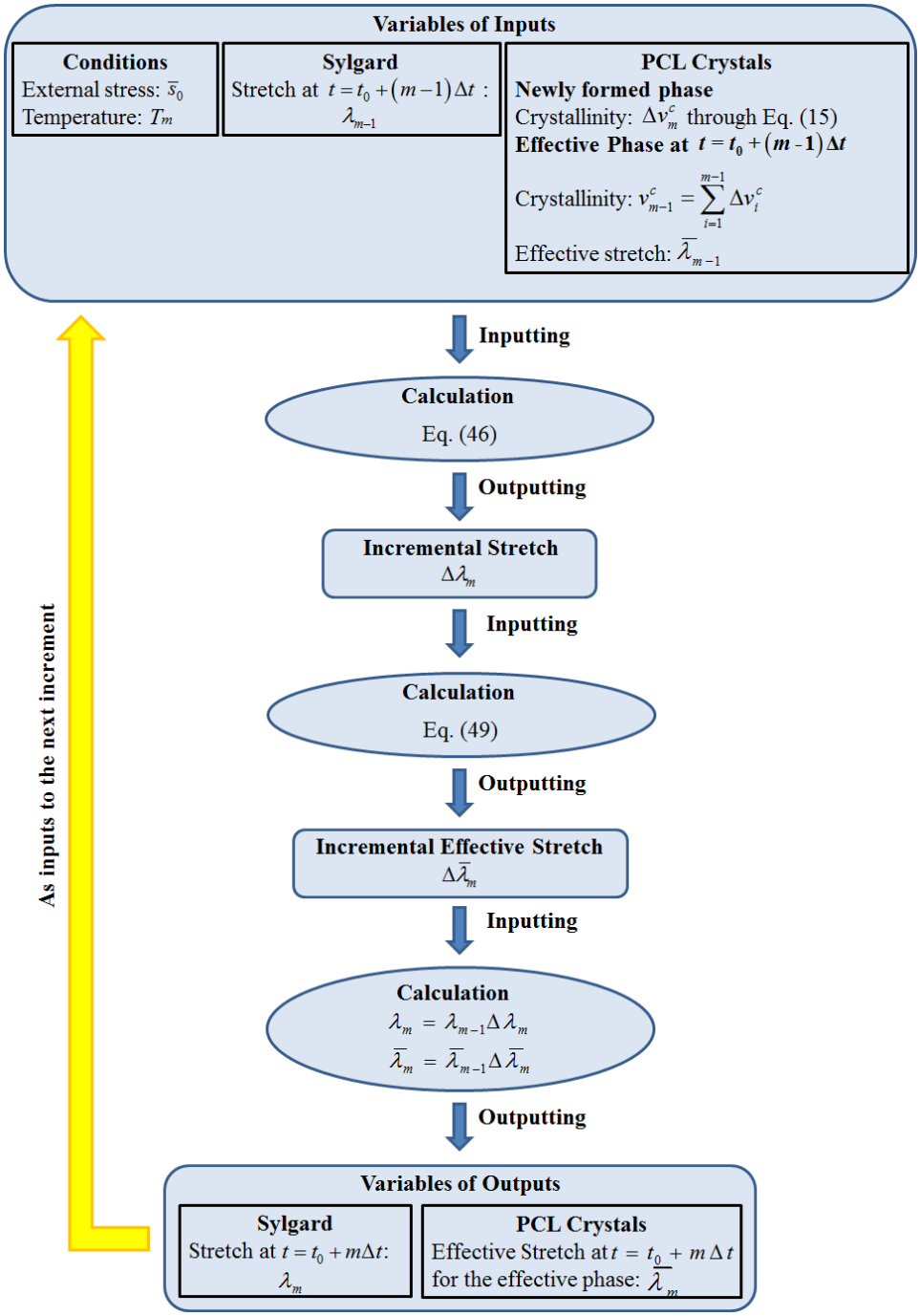

Fig. 16. The flowchart shows the procedure to calculate stretch under stress control at time $t = t_0 + m\Delta t$ during crystallization by using the EPM theory.

2.4.2 Comparison between Experiments and Simulations

The experimental result from the four-step thermo-mechanical cycle with 0.15MPa imposed stress was used to fit the model parameters. Parameters are listed in Table 2. There are

totally 18 parameters, 12 parameters are obtained from fabrication, experiments, handbooks and literatures, and 6 parameters are determined by parameter fitting. These parameters were used for the rest of simulations in this section. Fig. 17 shows the model fitting. The excellent agreement between model simulation and experiment validates the model capability of capturing the physics underlying the shape memory behavior.

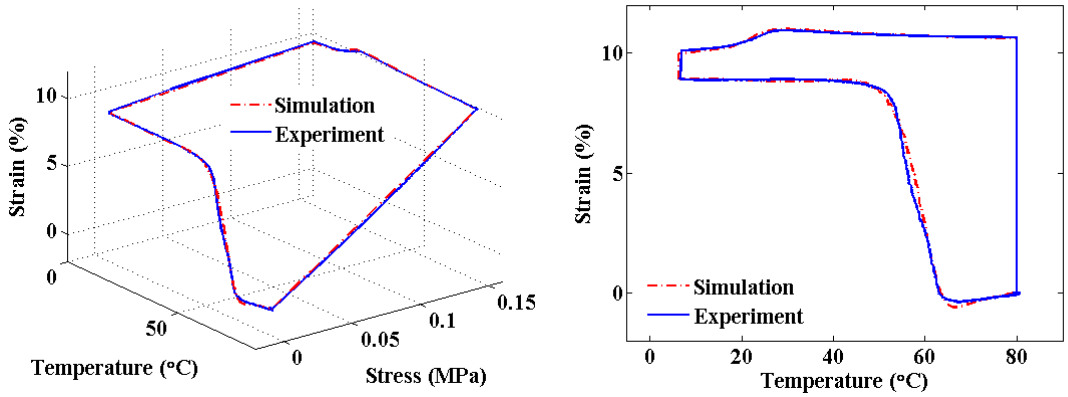

(a) (b)

Fig. 17 Model fitting to the experimental result for the case of imposed stress 0.15MPa. (a) Stress-Temperature-Strain plot. (b) Strain-Temperature plot.

The material parameters identified by fitting the 0.15MPa curve were then used to predict the shape memory behaviors with 0.1MPa and 0.2MPa stresses. Fig. 18 shows the comparison between the model prediction and the experiment. The good agreement between the model prediction and the experiment verifies the model.

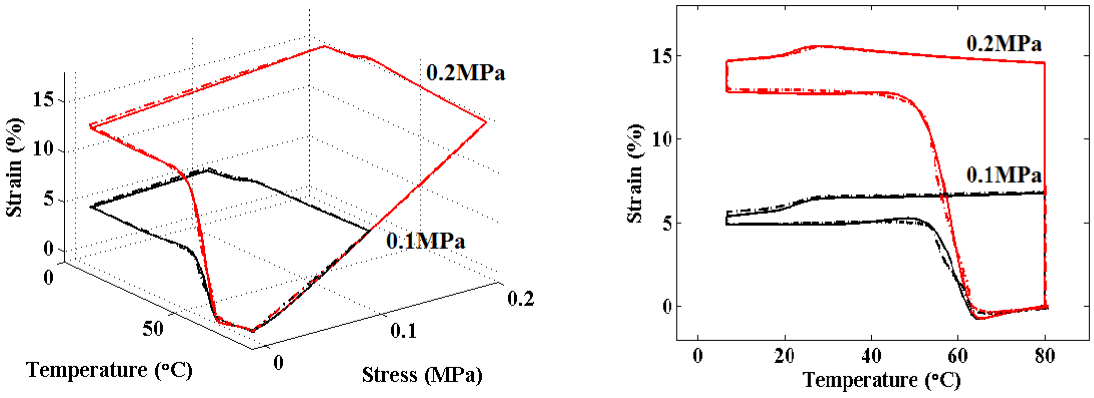

(a) (b)

Fig. 18 Comparisons between model predictions (solid-dot line) and experimental results (solid line) for the cases of 0.1MPa (red) and 0.2MPa (black): (a) Stress-Temperature-Strain plot. (b) Strain-Temperature plot.

Table 2. List of material parameters

Parameter	Value	Description (Fitting parameter are described in italics)
Composition		
v_{Syl}	0.87	Volume fraction of Sylgard (Determined by fabrication)
v_{PCL}	0.13	Volume fraction of PCL (Determined by fabrication)
Kinetics of crystallization and melting		
G_0	4.6×10^5m s^{-1}	Pre-exponential factor of growth rate (From Liu et al (Liu, et al., 2010))
U	17.3kJ mol^{-1}	Diffusional activation energy (From Liu et al (Liu, et al., 2010))
T_m^0	310K	The equilibrium melting temperature (From Kweon et al. (Kweon, et al., 2003))
T_∞	193K	The temperature about 30K lower than T_g (T_g obtained from DMA)
K_g	$35080K^2$	Nucleation constant (From Liu et al (Liu, et al., 2010))
N_0	2.4×10^4 m^{-3}	Pre-exponential factor of nucleation density (Fitting parameter)
β	$0.1349K^{-1}$	Empirical parameter (From Angelloz et al (Angelloz, et al., 2000))
C	8.3×10^5m s^{-1}	The melting contraction rate (Fitting parameter)
H_∞	0.25	The saturated crystallinity (From Kweon et al. (Kweon, et al., 2003))
Mechanical behaviors		
γ_{Syl}	0.51	Stress concentration factor of Sylgard (Fitting parameter)
γ_{PCL}	4.31	Stress concentration factor of PCL (Fitting parameter)
N	2.16×10^{26} m^{-3}	Polymer crosslinking density (From DMA for neat Sylgard)
μ	20.69MPa	PCL crystal phase modulus (Fitting parameter)

Thermal contraction/expansion		
α_1	2.66×10^{-4} ℃$^{-1}$	CTE at high temperature (Measured from experiment)
α_2	8.27×10^{-5} ℃$^{-1}$	CTE at low temperature (Measured from experiment)
$\Delta\lambda_{PT}$	-1.16×10^{-2}	Thermal strain due to phase transition (Fitting parameter)

The numerical simulation of a constrained recovery experiment as described above was also conducted to characterize the constrained recovery feature of the constitutive model. Fig. 19 shows the comparison between the numerical simulation and the experiment. The model predicts the constrained recovery of the material very well. Two peaks of strain at different temperature are also described due to hysteresis of crystallization and melting.

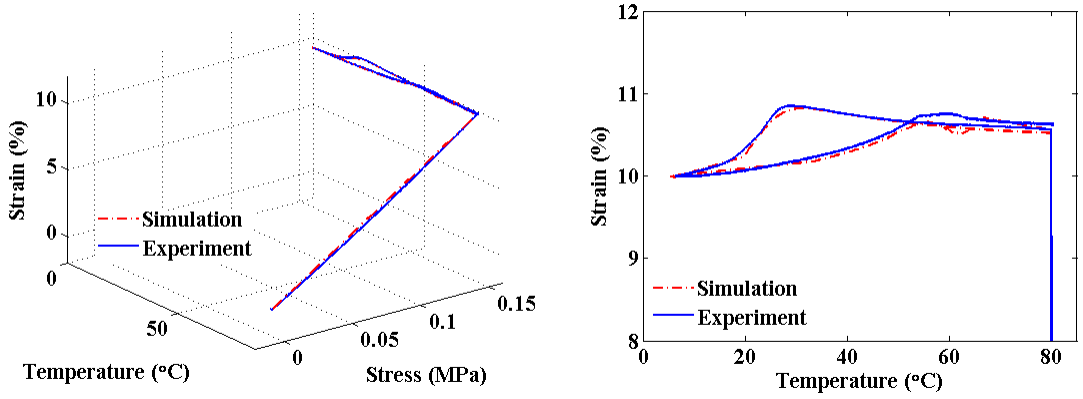

(a) (b)

Fig. 19 Comparison between model predictions and experiments for the case of imposed stress 0.15MPa. (a) Stress-Temperature-Strain plot. (b) Strain-Temperature plot.

2.4.3 Effect of thermal rates

The constitutive model with parameters fitted by the 0.15MPa with 2 ℃/min case was used to investigate the effect of thermal rates. The model predicts the behaviors of other three thermal rates (Fig. 20) with a very good agreement with experiments. Fig. 21 shows crystallization under different thermal rates from model predictions. Clearly, crystallinity plays a key role in determining the fixity upon unloading. For the slow cooling cases, such as 1 ℃/min and 2 ℃/min cases, crystallization occurs at a faster rate than the cooling rate and can reach the

saturated crystallinity, and therefore the best fixity can be achieved. For the fast cooling cases, crystallization occurs at a slower rate than the temperature rates, therefore, upon unloading, crystallinity only reach 5% and 2%, respectively, leading to a poor fixity: the 5 ℃/min case held about 60% temporary shape and the 10 ℃/min case just fixed about 40%. In addition, for the 5 ℃/min and 10 ℃/min cases, it is observed that crystallinity keeps growing at low temperature during heating, since the temperature is lower than the crystallization temperature.

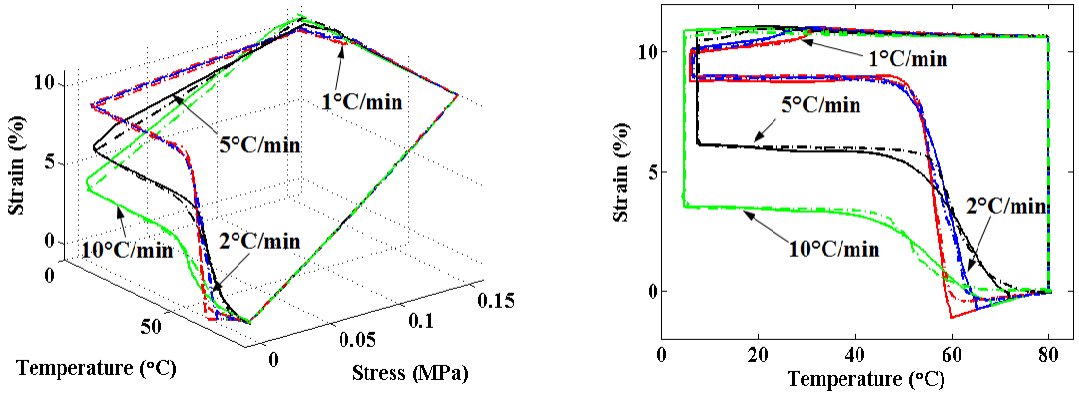

(a) (b)

Fig. 20 Comparison between simulations and experiments of shape memory behavior with different thermal rates (1 ℃/min (red), 2 ℃/min (blue), 5 ℃/min (black) and 10 ℃/min (green)): (a) Stress-Temperature-Strain plot. (b) Strain-Temperature plot. Solid lines represent simulations and solid-dot line represents experiments.

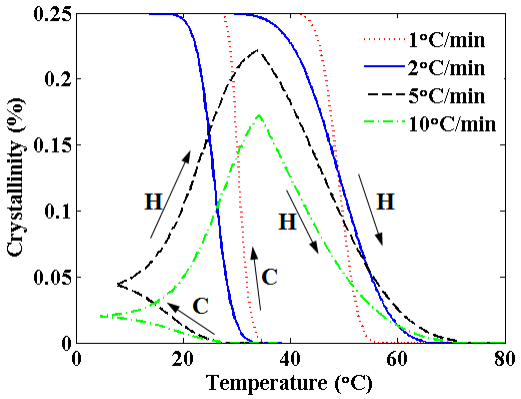

Fig. 21 Simulations of kinetics under different thermal rates (“C” represents “Cooling”, “H” represents “Heating”).

2.4.4 Effect of volume fractions

As mentioned in Section 2.3, the fixing capability of SMEC can be affected by changing the Sylgard/PCL composition. The effect of volume fraction of PCL on the ability of fixing temporary shape was investigated here by the constitutive model.

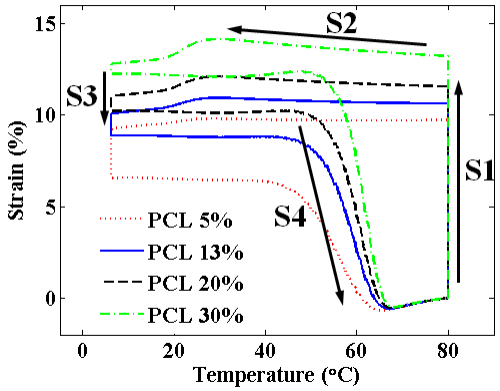

Fig. 22 Strain-Temperature plot with different volume fraction of PCL with 0.15MPa.

Fig. 22 shows model predictions of different shape memory behaviors on 0.15MPa imposed stress by varying volume fraction of PCL from 5% to 30%. At S1, the sample will be stretched more with higher percentage of PCL, since higher percentage of PCL leads to softer SMEC stiffness at T_H due to lower percentage of Sylgard. At S3, upon unloading, higher volume fraction of PCL yields less strain drop and better fixity. Therefore, the advantage of higher PCL fraction is the better fixity. However, higher PCL can also lead to softer material behavior at high temperatures. Table 3 lists the fixing ratios R_f and the strains ε_H at T_H. Clearly, the fixing ratio increases with the volume fraction of PCL, nevertheless the strain ε_H at T_H increases, because the composition of Sylgard decreases as increasing the one of PCL and due to Eq. (17), only Sylgard carries load at T_H, the less Sylgard, the softer the material.

Table 3. List of R_f and ε_H

v_{PCL}	5%	13%	20%	30%
R_f	70.4%	88.4%	93.9%	95.4%
ε_H	9.73%	10.72%	11.71%	13.23%

2.5 Conclusion

Shape memory behaviors of a novel SMEC are investigated in this paper. In the SMEC system, Sylgard as an elastomeric matrix provides rubber elasticity and PCL serves as a reversible "switch phase" due to the crystal-melt transition, imparting shape memory ability into the system. This paper investigates the thermomechanical behaviors of SMEC and presents a first 3D constitutive modeling frame to describe the shape memory effects of SMECs. This modeling frame includes kinetics of non-isothermal crystal-melt transition of PCL, mechanical and thermal behaviors The kinetics for the crystal-melt transition utilizes the Evans theory and Hoffman-Lauritze expression for crystallization then expands Hoffman-Lauritze expression to consider melting. The kinematics of evolving phases is tracked by using the assumption that newly formed the crystalline phase is undeformed and stress-free. In order to improve the computational efficiency, the effective phase model (EPM) is adopted to capture the mechanics of material with evolving phases. The model accurately captures shape memory behaviors and is used to discuss effects of thermal rates and volume fractions. The model is also used to explore the effects of volume fraction and thermal rates.

CHAPTER III

MECHANISMS OF TRIPLE-SHAPE POLYMERIC COMPOSITES DUE TO DUAL THERMAL TRANSITIONS

3.1 Introduction

Along with strong interests in dual-shape SMPs, such as SMECs which have two shapes, namely the temporary shape and the permanent shape, multi-shape SMPs have started to attract increasing attention. To date, there are two approaches to achieve a multi-shape memory effect (m-SME). The first approach requires the SMP to have a wide temperature range of thermomechanical transition. For example, Xie (Xie, 2010) recently demonstrated that perfluorosulphonic acid ionomer (PFSA), a thermo-plastic SMP with a broad glass transition temperature range from 55 ℃ to 130 ℃, could show m-SME, if the temperature is increased during recovery in a staggered manner. Using a simple theoretical model, we found that the physical mechanism of this observed m-SME is due to the multiple relaxation modes of macromolecular chains, these relaxation modes being sensitive to temperature (Westbrook, et al., 2011). At a particular temperature during recovery, some relaxation modes are active (meaning their relaxation time is comparable with lab time scale) while some other relaxation modes are not (meaning their relaxation time is extremely long as compared to lab time scale). If the temperature is increased in a staggered manner, the number of active relaxation modes also increases in a staggered manner, leading to the observed m-SME.

The second approach is to use multiple transition temperatures to achieve m-SME, most notably, to use two distinct transition temperatures to obtain triple-shape memory effect (t-SME). Here, t-SME refers to fixing two temporary shapes and recovering sequentially from one temporary shape to the other upon continuous heating, and ultimately to the permanent shape (Bellin, et al., 2006, Bellin, et al., 2007, Luo and Mather, 2010, Xie, et al., 2009). In a typical thermomechanical triple-shape memory cycle (Fig. 2), at Step 1 (S1), the material is initially

deformed at a temperature T_H, where T_H is higher than two phase transition temperatures ($T_{trans\ I}$ and $T_{trans\ II}$). At Step 2 (S2), the temperature is decreased to T_{L1} ($T_{L1} < T_{trans\ I}$), while maintaining the external load and fixing associated with the higher temperature transition begins. After removal of the external load, at Step 3 (S3), fixing of the first temporary shape at T_{L1} is revealed. At Step 4 (S4), the sample is deformed further at T_{L1} (note: this need not be in the same direction or in the same plane as the first deformation). At Step 5 (S5), the material is cooled to T_{L2} ($T_{L2} < T_{trans\ II}$), while keeping the external load causing the deformation at S4. At Step 6 (S6), after unloading, the second temporary shape is fixed at T_{L2}. At Step 7 (S7), as the sample is heated back to T_{L1}, the material recovers into its first temporary shape. At Step 8 (S8), the permanent shape is reached by heating to T_H.

Recently, several methods of achieving the t-SME were reported. Bellin and co-workers (Bellin, et al., 2006, Bellin, et al., 2007) developed two different polymer networks to achieve the t-SME. These two network systems are macroscopically homogeneous with two microscopic polymer segments. The two phase transitions are either glass transition of one segment and crystal-melt transition of the other one, or two crystal-melt transitions of two different segments. Xie (Xie, et al., 2009) reported a different method of achieving the t-SME using a macroscopic bilayer crosslinked polymer structures with two well separated phase transitions. Recently, based on the fabrication of shape memory elastomeric composites (SMECs) (Luo and Mather, 2009), Luo and Mather (Luo and Mather, 2010) introduced a new and broadly applicable method for designing and fabricating triple shape polymeric composites (TSPCs) with well controlled properties. In the TSPC, an amorphous SMP (epoxy with $T_g \approx 20$ ℃ – 40 ℃, depending on the precise composition) works as the matrix providing overall elasticity and provides one phase transition temperature and non-woven PCL (poly(ε-caprolactone)) microfibers produced by electrospinning and incorporated into the matrix provides the other phase transition temperature

due to the crystal-melt transition of PCL (T_m ≈50 °C). Compared with methods reported previously, the approach for fabricating polymeric composites is quite flexible, since one can tune the functional components separately to optimize material properties, opening up the potential to design for a variety of applications (Luo and Mather, 2010).

Constitutive models were also developed in the past for SMPs. These models were mainly for dual-shape SMPs, including the early model by Tobushi et al. (Tobushi,Hayashi, et al., 1996), the modified standard linear solid model with Kohlrausch-Williams-Watts (KWW) stretched exponential function by Castro et al. (O'Connell and McKenna, 1999), three dimensional finite deformation models for amorphous SMPs developed by Liu et al. (Liu, et al., 2006), Qi et al. (Qi, et al., 2008a), Nyugen et al. (Nguyen, et al., 2008), Chen and Lagoudas (Chen and Lagoudas, 2008a, b), Westbrook et al. (Ge,Luo, et al., 2012); constitutive models for crystallizable shape memory polymers were developed by Barot and Rao (Barot and Rao, 2006), Westbrook et al. (Westbrook,Parakh, et al., 2010), and Ge et al for SMEC (Ge,Luo, et al., 2012). For multi-shape SMP, Yu et al. (Westbrook, et al., 2011) demonstrated that a multi-branch model can be used to capture the m-SME in SMPs with a broad range of transition temperature. For the t-SME with dual transition temperatures, to the authors' best knowledge, no model has been reported to date.

This paper investigates the triple-shape memory behavior of TSPC and presents a one-dimension (1D) model to describe the tripe-shape memory behavior. In the model, the macroscopic behavior of the composite depends on two phases the composite made up of. Each phase of the composite can undergo individual phase transition (the glass transition for the matrix and the crystal-melt transition for the fiber network) and contributes to the macroscopic behavior. The model separately considers the glass transition and crystal-melt transition. This separate treatment allows the material parameters used in the model to be independently identified from experiments. The parameter identification approaches are proposed and the necessary tests are

described. The paper is arranged in the following manner: In Section 2, the material is introduced briefly and experimental results including DMA, stress relaxation tests, uniaxial tension tests and triple-shape memory behaviors are presented. Section 3 introduces the 1D model. In Section 4, parameter identification is introduced and, with parameters having been determined by experiments, simulations of stress and stored energy analysis for the triple-shape memory behavior are presented.

3.2 Materials and thermomechanical behaviors

3.2.1 Materials

A TSPC was prepared using an epoxy-based copolymer thermoset system as the matrix and a poly(ε-caprolactone) (PCL) as fiber reinforcements. For the epoxy-based copolymer thermoset system, it consists of an aromatic diepoxide (diglycidyl ether of bisphenol-A or DGEBA), an aliphatic diepoxide (neopentyl glycol diglycidyl ether or NGDE) and a diamine curing agent (poly(propylene glycol) bis (2-aminopropyl) or Jeffamine D230) (Luo and Mather, 2010). In this paper, the mole-% ratio DGEBA: NGDE=30:70 or D30N70 was chosen for all tests. The fabrication is similar with previously reported shape memory elastomeric composites (SMECs) (Luo and Mather, 2009, 2010).

3.2.2 DMA experiments

DMA tests were conducted using a dynamic mechanical analyzer (Q800 DMA, TA Instruments). The epoxy/PCL TSPC (a 11.65 mm×1.7 mm×0.43 mm rectangular film) was stretched by a dynamic tensile load at 1Hz. The temperature was first cooled at a rate of 1 ℃/min from 100 ℃ to -50 ℃, then after 10 min thermal equilibrating at -50 ℃, it was heated up to 100 ℃ at a rate of 1 ℃/min. Fig. 23 shows the tensile storage modulus with temperature. The heating trace and the cooling trace show different features. In the heating trace, it clearly shows two separated thermal transitions, corresponding to the glass-rubber transition of epoxy and the

crystal-melt transition of PCL, respectively. As a result, the cascade of three storage modulus plateaus of decreasing magnitude with increasing temperature was observed. The first high modulus plateau (~1.5 GPa) exists below epoxy T_g^{epoxy} attributed to the glassy state of epoxy (Plateau I in Fig. 2). The second moderate modulus plateau (~10 MPa) lies between epoxy T_g^{epoxy} and PCL T_m^{PCL}, where epoxy is in rubbery state but PCL is in semicrystalline state (Plateau II in Fig. 23). Above PCL T_m^{PCL}, there is a low modulus plateau (~ 2MPa) (Plateau III, in Fig. 23). Different from the heating trace, during cooling, the rubber-glass transition of epoxy and the melt-crystal transition of PCL are largely merged into one single transition and Plateau II disappears. This is primarily attributed to two close temperature ranges of two transitions, and the supercooling that is inherent to polymer crystallization.

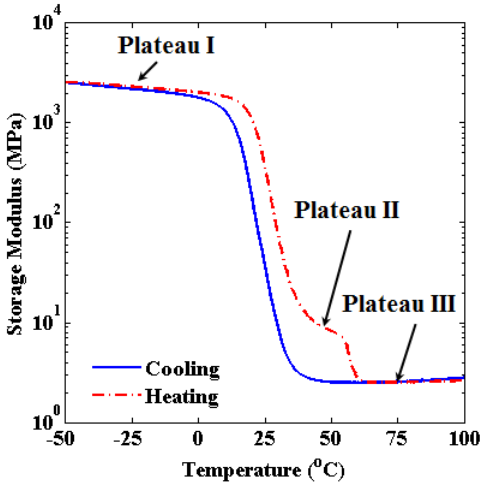

Fig. 23 DMA results for the epoxy/PCL TSPC: storage modulus with temperature during a cooling-heating cycle. During heating, the cascade of three storage modulus plateaus was observed. At Plateau I, the matrix (epoxy) is in the glassy state and the fiber network (PCL) is in the semicrystalline state. At Plateau II, the matrix is in the rubbery state, but the fiber network is still in the semicrystalline state. At Plateau III, the matrix is in the rubbery state and the fiber network is in the melting state. During cooling, Plateau II disappears.

3.2.3 Stress relaxation tests

Stress relaxation tests were conducted using the DMA machine in order to yield the viscoelastic data required material parameter estimations needed for our modeling. A rectangular

TSPC sheet with the dimension of 8.97 mm×1.71 mm×0.43 mm was used for tests. Stress relaxation tests were performed at 16 different temperatures evenly distributed from 0 ℃ to 30 ℃, a temperature safely below the melting point of the fiber network. The sample was preloaded by application of a small, 1×10^{-3} N force to maintain its straightness. After reaching the testing temperature, it was thermally equilibrated for 30 min. Then a 0.1% strain was applied to the sample and the relaxation modulus was observed for 30 min. Fig. 24 shows the results of stress relaxation for 16 different temperatures. Base on the well-known time temperature superposition principle (TTSP) (Brinson, 2007, Rubinstein and Colby, 2003), a relaxation master curve was achieved by shifting relaxation curves to a reference temperature of $T_{ref}=16°C$, with temperature-dependent shifting factors. The relaxation master curve and shifting factors will be reported in Section 4.

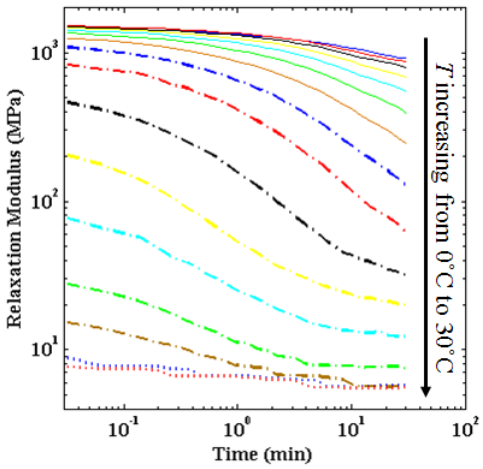

Fig. 24. Tensile relaxation modulus for temperatures varying from 0 ℃ (indicate color or insert line) to 30 ℃ (indicate color or insert line) with 2 ℃ temperature intervals between experiments.

3.2.4 Uniaxial tension tests

The uniaxial tension tests for both the neat epoxy and the TSPC were conducted using the DMA machine. The dimensions of the neat epoxy sample and the TSPC sample were 9.09 mm×1.8 mm×1.44 mm and 9.97 mm×1.97 mm×0.5 mm, respectively. Both samples were tested

at 40 ℃ and 80 ℃ respectively, at the loading rate of 0.5 MPa/min. The results of uniaxial tensions were used for parameter identification, which will be introduced in Section 4.1.

3.2.5 Shape memory behavior

Shape memory behaviors were tested on the DMA machine with a 10.69 mm×2.25 mm×0.42 mm rectangular film. The t-SME was achieved by following an eight-step-shape-fixing method proposed by Luo and Mather (Luo and Mather, 2010): at Step 1 (S1), the material is initially stretched at a stress rate of 0.5 MPa/min to a constant load P_1 at a temperature T_H ($T_H > T_g^{epoxy}, T_m^{PCL}$). At Step 2 (S2), the material is cooled down at a rate of 2 ℃/min to a temperature T_{L2} ($T_{L2} < T_g^{epoxy}, T_m^{PCL}$) while maintaining the load P_1. At Step 3 (S3), it is heated up at a rate of 2 ℃/min to a temperature T_{L1} ($T_g^{epoxy} < T_{L1} < T_m^{PCL}$). At Step 4 (S4), after unloading, the first temporary shape is fixed at T_{L1}. At Step 5 (S5), the material is stretched at the same stress rate of S1 to a constant load P_2 (P_2>P_1) and the material is at a new deformation state. At Step 6 (S6), it is cooled down to T_{L2} again, while keeping the constant load P_2. At Step 7 (S7), after unloading, the material achieves the second temporary shape at T_{L2}. Finally, at Step 8 (S8), the material is heated up to T_{L1} and it recovers to its first temporary shape and permanent shape sequentially. In this paper, this approach is used where T_H is 80 ℃, T_{L1} is 40 ℃ and T_{L2} is 0 ℃. It is emphasized that the cooling to T_{L2} at S2 and the heating to T_{L1} at S3 are necessary to distinguish the two separated phase transitions: at S2, epoxy is in glassy state and PCL is in semicrystalline state and at S3, PCL is still in semicrystalline state but epoxy is in rubbery state. The strain-temperature plots are shown in Section 4 with three different nominal stress pairs (P_1=0.1 MPa, P_2=0.3 MPa; P_1=0.15 MPa, P_2=0.45 MPa; P_1=0.2 MPa, P_2=0.6 MPa).

As reported by Luo and Mather (Luo and Mather, 2010), the triple-shape behavior can be achieved by a so called “one-step-fixing” method. In order to better understand the mechanism on

how to achieve two temporary shapes after a single fixing step, the material was tested by the "one-step-fixing" method. The material was stretched at a rate of 0.5 MPa/min to 0.2 MPa at 80 ℃ and then cooled down to 0 ℃ at a rate of 2 ℃/min, while maintaining the load; after quickly unloading at 0 ℃, almost 100% strain was fixed. During heating, it is quite interesting that there is a strain plateau at ~40 ℃-60 ℃, and at 80 ℃, the material was able to completely recover into its permanent shape. In Section 4, we will show that three shapes can be observed: one at 0 ℃, one at between 40 ℃ and 60 ℃, and finally one at 80 ℃.

3.3 Model description

3.3.1 Overall model

In this section, a one dimensional (1D) model is developed to capture the t-SME in the epoxy/PCL composites and to clearly understand the mechanism of shape fixing, stress and strain energy distribution during a shape memory cycle. In this model, the matrix and fiber network are treated as a homogenized system. The macroscopic behavior of system depends on the two phases (the matrix and the fiber network). The matrix as an amorphous SMP undergoes the glass transition and the fiber network as crystallizable polymer undergoes the crystal-melt transition. The fiber network is a liquid (melt) at high temperatures and an elastic solid at low temperature, where melts and crystals co-exist and their respective volume fractions depend on the temperature and their evolutions are described by the existing theory of crystallization. As the model is primarily focusing on the shape fixing mechanism, we do not seek a rigorous micromechanical description. In addition, the thermal expansion is not introduced for this 1D model, although it can be easily included. (Ge,Luo, et al., 2012)

For the TSPC system, the simplest model arranges stresses on the matrix and the fiber network in parallel (as shown in Fig. 25) and the total Cauchy stress σ^{total} is given by:

$$\sigma^{total} = V_M \sigma^M + V_F \sigma^F, \tag{50}$$

where σ^M and σ^F are the stresses acting on the matrix and the fiber network, V_M and V_F are the effective volume fractions of the matrix and the fiber network by considering the departure of stress distribution among the phases, which are a multiplication of stress concentration factors and volume fractions for the matrix and the fiber network, respectively, and $V_M + V_F = 1$. (Ge,Luo, et al., 2012)

Fig. 25 shows a rheological representation of the model. In Fig. 4, the left red dashed box represents the stress acting on the matrix. A modified Standard Linear Solid (SLS) model is adopted to consider both equilibrium and nonequilibrium behaviors of the matrix. Here, a spring is used to represent the equilibrium behavior and a KWW (Kohlrausch, Williams and Watts) stretched exponential function for stress relaxation is used to represent the nonequilibrium viscoelastic response (Williams and Watts, 1970). The right blue dashed box represents the mechanical elements for the fiber network behavior. The fiber network changes its crystallinity with temperature: when $T > T_m$, fiber melts do not carry load; when $T < T_m$, fibers crystallize and can carry load.

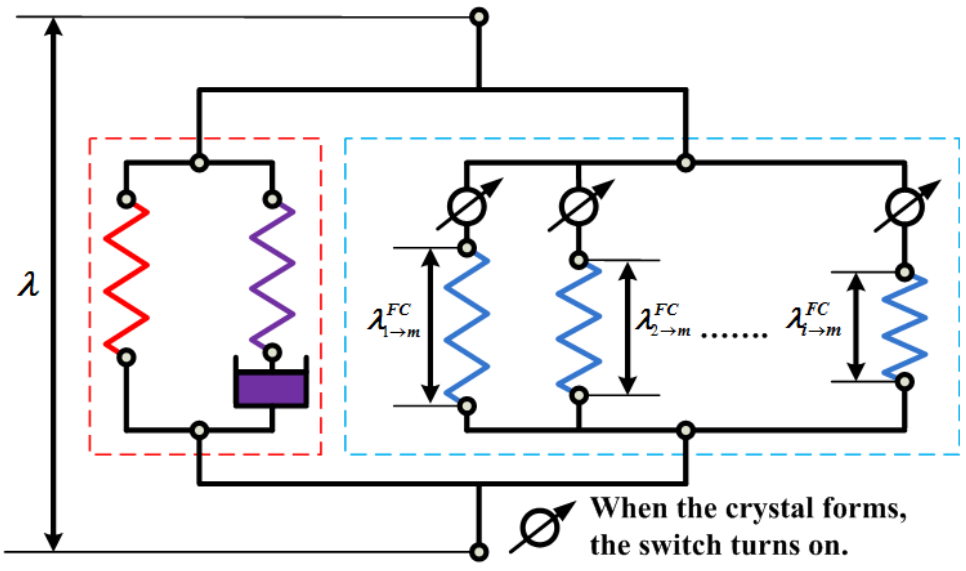

Fig. 25. Schematic of overall model: the total Cauchy stress consists of stresses on the matrix (red dashed box, left) and stress on fiber network (blue dashed box, right). For the stress on the matrix, a modified Standard Linear Solid (SLS) model is adopted to consider the equilibrium and

nonequilibrium behaviors of the matrix. The multiple springs of the fiber network model represents fiber crystals formed at different times. When fibers crystallize, the switch turns on and crystals appear with modulus, μ; when fibers melt, the switch turns off and fibers lose their modulus.

3.3.2 Viscoelastic behavior for the matrix

For the matrix, the modified SLS model is used to consider both equilibrium and nonequilibrium viscoelastic behaviors. The total stress on the matrix consists of contributions from both equilibrium and nonequilibrium behaviors:

$$\sigma^{M}(T,t)=\sigma^{eq}(T)+\sigma^{non}(T,t). \tag{51}$$

The Cauchy stress from the equilibrium response $\sigma^{eq}(T)$ follows the neo-Hookean model with entropic elasticity:

$$\sigma^{eq}(T)=NkT\left(\lambda^{2}-1/\lambda\right), \tag{52}$$

where N is the crosslink density of the matrix, k is Boltzmann's constant, T is absolute temperature and λ is the stretch along the uniaxial load. $\lambda=1+\varepsilon$ and ε is the strain. For the nonequilibrium response, the stress should be:

$$\sigma^{non}(t)=E_{non}\varepsilon_{e}(t), \tag{53}$$

where E_{non} is Young's Modulus and ε_{e} is the elastic strain of the nonequilibrium branch. Using KWW stretched exponential and Boltzmann superposition principle, ε_{e} can be (Xie, et al., 2009):

$$\varepsilon_{e}(t)=\int_{0}^{t}\frac{\partial\varepsilon}{\partial s}\exp\left[-\left(\int_{s}^{t}\frac{dt'}{\tau(T,t')}\right)^{\beta}\right]ds\,, \tag{54}$$

where ε is the total strain in the nonequilibrium $\varepsilon=\varepsilon_{e}+\varepsilon_{v}$, ε_{v} is the viscous strain, $\tau(T)$ is the temperature dependent stress relaxation time. β is a material parameter within a range between 0 and 1 characterizing the width of the stress relaxation distribution, i.e. a decrease of β leads to an increase of the stress relaxation breadth. Once β reaches 1, it is the narrowest stress relaxation

time distribution and the nonequilibrium branch is reduced to the original Maxwell model. The temperature dependent stress relaxation time $\tau(T)$ is obtained using a shifting factor a_T:

$$\tau(T) = a_T \tau_0 , \tag{55}$$

where τ_0 is the stress relaxation time at a reference temperature. It was found that depending on whether temperature is above and near or below T_g, the shifting factor a_T can be calculated by two different methods (O'Connell and McKenna, 1999). For temperature above and near T_g, the WLF (Williams-Landel-Ferry) equation (Williams, et al., 1955) is used:

$$\log a_T = -\frac{C_1 (T - T_r)}{C_2 + (T - T_r)} , \tag{56}$$

where C_1 and C_2 are material constants, and T_r is a reference temperature. For temperature below T_g, an Arrhenius-type behavior developed by Di Marzio and Yang et al. (1997) (Di Marzio and Yang, 1997) is used:

$$\ln a_T = -\frac{A F_C}{k}\left(\frac{1}{T} - \frac{1}{T_r}\right), \tag{57}$$

where A is material constant, F_c is the configuration energy and k is Boltzmann's constant.

3.3.3 Mechanical behavior of the fiber network

For the semicrystalline fiber network, crystallization and melting are functions of temperature and time. We adopt the postulation that when a small fraction of polymer crystals forms, it is in a stress-free state (Long, et al., 2010, Westbrook,Parakh, et al., 2010). However, in order to satisfy the boundary conditions, either overall or locally, this small fraction will deform immediately. This stress-free state for new formed crystalline phases was referred as natural configuration by Rajagapol (Rajagopal and Srinivasa, 1998a, b), and has been used by many researchers to study crystallizing polymers (Ma and Negahban, 1995a, Ma and Negahban, 1995b,

Negahban, 1993, Negahban and Wineman, 1992), rubbers with thermally induced scissoring and reformation (Tobolsky, 1960, Wineman, 1999, 2005, Wineman and Min, 2000, 2003, Wineman and Shaw, 2008), shape memory polymers (Barot and Rao, 2006, Barot, et al., 2008, H. Jerry Qi, et al., 2008), and light induced activated polymers (Long, et al., 2009). Following this assumption, the stress in the fiber networks is (Long, et al., 2010):

$$\sigma^{F} = \int_{t_c}^{t} \dot{v}(s)\sigma^{FC}\left[\lambda^{FC}(t-s)\right]ds\,, \tag{58}$$

where t_c is the time point when crystallization starts, $\lambda^{FC}(t-s)$ is the stretch of the fiber crystals formed at $t=s$ and $v(s)$ is the crystallinity of crystalline phases, which is a function of time and temperature and is discussed below; σ^{FC} is the stress function for fiber crystals. For the sake of simplicity, it simply assumes the stress on fiber crystals follows neo-Hookean behavior and the Cauchy stress is:

$$\sigma^{FC} = \mu_C\left(\lambda^2 - 1/\lambda\right), \tag{59}$$

where μ_C is the shear modulus of fiber crystals. The incremental description for stress on the fiber network during crystallization and melting was reported. (Ge,Luo, et al., 2012)

To describe crystallization kinetics (Avrami, 1941, 1939, 1940), a simplified Avrami's phase transition theory is used. In polymer crystallization, the time-temperature dependent crystallinity of polymer, $v(T,t)$, can be expressed as (Ge,Luo, et al., 2012):

$$v(T,t) = H_\infty\left\{1-\exp\left[-V(T,t)\right]\right\}, \tag{60}$$

where H_∞ is the saturated crystallinity of a polymer under a certain condition, for PCL network H_∞ is taken as 25% (Ge,Luo, et al., 2012) and $V(T,t)$ is the volume fraction of crystalline phases without impingement. The calculation of $V(T,t)$ during crystallization or melting was discussed in Ge et al. (Ge,Luo, et al., 2012).

3.3.4 Strain energies

Strain energies on the matrix and the fiber network were used to investigate the shape fixing mechanism. For the equilibrium branch of the matrix and fiber crystals, as both of them adopt the Neo-Hookean constitution, the strain energy on the equilibrium branch of the matrix and individual fiber crystals is:

$$W = \pm\mu\left(I_1 - 3\right), \tag{61}$$

where μ is the shear modulus and equal to NkT for the matrix and equal to μ_C for fiber crystals; I_1 is the first deformation invariant, for the uniaxial loading case, $I_1 = \lambda^2 + 2/\lambda$. The "$\pm$" sign is used to distinguish tensile (+) or compressive (-) loading. For the strain energy of the fiber crystals, it follows:

$$W^F = \int_{t_c}^{t} \dot{v}(s) W\left(t - s\right) ds\,. \tag{62}$$

For the nonequilibrium branch of the matrix, the strain energy follows:

$$W = \pm\frac{1}{2} E_{non} \varepsilon_e^2\,, \tag{63}$$

where E_{non} is Young's Modulus and ε_e is the elastic strain of the nonequilibrium branch introduced in Eq. (54).

3.4 Results

3.4.1 Parameter identification

In the model, there are 11 parameters in total (see Table 4). They were determined by uniaxial tension and stress relaxation experiments. Specifically, uniaxial tension tests were used to determine the crosslinking density N of the matrix (epoxy), shear modulus of fiber crystals (PCL), and effective volume fractions V_M and V_F. Stress relaxation tests were used to identify the relaxation time τ_0 at 16 ℃, KWW stretching parameter β, the Young's modulus for nonequilibrium branch E_{non}, and constants in WLF equation and Arrhenius behavior.

Fig. 26 shows the results from uniaxial tensile experiments of both the neat epoxy and TSPC at 80 ℃ (Fig. 5a) and at 40 ℃ (Fig. 26b). By fitting the experimental curve for the neat

epoxy at 80 ℃, the crosslinking density N was identified as $3.84\times10^{-23}\mathrm{m}^{-3}$. For the TSPC at 80 ℃, as the fiber network melts, $\sigma^{F}=0$. Therefore, the total stress is:

$$\sigma^{total}=V_M NkT(\lambda^2-1/\lambda). \tag{64}$$

By fitting the TSPC curve at 80 ℃ (Fig. 5a), we obtained V_M =0.47 and $V_F=1-V_M=0.53$. For the TSPC at 40 ℃, as the crystallization of PCL finishes before the test, the Cauchy stress follows:

$$\sigma^{total}=V_M NkT\left(\lambda^2-1/\lambda\right)+V_F H_\infty \mu_C\left(\lambda^2-1/\lambda\right). \tag{65}$$

In Eq. (65), only the shear modulus μ_C for PCL crystals is unknown and can be determined easily by fitting the uniaxial tension for TSPC at 40 ℃. Fig. 26b shows the fitting result with $\mu_C=9.2\mathrm{MPa}$.

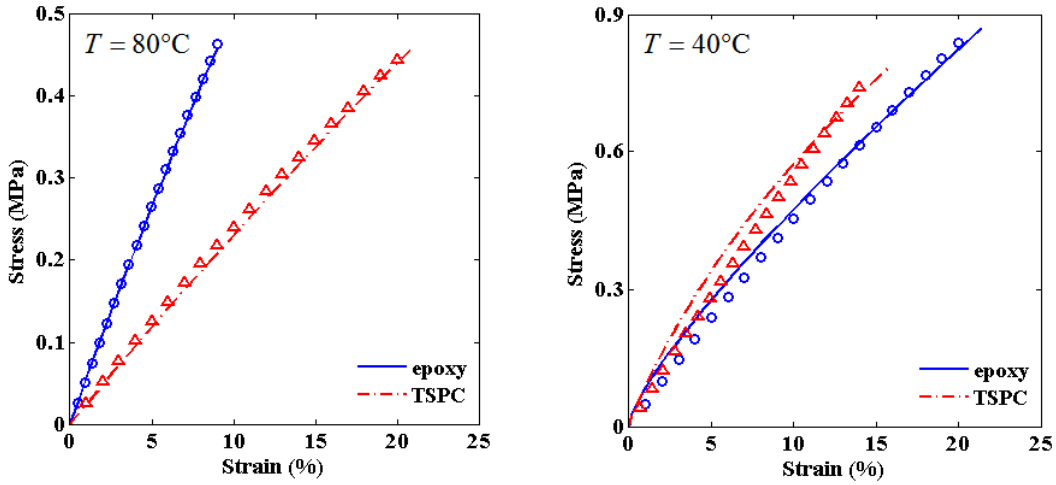

(a) (b)

Fig. 26. Model fitting for uniaxial loadings: (a) at 80 ℃; (b) at 40 ℃. (Blue circles represent the model fitting for the neat epoxy; red triangles represent the model fitting for the TSPC).

Based on the time-temperature superposition principle, a relaxation master curve at 16 ℃ (Fig. 6a) can be achieved by shifting individual relaxation curves with shifting factors at different temperatures (Brinson, 2007, Rubinstein and Colby, 2003). The relaxation master curve can be described by a modified standard linear solid model with KWW stretch exponential, where the stress relaxation modulus should be:

$$E(t) = E_0 + E_1 \exp\left[-\left(\frac{t}{\tau_0}\right)^{\beta}\right]. \tag{66}$$

In Eq. (66), at time $t = 0$, $E(0) = E_0 + E_1$ and when t approaches ∞, $E(\infty) = E_0$. From Fig. 27a, we have E_0 =8MPa ($E(\infty)$) and E_1 =1480MPa ($E(0) - E_0$). By considering the effective volume fraction of the matrix, the Young's modulus of the nonequilibrium branch is $E_{non} = E_1 / V_M$ and therefore E_{non} =3150MPa. Using Eq. (66) to fit the stress relaxation master curve at 16 ℃, parameters τ_0 and β are determined as 110s and 0.3, respectively. As introduced in Section 3, the shifting factors as functions of temperature can be described by WLF and Arrhenius equations at different temperature ranges. By fitting shifting factors with these two equations (Fig. 27b), parameters in Eqs. (56) and (57) are determined as C_1 =24, C_2 =50 ℃, T_r =16 ℃ and AF_c / k =-35000K.

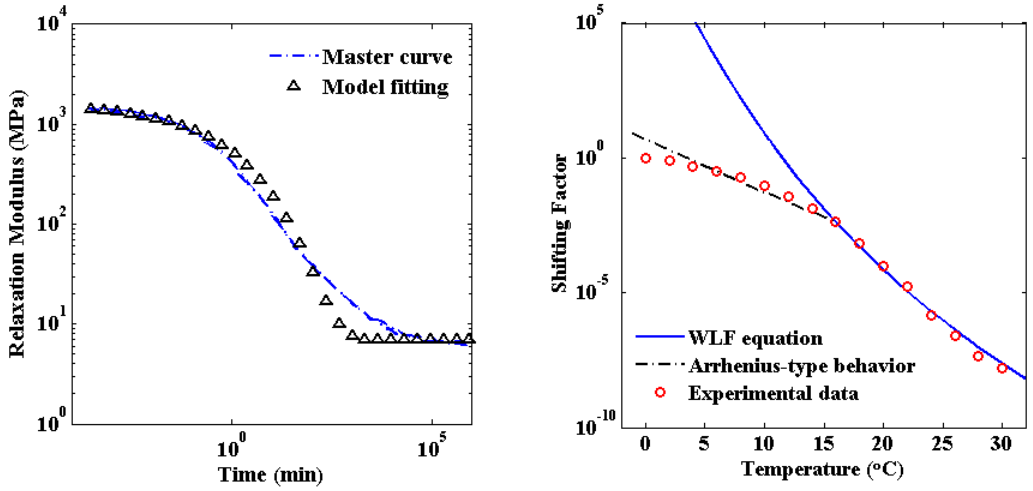

(a) (b)

Fig. 27 Model fitting for stress relaxation: (a) the stress relaxation master curve at 16 ℃; (b) the shifting factors with temperature.

Table 4. List of material parameters

Parameters	Value	Description
Composition		

V_M	0.47	Effective volume fraction of the matrix (epoxy)
V_F	0.53	Effective volume fraction of the fiber networks (PCL)
Epoxy Matrix		
N	$3.84\times10^{-23}\mathrm{m}^{-3}$	Polymer crosslinking density
E_{non}	3150MPa	Young's modulus for nonequilibrium branch
τ_0	110s	Relaxation time at 0 ℃
β	0.3	KWW stretching parameter
T_r	16°C	Reference temperature
C_1	24	WLF constant
C_2	50°C	WLF constant
AF/k	−35000K	Pre-exponential parameter for Arrhenius-type behavior
PCL Fiber Network		
μ_C	9.2MPa	Shear modulus for PCL crystals

3.4.2 Comparison between model simulations and experiments

Using parameters in Table 4, the model successfully predicts the triple-shape memory behavior under three different nominal stress pairs (P_1=0.1 MPa, P_2 =0.3 MPa; P_1=0.15 MPa, P_2 =0.45 MPa; P_1=0.2 MPa, P_2 =0.6 MPa) (Fig. 28). It should be noted that these curves were not used for parameter identification. In Fig. 28, the model predictions show good agreement with experiments and the largest discrepancy occurs at S4 unloading to achieve the first temporary shape and at S8 heating back to ~40 ℃ to recover to the first temporary. We attribute this error primarily to the nonlinear deformation for the TSPC at 40 ℃, which the neo-Hookean model for PCL crystals is unable to satisfactorily represent. The faster relaxation modulus in the model fitting (Fig. 27a) makes the model predictions reach the first temporary at S8 earlier than experiments.

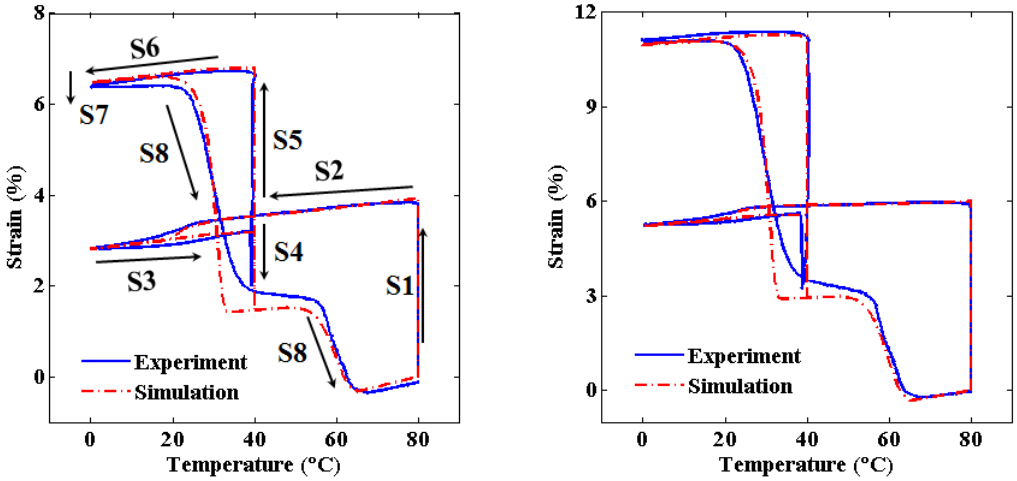

(a)

(b)

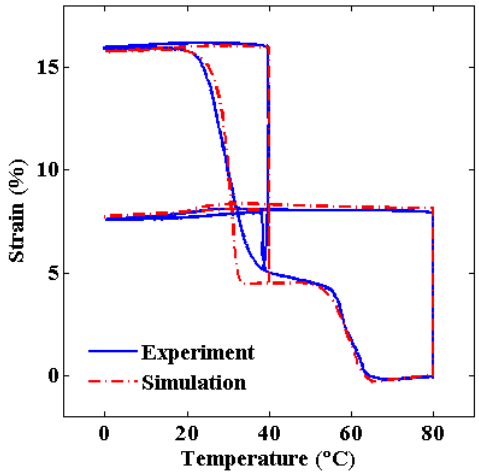

(c)

Fig. 28 Model predictions for triple-shape memory behavior under three different nominal stress pairs: (a) P_1=0.1 MPa, P_2 =0.3 MPa; (b) P_1=0.15 MPa, P_2 =0.45 MPa; (c) P_1=0.2 MPa, P_2 =0.6 MPa.

The model also predicted the one-step-fixing shape memory behavior introduced in 2.4 with the 0.2 MPa imposed stress case (Fig. 29). Briefly, following high temperature deformation, then direct cooling to 0 ℃ and subsequent unloading, almost 100% strain was fixed. During continuous heating, recovery is interrupted as the strain reaches a plateau between T_g^{epoxy} and T_m^{PCL}, and then completes as T_m^{PCL} is surpassed. In Fig. 29, the model prediction shows good agreement with the experiment, indicating that the essential physics are captured.

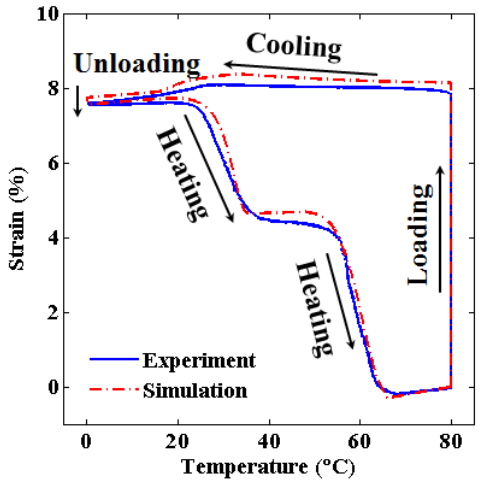

Fig. 29 Comparisons between model predictions and experimental result for the one-step-fixing shape memory behavior.

3.4.3 Stress and strain energy analyses for the triple-shape memory behavior

In order to better understand the mechanism of fixing temporary shapes, stress evolution and strain energy for the t-SME under the 0.15-0.45 MPa stress pair were investigated. Fig. 30a provides the thermomechanical loading history. Fig. 30b shows the variation of the strain as a function of time. In Fig. 30c and e, the total stress is decomposed into the stress acting on the matrix and the stress acting on the fiber network. At S1, all stress comes from the matrix since the fiber network (PCL) is in melt state. In addition, because the matrix is in its rubbery state, the stress on the matrix mainly comes from the equilibrium branch; the stress on the nonequilibrium branch is almost zero due to large viscous strain developed, indicating the nonequilibrium branch is active for the subsequent shape memory effect. At S2 and S3, although crystals in the fiber network formed gradually, stress contribution from the fiber network is negligible due to small deformations on fiber crystals. At S4, after a quick unloading, the strain contracts ~50% (at S4 in Fig. 30b), which leads to a decrease of stress on the equilibrium branch of the matrix and the introduction of a compressive stress on the fiber network. Thus, the overall force balance is achieved and the total stress is zero. It is clear that the compressive stress on the fiber network

prevents the matrix from returning to its stress-free (or initial) state. At S5 (the second loading), stresses on the matrix and the fiber network increase. At S6 (second cooling with holding a constant stress), stresses on the matrix and the fiber network stay constant. At S7 (unloading), stresses on the fiber network and on the equilibrium branch decrease slightly, but the stress on the nonequilibrium branch of the matrix changes quickly to a negative value, thus to prevent the material from recovery and maintain the force balance. At S8, during heating, viscosity on the nonequilibrium branch decreases, causing the decrease of the compressive stress on this branch. When the stress on the nonequilibrium branch decreases to zero, the material recovers to the first temporary shape and the stresses on the equilibrium branch and the fiber network return to the same values at S4. As the temperature is further increased to above the melting temperature, the stress on the fiber network starts to decrease; when fiber crystals completely melt, the material recovers to its initial shape.

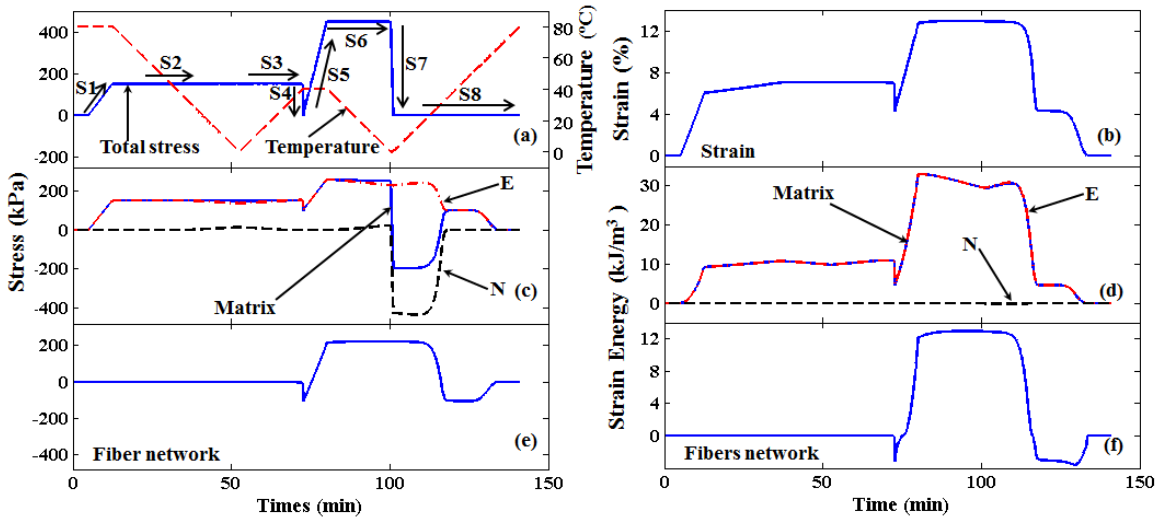

Fig. 30 Stress and strain analyses for the triple-shape memory behavior: (a) the thermomechanical loading history (stress and temperature vs time). (b) Experimental output (strain). Total stress can be decomposed into the stress on the matrix (c) and the stress on the fiber network (e). The stress on the matrix (c) can be further decomposed into the one on the equilibrium branch ("E") and the one on the nonequilibrium branch ("N"). (d) provides the strain energy on the matrix, which can be decomposed into the one on the equilibrium branch ("E") and the one on the nonequilibrium branch ("N"). (f) provides the strain energy the fiber network. In (d) and (f), the strain energy is taken as negative if the deformation is compressive.

Fig. 30d and f show the variation of strain energy in the material. Comparing Fig. 30d and f, at S1, S2 and S3, the strain energy on the fiber network is nearly zero and most strain energy is from the equilibrium branch of the matrix. After the first unloading at S4, the strain energy on the equilibrium branch of the matrix drops and the strain energy on the fiber network is instantaneously generated to a negative value (due to compression). The energy release from the matrix is stored in the fiber crystals and a strain energy loss of ~3 kJ/m^3 (corresponding a 30% of loss) is observed. At S5 (loading at 40 ℃), the strain energies on both the matrix and the fiber network increase. At S6 (cooling to 0 ℃), the strain energy on the matrix decreases slightly, but that of the fiber network remains nearly constant. Upon unloading at S7, the strain energies on the equilibrium branch and the fiber network change slightly by transferring the energy to the nonequilibrium branch in the form of compressive energy (-0.2 kJ/m^3). During heating at S8, the strain energy stored on both the fiber network and the matrix decreases and the nonequilibrium branch returns to zero when the material returns to the first temporary shape. Further heating the material to above its melting temperature, the energies stored on the fiber network and equilibrium branch decrease to zero and the material recovers to its permanent shape. It is also noted that since fiber crystals have a higher modulus than the equilibrium branch, the energy stored in the second temporary shape is much higher than that stored in the first temporary shape. For the material studied here, the energy stored in the second temporary shape is 42.6 kJ/m^3, which is 430% higher than that in the first temporary shape (8 kJ/m^3).

3.4.4 Stress and strain energy analyses for the one-step-fixing shape memory behavior

Similarly with the triple-shape memory behavior, stress and strain energy analyses were investigated for the one-step-fixing shape memory behavior. Fig. 31a provides the thermomechanical loading history. Fig. 10b shows the variation of the strain as a function of time. In Fig. 31c and e, the total stress is decomposed into the stress acting on the matrix and the stress

acting on the fiber network. During the loading step, all stress comes from the matrix since the fiber network (PCL) is in melt state. In addition, because matrix is in its rubbery state, the stress on the matrix mainly comes from the equilibrium branch; the stress in the nonequilibrium branch is almost zero due to large viscous strain developed, indicating the nonequilibrium branch is active for the subsequent shape memory effect. At the cooling step, although crystals in the fiber network formed gradually, stress contribution from the fiber network is negligible due to small deformations on the fiber network. During unloading, stresses on the fiber network and on the equilibrium branch decrease slightly, but the stress on the nonequilibrium branch of the matrix changes quickly to a negative value, thus to prevent the material from recovery and maintain the force balance. During heating from 0 ℃ to ~40 ℃, viscosity on the nonequilibrium branch decreases, causing the decrease of the compressive stress on this branch. When the stress on the nonequilibrium branch decreases to zero, the material arrives at a strain plateau from ~40 ℃ to 60 ℃ (Fig. 31b) and the compressive stress on the fiber network maintains the force balance, which indicates part of the strain is fixed by compressed the fiber crystals. As the temperature is further increased to exceed the melting temperature, the stress on the fiber network starts to decrease; when fiber crystals completely melt, the material recovers to its initial shape.

Fig. 31d and f show the variation of strain energy in the material. Comparing Fig. 31d and f, at loading and cooling, the strain energy on fiber networks is nearly zero and most strain energy is from the equilibrium branch of the matrix. Upon unloading, the strain energies on the equilibrium branch and fibers networks change slightly by transferring the energy to the nonequilibrium branch in the form of compressive energy (-0.03 kJ/m^3). During heating from 0 ℃ to ~40 ℃, the strain energies stored on the matrix decreases and the nonequilibrium branch returns to zero when the material arrives at a strain plateau from ~40 ℃ to 60 ℃. At the strain plateau, the energy of the fiber network is negative, indicating that the energy released from the matrix is stored in the fiber crystals, and a strain energy release of ~5 kJ/m^3 is observed. Further

heating the material to above its melting temperature, the energies stored on the fiber network and equilibrium branch decrease to zero and the material recovers to its permanent shape.

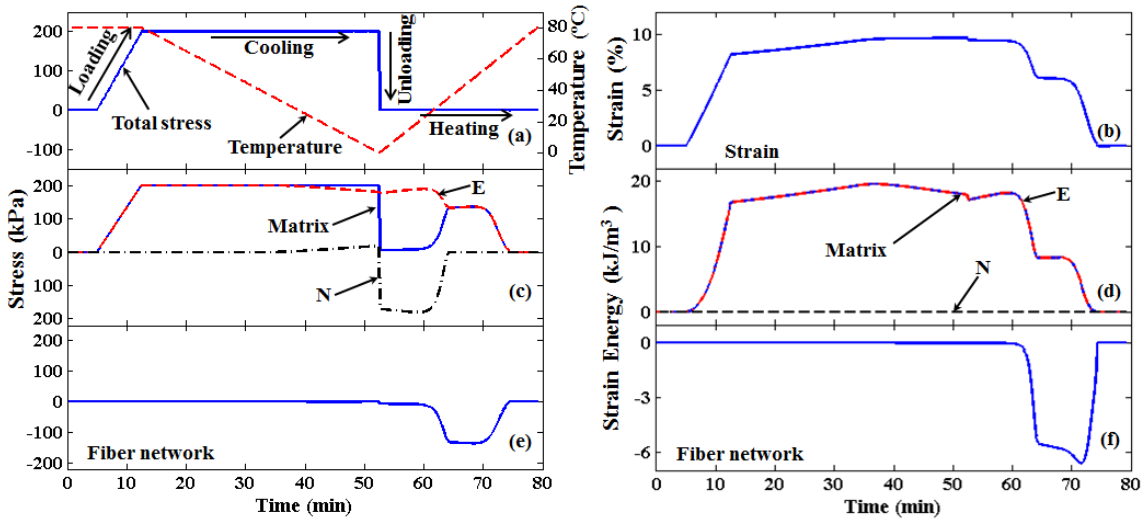

Fig. 31. Stress and strain analyses for the one-step-fixing shape memory behavior: (a) the thermomechanical loading history (stress and temperature vs time). (b) Experimental output (strain). Total stress can be decomposes the stress on the matrix (c) and the stress on fiber networks (e). The stress on the matrix (c) can be decomposed into the one on the equilibrium branch ("E") and the one on the nonequilibrium branch ("N"). (d) provides the strain energy on the matrix, which can be decomposed into the one on the equilibrium branch ("E") and the one on the nonequilibrium branch ("N"). (f) provides the strain energy fiber networks.

3.5 Conclusion

Triple-shape memory behaviors of TSPC were investigated in this paper. A 1D model was presented to describe the tripe-shape memory behaviors. The model separately considers the glass transition and melt-crystal transition. This separate treatment allows the material parameters used in the model to be independently identified from experiments. With parameters identified from stress relaxation tests and uniaxial isothermal tension tests, the model is able to predict the triple-shape memory behaviors and the one-step-fixing shape memory behavior. The stress and strain energy analyses from the model revealed clearly the shape fixing mechanisms for TSPC. For the triple-shape memory behavior, the first temporary shape is fixed by fiber crystals and the second temporary shape is fixed the nonequilibrium branch. For the one-step-fixing shape memory

behavior, the temporary shape is firstly fixed by the nonequilibrium branch at low temperature as the matrix in the glassy state. During heating, when the matrix transfers gradually from the glassy state to the rubbery state, the fiber network becomes deformed to fix a part of the temporary shape, which gives way to complete recovery upon further heating.

CHAPTER IV

PRINTED SHAPE MEMORY COMPOSITES

4.1 Introduction

Three dimensional (3D) printing or additive manufacturing is a process of making 3D solid objects from a digital model. Distinct from traditional machining techniques (subtractive processes relying on the removal of material by methods such as cutting and drilling), the 3D printing is realized by using additive processes and an objective is created by laying down successive layers of material. Since the start of the twenty-first century, the 3D printing technology has been developed rapidly and it is applied in a variety of the fields such as industrial design, footwear, jewelry, automotive, aerospace, dental and medical industries, etc.

In this chapter, we pursue the general idea of control of macroscopic shape memory behavior via control of the composite architecture by introducing a new paradigm enabled by recent advances in digital manufacturing of multimaterial architectures – printed shape memory composites (pSMCs). We present a method based on 3D printing to fabricate composite materials with precisely-controlled fiber architectures that lead to complex, anisotropic shape memory behavior. We demonstrate how anisotropic shape memory behavior derives in printed anisotropic shape memory elastomeric composites (ASMECs) consisting of an elastomeric matrix and oriented poly (ε-caprolactone) (PCL) fibers that undergo a melt-crystal phase transformation during heating or cooling. The controllable anisotropy in thermomechanical behaviors and shape memory behaviors are observed by tests, such as uniaxial tensions, the free thermal strain tests, and shape memory cycles. A 3D anisotropic thermomechanical constitutive model is developed to capture the observed anisotropic behaviors and can be used to guide the design of pSMC lamina and laminates.

This chapter is arranged in the following manner: In Section 2, the fabrication process of ASMECs is introduced. The thermomechanical tests for ASMECs are presented, including DMA tests, uniaxial tensions, shape memory behaviors and thermal strain tests. Section 3 introduces the

3D anisotropic thermomechanical constitutive model and the identification of the parameters used in the model. In section 4, the model predictions of shape memory behaviors are compared with the experimental results. The parametric studies such as the effect of volume fractions and the effect of the effective shear modulus of fibers are investigated.

4.2 Materials and experiments

4.2.1 PolyJet polymer jetting

The layer-by-layer fabrication approach is used in the 3D printing process. In the 3D printing, the drop-on-demand inkjet printing is employed to selectively deposit droplets of photopolymer directly onto a build platform. This direct 3D printing technique is referred to as PolyJet. For the OBJet 3D printer (OBJet 260 Connex), as the inkjet print heads are connected with separate material sources (material cartridges with two photopolymer solutions (Verowhiteplus and Tangoblackplus) are installed in the OBJet 3D printer), multiple material can deposited in a single layer and the materials graded can be created. In addition, a hydrophobic gel is used as a sacrificial material or support material for the fabrication of complex geometries. During the printing process, once a layer of droplets is deposited (64 μm in standard mode; 32 μm in high-resolution mode), a roller evens out the horizontal surface of the layer. After that, two UV lights pass over the printed layer multiple times to cure the photopolymer.

The PolyJet printing based on the layer-by-layer printing approach is well suitable for component embedding, as the components can be directly embedded in bulk, in powder or even in liquid form without destroying the previously printed layer. However, there are two inherent limitations in using the PolyJet to embedded components. First, as the PolyJet software does not have the function to define the deposition of the sacrificial material, one has to manually remove the deposited sacrificial material from the void where a component will be embedded. Secondly, as the print heads is just over the printed part at a clearance of 4 μm, embedded components cannot protrude from previously deposited layer, or the print head may be damaged.

4.2.2 Fabrication of printed shape memory composites

There are two approaches to reach printed shape memory composites (PSMCs) using the 3D printer: the first one is straight printing of multiple materials; the second one is a more complex hybrid printing/impregnation process with a sacrificial material and then a non-printed active material. For the first approach, as long as the composite is designed using a CAD software, it can be printed directed by the 3D printer. Later, several applications fabricated by this approach will be demonstrated. Here, we primarily introduce the fabrication of the anisotropic shape memory elastomeric composites (ASMECs), which were fabricated by the 3D printer using the second approach. The fabrication process follows six steps (Fig. 32): 1) Design the composite in CAD. 2) Print the structure on the 3D printer. In the ASMEC case, the Tangoblackplus is chosen as rubbery matrix material. 3) Along with the composite structure, an indicator is printed. Once the color or the shape of the indicator changes, it indicates that the channels completely form, and the printing process should be paused immediately. 4) Manually remove the sacrificial material from channels. 5) Fill the channels with PCL melt. This step needs to be operated at 80 ℃. 6) Resume the printing process to close up the channels. Composites with seven fiber orientations (0 °, 15 °, 30 °, 45 °, 60 °, 75 ° and 90 °) were made.

Fig. 32c takes the 90 ° fiber orientation to introduce the geometry of the composite. The sample has dimension 25 mm×7 mm ×3mm (length ×width ×thickness). The coordinate system x-y-z is the globe coordinate system, where the x-axis along the length direction and the y-axis along the width direction. The coordinate system 1-2-3 is the local coordinate system. Originally, for the 0 ° fiber orientation case, the 1-, 2-, 3-axes are coincident with the x-, y-, z-axes, respectively. In an arbitrary θ, using the 3-axis as a rotation axis, the 1-axis is rotated counterclockwise from x-axis by θ. In the 90 ° fiber orientation case, the 1-axis is rotated counterclockwise by 90 ° and coincident with the y-axis. A zoomed in figure for a repeating unit is used to introduce the size of fibers. The dimension of the entire cross section is 2ΔL×3ΔL (here,

ΔL=1mm). The fibers with square cross section b ×b. In the real sample, each end of the holes is sealed by a 0.25mm thick "cap" to prevent PCL melt from leaking. Regardless of the size of these "caps", the volume fraction of fibers is: $v_f = b^2/6\Delta L^2$. In following tests, b is taken to be ΔL and v_f becomes 1/6 (16.7%). b taken to be 0.7ΔL, where v_f is 8.2% is used to investigate the effect of volume fraction.

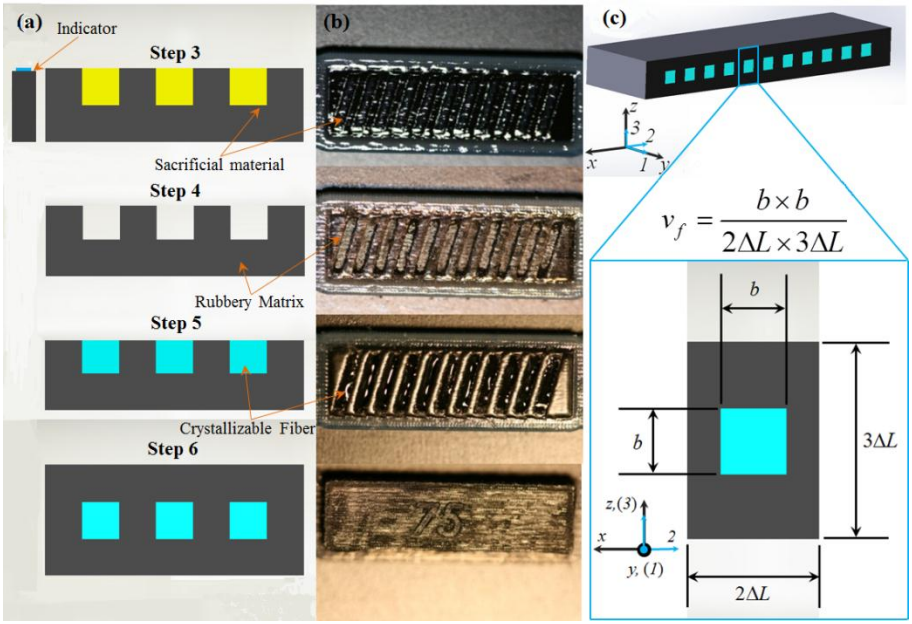

Fig. 32 The fabrication of ASMECs: (a) schematics of the fabrication steps. (b) The corresponding photos of the fabrication steps in (a). (c) The schematics of the geometry of the composites.

4.2.3 DMA tests

DMA tests were conducted using the DMA machine for the seven fiber orientation cases and the neat rubbery matrix material (Tangoblackplus). For the composite with seven fiber orientations, the dimension of the samples is ~15mm×7mm×3mm. For the neat rubbery matrix material, the dimension is 15mm×5mm×2mm. Before tests, samples were held at 30 ℃ for 60 min to make fibers (PCL) in the composite crystallized. Then, it was heated from 30 ℃ to 100 ℃ at a rate of 2 ℃/min. Fig. 33 shows storage modulus vs temperature for the eight cases. The melting

temperature (T_m) of these composites is ~63 ℃. The storage moduli of composites with seven orientations follow the order: 0 °>15 °>30 °>90 °>75 °>45 °>60 °.The storage modulus of the neat rubbery matrix material (RM) slightly increases as the temperature increasing, which indicates that in the temperature range the neat rubbery matrix material is in the rubbery state. The storage modulus of the neat rubbery matrix material is larger than the one of all composites above T_m, and it is lower than all composites below T_m as fibers in composites crystallized.

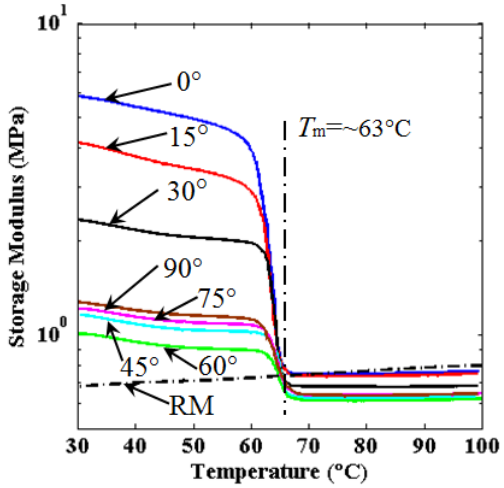

Fig. 33 The DMA results for the ASMECs with seven different fiber orientations and the neat rubbery matrix material.

4.2.4 Uniaxial tension tests

Uniaxial tension tests were conducted using the DMA machine for the neat PCL at 30 ℃, and for the ASMECs with seven fiber orientations at 30 ℃ and 80 ℃, respectively. For uniaxial tension tests at 30 ℃, before the tests were performed, the samples (for the neat PCL with dimension 7.5mm×1.9mm×1.3mm and for ASMECs with dimension ~15mm×7mm×3mm) were held at 30 ℃ for 60 min to make sure PCL crystallized. For the neat PCL, it was stretched at a stress rate of 8MPa/min to 8MPa; For the ASMECs, they were stretched at a stress rate of 0.2MPa/min to 0.2MPa. Fig. 34a and b show the stress-strain behavior of the neat PCL and the ASMECs at 30 ℃. All of them exhibit nonlinear plastic deformation at large deformation. For

uniaxial tension tests for ASMECs at 80 ℃, the samples were held at 80 ℃ for 60 min to make PCL completely melted. The samples were stretched at a stress rate of 0.05MPa/min to 0.05MPa. Fig. 34c shows the stress-strain behavior of the ASMECs at 80 ℃, which shows a good linearity for all composites. Fig. 34d presents the comparison of Young's Modulus for ASMECs between 30 ℃ and 80 ℃. Fig. 34e presents the comparison between DMA tests and uniaxial tensions for ASMECs. Circles represent Young's modulus at 30°C and triangles represent Young's modulus at 80 ℃. The DMA tests and uniaxial tensions show good agreement.

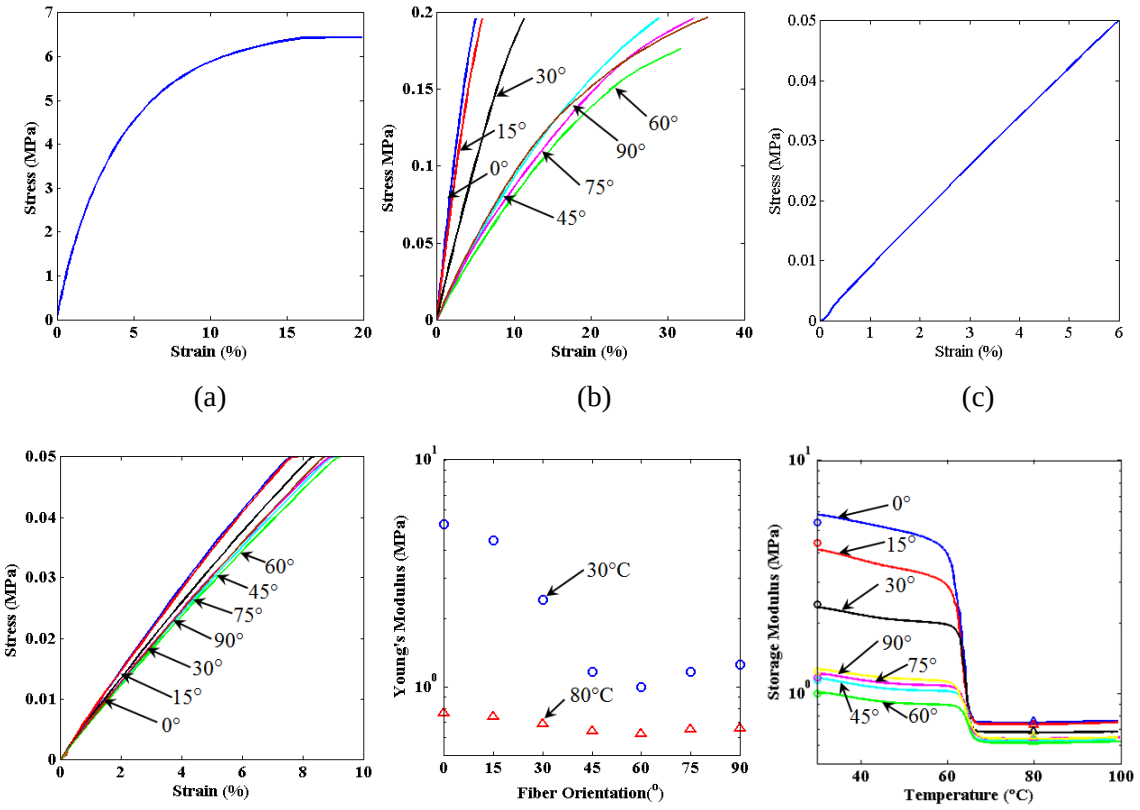

Fig. 34 Uniaxial tensions: (a) uniaxial tension for the neat fiber crystal (PCL) at 30 ℃. (b) Uniaxial tensions for the ASMECs at 30 ℃. (c) Uniaxial tensions for the neat rubbery matrix material at 80 ℃. (d) Uniaxial tensions for the ASMECs at 80 ℃. (e) Young's modulus vs fiber orientation for ASMECs at 30°C and 80°C, respectively. (f) Comparison between Young's modulus obtained from the uniaxial tensions (triangles represent the results at 30 ℃ and circles represent the results at 80 ℃.) and the storage modulus from DMA tests of ASMECs.

4.2.5 Shape memory behaviors

The SM behaviors of the ASMEC were investigated on the DMA machine. Fig. 35a shows the thermomechanical cycle under which the shape memory behavior was performed. In Fig. 35b, take the 0 °fiber orientation case for instance: at step 1 (S1), the sample was stretched at 80 ℃ (T_H) by gradually ramping the tensile stress at a loading rate 0.05MPa/min to 0.05MPa. At step 2 (S2), the temperature was decreased to 30 ℃ (T_L) at a rate of 2 ℃/min while the nominal stress was fixed. It shows that when lowering the temperature, the strain initially increased. At step 3 (S3), it was isothermally held at 30 ℃ for 60 min to crystallize PCL fibers. During the isothermal crystallization, an about 1% nonlinear strain drop was observed. At step 4 (S4), the stress was quickly released at 30 ℃ and most of the deformation was fixed. At step 5 (S5), the strain recovery was triggered by heating back to 80 ℃ at a rate of 2 ℃/min. The strain was first linearly increased from 30 ℃ to ~55 ℃. Then, the strain suddenly dropped to ~-0.4% at the temperature between ~55 ℃ to 65 ℃. From 65 ℃ to 80 ℃, the strain linearly recovered to zero. Fig. 35c shows the shape memory behavior for ASMECs with seven fiber orientations and for the neat rubbery matrix materials. Eq. (1) was used to calculate the fixity R_f. Table 5 lists the fixity for the eight cases. Fig. 35d shows the fixity vs fiber orientations. For ASMECs, between 0 °to 45 °, the fixity decreases dramatically as increasing the degree of fiber orientation; as the fiber orientation higher than 45 °, the fixity stays around ~40% and the lowest case happens at 60 °. Interestingly, for the neat rubbery matrix material which does not have the shape memory effect, its fixity is supposed to be zero. However, the experiment presented a negative value.

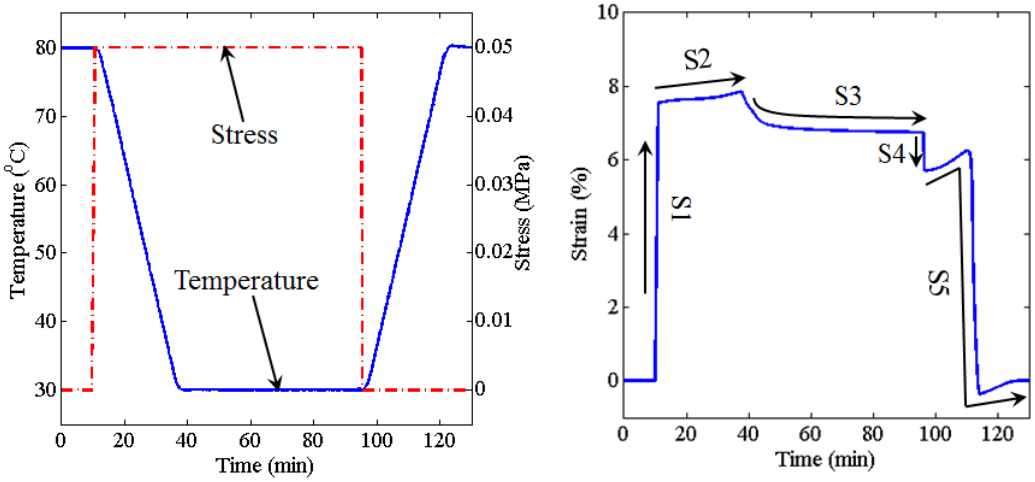

(a) (b)

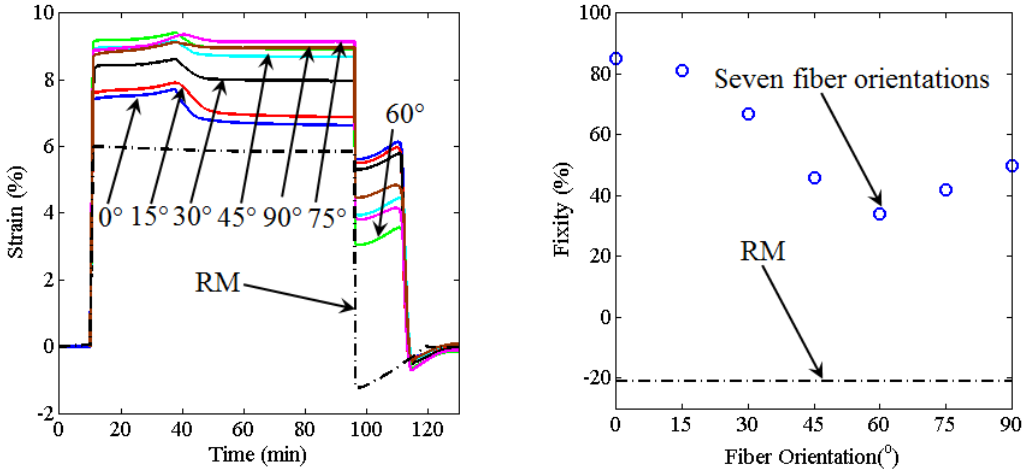

(c) (d)

Fig. 35 Shape memory behaviors for ASMECs and the neat rubbery matrix material: (a) thermomechanical condition to achieve the shape memory behaviors. (b) the time vs strain plot for the 0 ° fiber orientation is used to demonstrate the shape memory behavior. (c) the time vs strain plot for all seven fiber orientation cases of ASMECs and the neat rubbery matrix material. (d) the fixity vs fiber orientation for the ASMECs with seven fiber orientations and the neat rubbery matrix material.

Table 5. List of R_f with different fiber orientations

	0 °	15 °	30 °	45 °	60 °	75 °	90 °	RM
R_f	85%	80%	67%	46%	34%	42%	50%	-21%

4.2.6 Thermal strain tests

The thermal strain tests were conducted using the DMA machine. Fig. 36a presents the thermomechanical condition for the thermal strain test. During the entire test, a tiny static force (0.01N) was applied to maintain the straightness of the sample. The temperature was firstly decreased from 80 ℃ to 30 ℃ with the rate of 2 ℃/min. Then, it was held isothermally for 60min. After that, it was heated back to 80 ℃ at the same rate of cooling. Fig. 36b shows the thermal strain vs time for ASMECs and the neat rubbery matrix material. In order to better demonstrate the thermal strain, the thermal strain vs temperature was shown in Fig. 36c. Fig. 36d takes the 0 ° fiber orientation case for example to describe the thermal strain during the test. During cooling

from 80 ℃ to 30 ℃, the ASMEC with PCL melts contracts linearly with the coefficient of thermal expansion (CTE) α_m. During isothermal crystallization at 30 ℃, it nonlinearly contracts by ε_{PT}. During heating, it firstly expands linearly with CTE α_c, then expands nonlinearly by ε_{PT}, and finally expands linearly with CTE α_m.

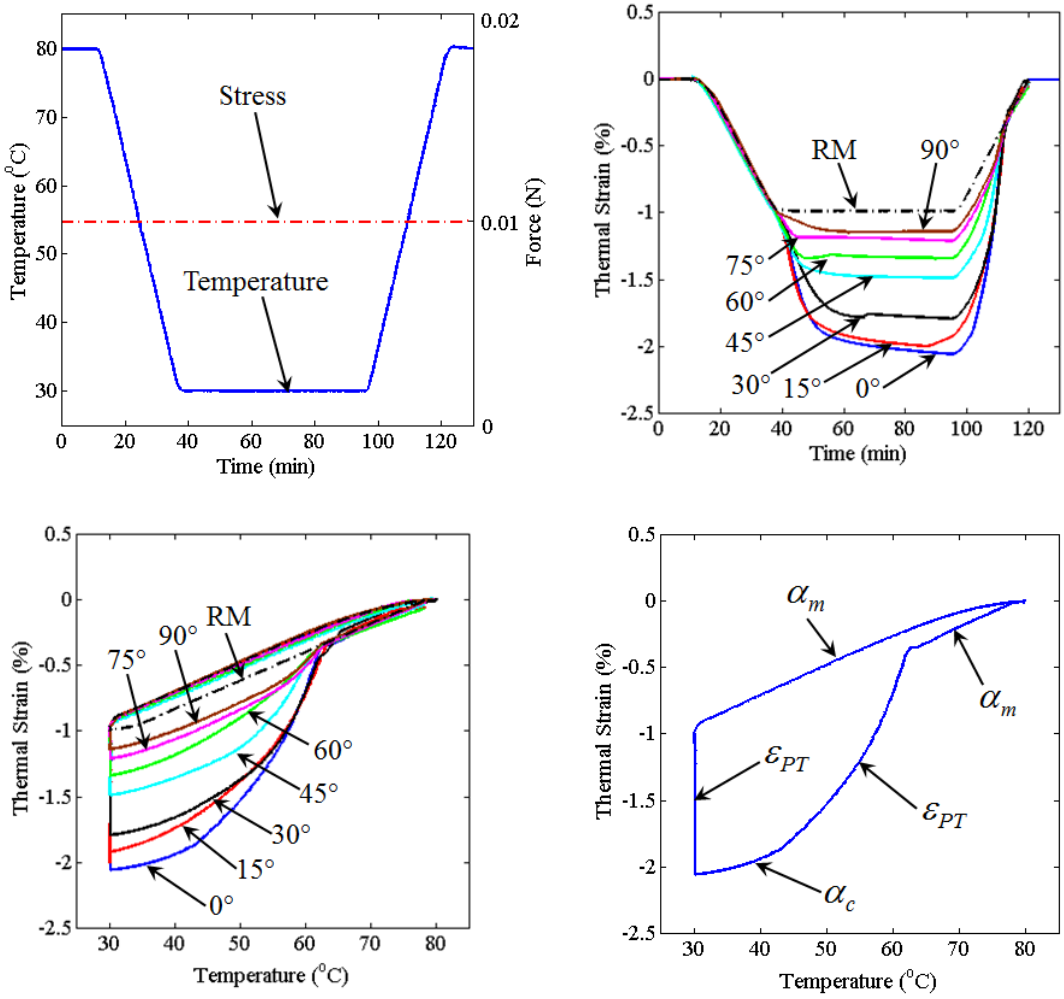

Fig. 36 Thermal strain tests: (a) the thermomechanical condition to achieve the thermal strain under a stress free thermal cycle. (b) the thermal strain plot vs time plot for the ASMECs with seven fiber orientations and the neat rubbery matrix material. (c) the thermal strain vs temperature plot for the ASMECs with seven fiber orientations and the neat rubbery matrix material. (d) the thermal strain vs temperature plot for the 0 ° fiber orientation plot is used to describe the thermal strain.

4.3 Model description

4.3.1 Constitutive model for anisotropic composites

In this paper, an anisotropic nonlinear elastic constitutive models for fiber reinforced composites proposed by Guo (Guo, et al., 2006, 2007) was adopted to describe the mechanical response of the ASMEC system. The model developed by Guo treats both matrix and fibers are incompressible neo-Hookean hyperelastic model. The model decomposes deformation gradient into two parts: the first part is comprised of uniaxial deformation along the fiber direction; the second part is comprised of all remaining deformation. The total strain energy can be constructed as:

$$W = \frac{1}{2}\mu_a\left(I_1 - 3\right) + \frac{1}{2}\mu_b\left(I_4 + I_4^{-1/2} - 3\right), \tag{67}$$

and the corresponding Cauchy stress is

$$\boldsymbol{\sigma} = -p\mathbf{I} + \underbrace{\mu_a\mathbf{B}}_{iso} + \underbrace{\mu_b\left(1 - I_4^{-3/2}\right)\mathbf{F}\mathbf{a}_0 \otimes \mathbf{F}\mathbf{a}_0}_{aniso}. \tag{68}$$

Here, $\mathbf{F}$ is the deformation gradient and $\mathbf{F}=\partial\mathbf{x}/\partial\mathbf{X}$. Here we use $\mathbf{X}$ to represent the position of a material particle in the original (undeformed) configuration, while $\mathbf{x}$ is the position of the corresponding particle in the current (deformed) configuration. $\mathbf{B}$ is the left Cauchy-Green deformation gradient and $\mathbf{B}=\mathbf{F}\mathbf{F}^{\mathrm{T}}$. $\mathbf{C}$ is the right green Cauchy-Green deformation tensor and $\mathbf{C}=\mathbf{F}^{\mathrm{T}}\mathbf{F}$. I_1 and I_4 are the principal invariants of $\mathbf{C}$: $I_1 = \mathrm{tr}\mathbf{C}$ and $I_4 = \mathbf{a}_0 \cdot \mathbf{C} \cdot \mathbf{a}_0 = \lambda_F^2$, where $\mathbf{a}_0$ is a unit vector represents the fiber orientation of the reinforced fiber in the original (undeformed) configuration and λ_F is the fiber stretch. In Eqs. (67) and (68), $\mu_a = \dfrac{\left(1-\nu_f\right)\mu_m + \left(1+\nu_f\right)\mu_f}{\left(1+\nu_f\right)\mu_m + \left(1-\nu_f\right)\mu_f}\mu_m$ and $\mu_b = \dfrac{\left(\mu_f - \mu_m\right)^2 \nu_m \nu_f}{\left(1+\nu_f\right)\mu_m + \left(1-\nu_f\right)\mu_f}$, where μ_m and μ_f are shear moduli of the matrix and the fibers, respectively; ν_m and ν_f are volume fractions of the matrix and the fibers and $\nu_m + \nu_f = 1$.

In Eq. (68), p is an arbitrary hydrostatic pressure, the second term is associated with the isotropic part of the Cauchy stress and the third term is associated with the anisotropic part of the Cauchy stress.

4.3.2 Parameter identification

In Eq. (68), the Cauchy stress can be calculated using four parameters (μ_m , μ_f , v_m and v_f). The volume fractions v_m and v_f are determined by design. As long as μ_m and μ_f are identified, the Cauchy stress can be computed.

In Fig. 37a, an incompressible Neo-Hookean model $\sigma = NkT\left(\lambda^2 - 1/\lambda\right)$ is used to fit the stress-strain behavior of the neat rubbery matrix material (tangoblackplus) at 80 ℃, where N is the crosslinking density, k is the Boltzmann's constant, and T is the temperature. Nk is identified as 0.822kPa/K. Thus, μ_m is 0.29MPa ($\mu_m = NkT,\ T = 353K$). In Fig. 37b, an incompressible Neo-Hookean model $\sigma = \mu_c\left(\lambda^2 - 1/\lambda\right)$ is used to fit the stress-strain behavior of the neat PCL at 30 ℃. The Neo-Hookean model is able to fit the linear part. After strain ~2%, the sample starts to perform nonlinear plastic deformation and the Neo-Hookean model is unable to characterize. μ_c is identified as 50MPa.

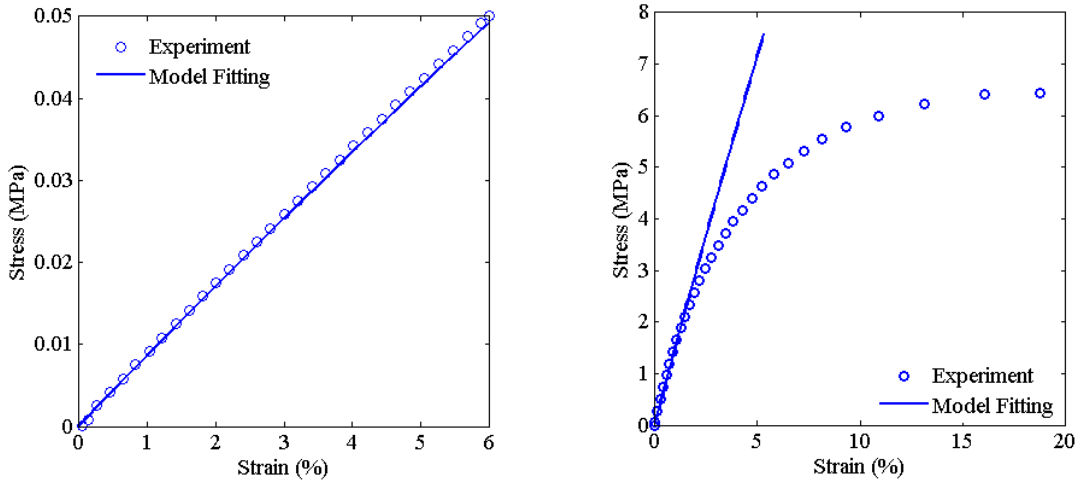

(a) (b)

Fig. 37 Uniaxial tensions are used to fit parameters in the model: (a) the uniaxial tension for the neat rubbery matrix material at 80 ℃ is used to identify Nk and Nk is 0.822kPa/K. (b) The uniaxial tension for the neat fiber crystals (PCL) at 80 ℃ is used to identify the shear modulus of fiber crystals μ_c and μ_c is 50MPa.

With $\mu_m = NkT = 0.25\text{MPa}$ ($T = 303K$), $\mu_f = \mu_c = 50\text{MPa}$, $v_m = 0.833$ and $v_f = 0.167$, Eq. (68) was used to predict the uniaxial tension of the $0°$ fiber orientation case at 30 ℃. Fig. 38a shows the comparison between experiment and model prediction. The model prediction overestimates the stiffness of the composite. The reason for this overestimation is that the model assumes the matrix and fibers are perfectly bonded, however, in the real composite, the interaction between the matrix and fibers are not perfect and the load transfer between the matrix and fibers is not 100%. Considering the real interaction between the matrix and fiber, a parameter γ is introduced and the effective shear modulus of semicrystalline PCL in the composite becomes $\bar{\mu}_c = \gamma\mu_c$. In Eq. (68), $\mu_f = \bar{\mu}_c = \gamma\mu_c$. The uniaxial tension of the $0°$ fiber orientation case at 30 ℃ was used to fit γ. In Fig. 38b, the model is able to feature the stress-strain behavior at small deformation and γ is identified as 0.18.

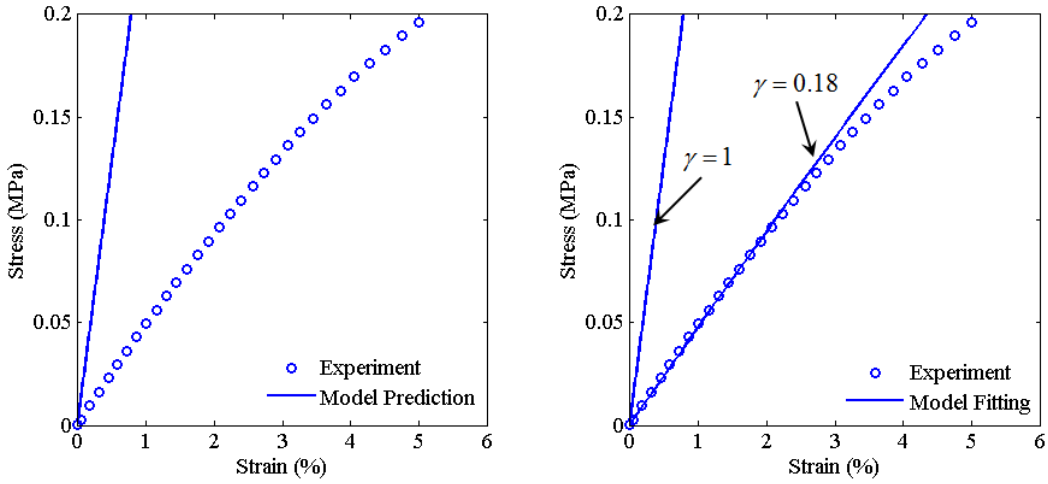

(a) (b)

Fig. 38 Model prediction and fitting for the uniaxial tension of the 0° fiber orientation case: (a) the model with $\mu_f = \mu_c = 50\text{MPa}$ is used to predict the uniaxial tension of the 0° fiber orientation case at 30 ℃. The model prediction overestimates the stiffness of the composite. (b) By fitting the uniaxial tension of the 0° fiber orientation case at 30 ℃, the parameter γ is identified as 0.18 and the effective shear modulus of the fiber in composite at 30 ℃ is 9MPa.

With $\mu_m = NkT = 0.25\text{MPa}$ ($T = 303K$), $\mu_f = \bar{\mu}_c = \gamma\mu_c = 9\text{MPa}$, $\nu_m = 0.833$ and $\nu_f = 0.167$, Eq. (68) was used to predict the uniaxial tensions of the other six fiber orientation cases at 30 ℃. Fig. 39 shows with $\gamma = 0.18$ or $\bar{\mu}_c = 9\text{MPa}$, the model is able to predict stress-strain behavior at small deformation. It is found that when the degree of the fiber orientation is high, the model is less sensitive to γ.

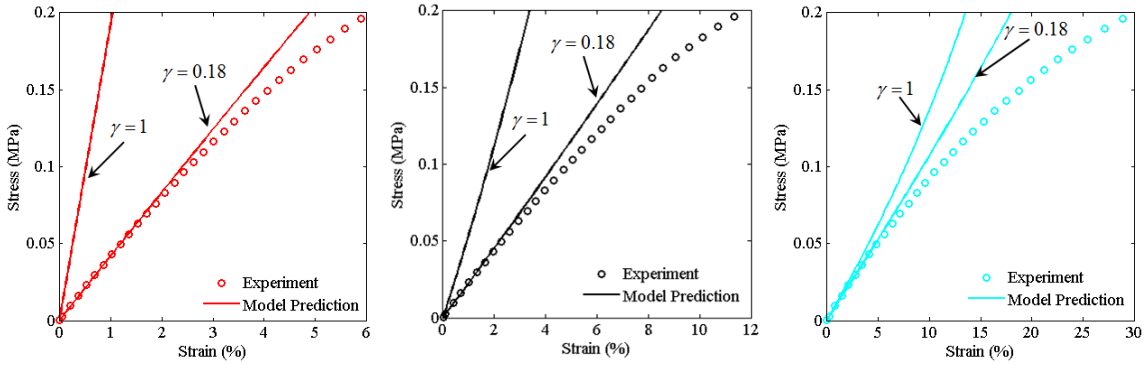

(a) (b) (c)

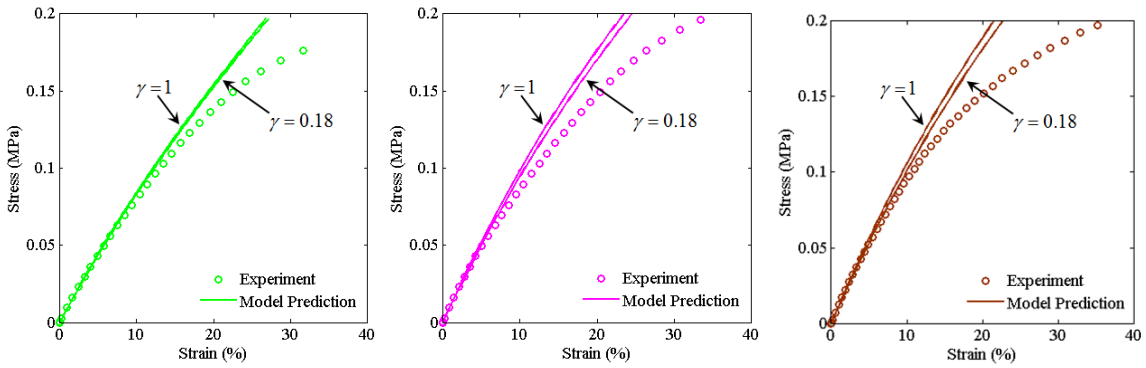

(d) (e) (f)

Fig. 39 The model with $\mu_f = 50\text{MPa}$ ($\gamma = 1$) and $\mu_f = 9\text{MPa}$ ($\gamma = 0.18$) predicts uniaxial tensions of other six fiber orientations at 30 ℃: (a) the 15 ° fiber orientation case. (b) The 30 ° fiber orientation case. (c) The 45 ° fiber orientation case. (d) The 60 ° fiber orientation case. (e) The 75 ° fiber orientation case. (f) The 90 ° fiber orientation case. The model with $\gamma = 0.18$ predicts the experimental results well at small deformation and the model is less sensitive to γ at the high degree fiber orientation case.

In Fig. 40, with $\mu_m = NkT = 0.29\text{MPa}$ ($T = 353K$), $v_m = 0.833$ and $v_f = 0.167$, the uniaxial tensions of the 0 ° fiber orientation case at 80 ℃ was used to fit μ_f (or $\bar{\mu}_c$) at 80 ℃ using Eq. (68). It turns out that μ_f (or $\bar{\mu}_c$) is nearly zero that implies the PCL melts contributes negligible stiffness to the entire composite at 80 ℃. With $\mu_f \approx 0$ at 80 ℃, Eq. (68) was used to predict the uniaxial tensions of the other six fiber orientation cases (Fig. 41). The model predicts the stress-strain behavior well.

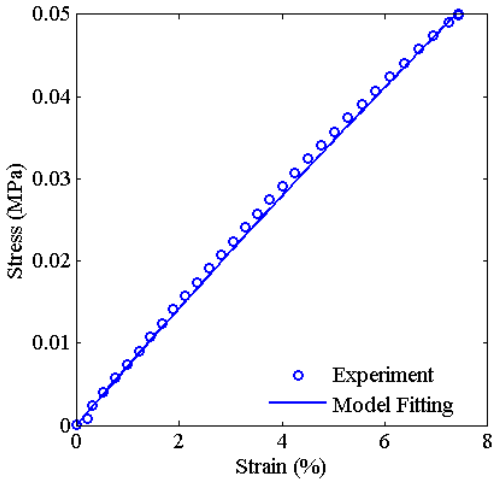

Fig. 40 The uniaxial tension of the 0 ° fiber orientation case at 80 ℃ is used to identify μ_f at 80 ℃ and it is nearly zero.

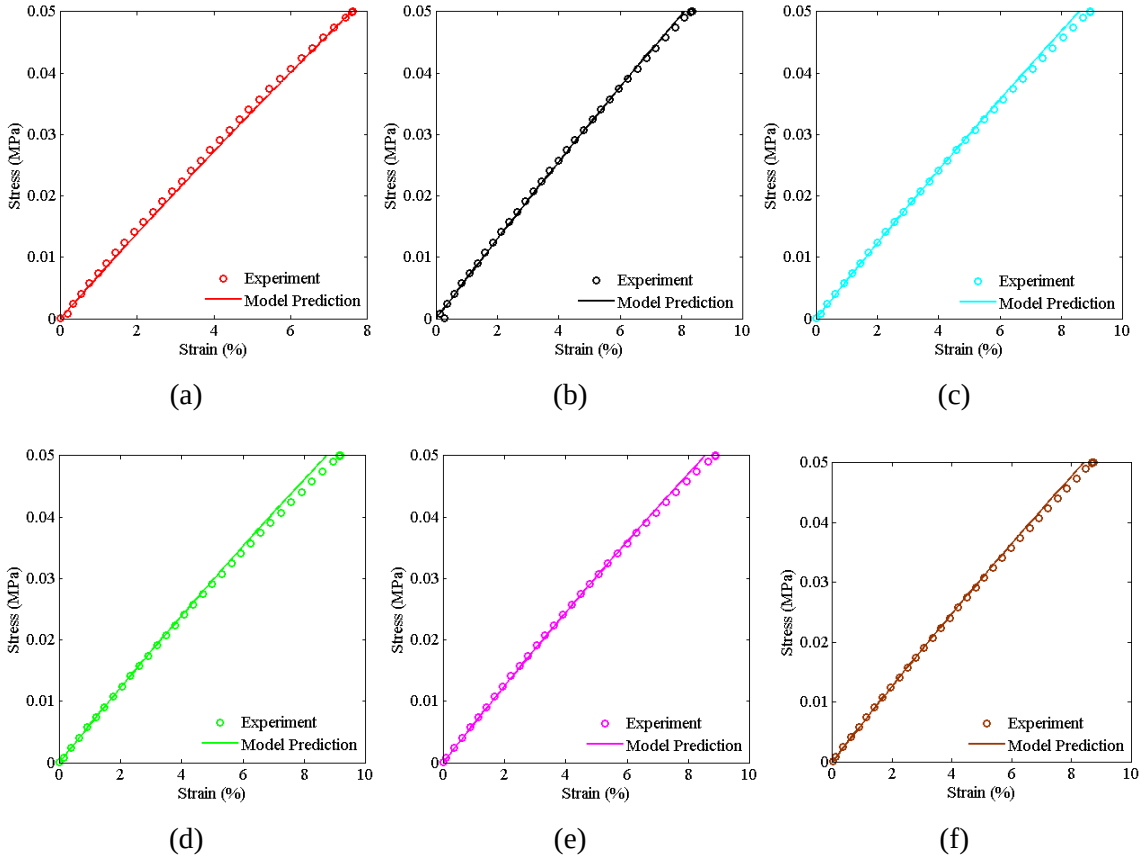

Fig. 41 The model with $\mu_f \approx 0$ predicts uniaxial tensions of other six fiber orientations at 30 ℃: (a) the 15 ° fiber orientation case. (b) The 30 ° fiber orientation case. (c) The 45 ° fiber orientation case. (d) The 60 ° fiber orientation case. (e) The 75 ° fiber orientation case. (f) The 90 ° fiber orientation case.

Figure 42 shows the prediction of Young's modulus of the composites with different fiber orientations from $0°$ to $90°$, at $30℃$ and at $80℃$, respectively. The predictions show good agreement with experimental results. Considering the case where fibers and the matrix are perfectly bonded with $\mu_f = 50\text{MPa}$ at $30℃$, the prediction shows if the fiber orientation is lower than $45°$, the stiffness of the composite is dramatically increased by changing μ_f from 9MPa to 50MPa. However, if the fiber orientation is higher than $45°$, the stiffness of the composite is less sensitive to μ_f.

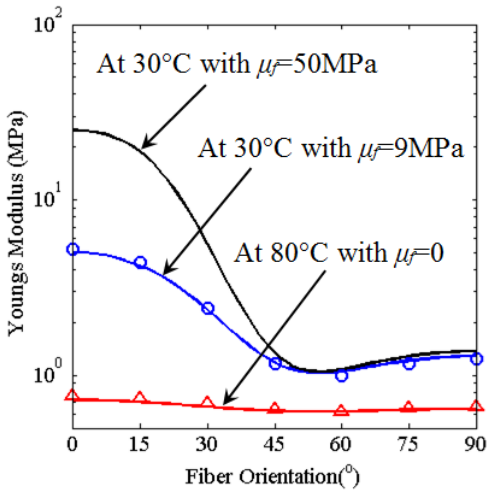

Fig. 42 The comparison of Young's modulus vs fiber orientation between experimental results and model predictions.

4.3.3 Models for thermal strain

During a heating-cooling cycle, the composite has thermal deformation gradient in following form:

$$\mathbf{F}^{\mathrm{T}} = \begin{bmatrix} F_x^{\mathrm{T}} & F_{xy}^{\mathrm{T}} & 0 \\ F_{yx}^{\mathrm{T}} & F_y^{\mathrm{T}} & 0 \\ 0 & 0 & F_z^{\mathrm{T}} \end{bmatrix}. \tag{69}$$

All of these components in thermal deformation gradient are temperature and time dependent. Thus, they are:

$$
\begin{aligned}
F_x^{\mathrm{T}}(T,t) &= 1+\varepsilon_x^T(T,t),\\
F_y^{\mathrm{T}}(T,t) &= 1+\varepsilon_y^T(T,t),\\
F_z^{\mathrm{T}}(T,t) &= 1+\varepsilon_z^T(T,t),\\
F_{xy}^{\mathrm{T}}(T,t) &= \gamma_{xy}^T(T,t)/2,\\
F_{yx}^{\mathrm{T}}(T,t) &= \gamma_{yx}^T(T,t)/2.
\end{aligned}
\tag{70}
$$

Fig. 43a shows a small element. Assuming there is no tractions acting on any of its six faces. Therefore, as temperature changing, the strain is free thermal strain. The free thermal strains are: $\varepsilon_1^T(T,t)$, $\varepsilon_2^T(T,t)$ and $\varepsilon_3^T(T,t)$. In a more general case shown in Fig. 43b, if the fibers are oriented θ degree counterclockwise from the x-axis, the thermal strains in the x-y-z global coordinate system can be transformed from the 1-2-3 fiber local coordinate system:

$$
\begin{aligned}
\varepsilon_x^{\mathrm{T}}(\theta,T,t) &= \cos^2\theta\varepsilon_1^{\mathrm{T}}(T,t)+\sin^2\theta\varepsilon_2^{\mathrm{T}}(T,t),\\
\varepsilon_y^{\mathrm{T}}(\theta,T,t) &= \cos^2\theta\varepsilon_2^{\mathrm{T}}(T,t)+\sin^2\theta\varepsilon_1^{\mathrm{T}}(T,t),\\
\varepsilon_z^{\mathrm{T}}(\theta,T,t) &= \varepsilon_3^{\mathrm{T}}(T,t),\ \gamma_{yz}^{\mathrm{T}}(T,t)=\gamma_{xz}^{\mathrm{T}}(T,t)=0,\\
\gamma_{xy}^{\mathrm{T}}(\theta,T,t) &= 2\left[\varepsilon_1^{\mathrm{T}}(T,t)-\varepsilon_2^{\mathrm{T}}(T,t)\right]\sin\theta\cos\theta.
\end{aligned}
\tag{71}
$$

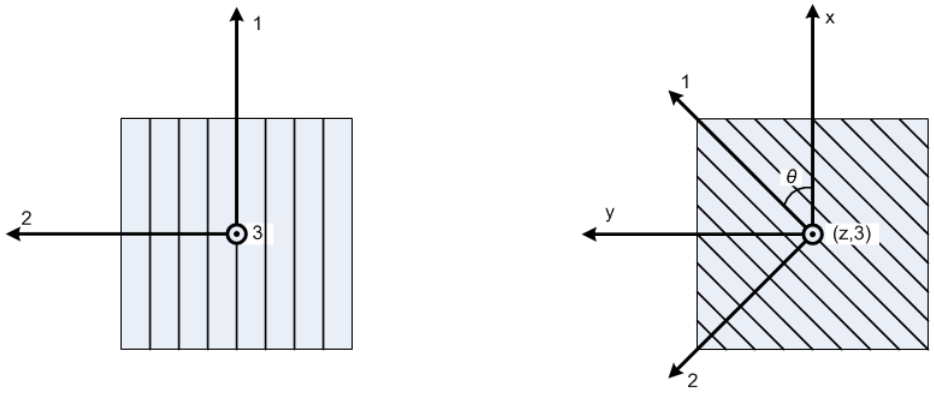

(a) (b)

Fig. 43 Schematics of a fiber reinforced composite: (a) a small element with three free thermal strains. (b) A more general case, where the fibers are orientated by θ degree counterclockwise from the x-axis, the thermal strains of the composite in the x-y-z global coordinate system can be transformed from the 1-2-3 fiber local coordinate system.

In the ASMEC case, $\varepsilon_1^T(T,t)$ is $\varepsilon_x^T(0°,T,t)$ for the $0°$ fiber orientation case and $\varepsilon_2^T(T,t)$ is $\varepsilon_x^T(90°,T,t)$ for the $90°$ fiber orientation case. As long as, we can describe $\varepsilon_x^T(0°,T,t)$ and $\varepsilon_x^T(90°,T,t)$, we can describe the thermal strain between them based on Eq. (71).

In Fig. 44a, during cooling from T_H to T_L (T_H =80 ℃, T_L =30 ℃) at a cooling rate Q ($Q = 2$℃/min), the thermal strains are:

$$\varepsilon_x^T(0°,T,t) = \varepsilon_1^{\mathrm{T}}(T,t) = \int_0^{\frac{T-T_H}{Q}} \alpha_1^m Q dt,\ \varepsilon_x^T(90°,T,t) = \varepsilon_2^{\mathrm{T}}(T,t) = \int_0^{\frac{T-T_H}{Q}} \alpha_2^m Q dt. \tag{72}$$

During isothermal crystallization at T_L, the thermal strains are:

$$\begin{aligned} \varepsilon_x^T(0°,T,t) &= \varepsilon_x^T\left(0°,T_L,\frac{T_L-T_H}{Q}\right) + \int_{\frac{T_L-T_H}{Q}}^{t} \varepsilon_1^{PT}\dot{v}_c(t)dt, \\ \varepsilon_x^T(90°,T,t) &= \varepsilon_x^T\left(90°,T_L,\frac{T_L-T_H}{Q}\right) + \int_{\frac{T_L-T_H}{Q}}^{t} \varepsilon_2^{PT}\dot{v}_c(t)dt, \end{aligned} \tag{73}$$

where $v_c(t)$ is the relative crystallinity changing from 0 to 1. During heating from T_L to T_H, the thermal strains are:

$$\begin{aligned} \varepsilon_x^T(0°,T,t) &= \varepsilon_x^{\mathrm{T}}\left(0°,T_L,\frac{T_L-T_H}{Q}+t_{iso}\right) + \int_0^{\frac{T-T_L}{Q}} \alpha_1^c v_c(t) + \alpha_1^m\left[1-v_c(t)\right] + \varepsilon_1^{PT}\dot{v}_c(t)dt, \\ \varepsilon_x^T(90°,T,t) &= \varepsilon_x^{\mathrm{T}}\left(90°,T_L,\frac{T_L-T_H}{Q}+t_{iso}\right) + \int_0^{\frac{T-T_L}{Q}} \alpha_2^c v_c(t) + \alpha_2^m\left[1-v_c(t)\right] + \varepsilon_2^{PT}\dot{v}_c(t)dt. \end{aligned} \tag{74}$$

In fig. 44b, parameters are identified by fitting the thermal strains at $0°$ and $90°$ (dash-dot line representing model fitting). They are $\alpha_1^m = 0.02\%/°\mathrm{C}$, $\alpha_1^c = 0.02\%/°\mathrm{C}$, $\varepsilon_1^{PT} = 1.05\%$, $\alpha_2^m = 0.02\%/°\mathrm{C}$, $\alpha_2^c = 0.02\%/°\mathrm{C}$, $\varepsilon_2^{PT} = 0.15\%$. Based on Eq. (71), $\varepsilon_x^{\mathrm{T}}(\theta,T,t)$ with the other five orientations are predicted in Fig. 44c.

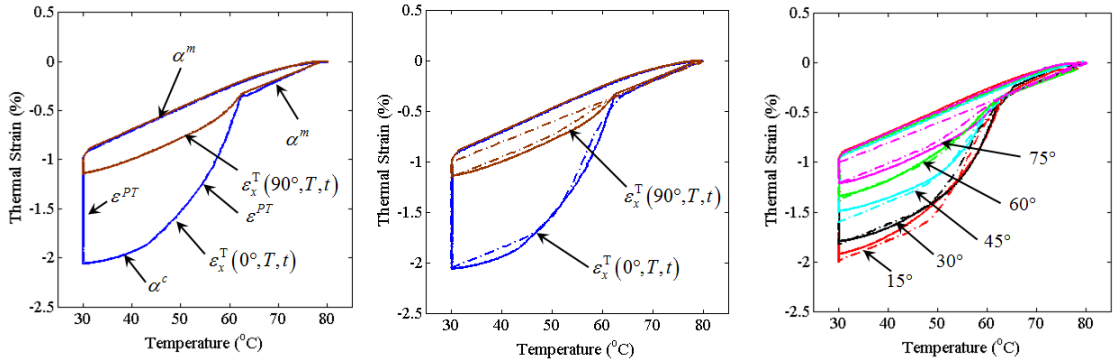

(a) (b) (c)

Fig. 44 Model fitting and prediction for free thermal strain: (a) free thermal strain vs temperature for the 0 ° and 90 ° fiber orientation cases. (b) Model fitting for free thermal strain vs temperature for the 0 ° and 90 ° fiber orientation cases. (c) Model prediction for free thermal strain vs temperature for the other five fiber orientation cases.

4.3.4 Thermomechanics during phase evolution

During a thermomechanical cycle, the total deformation gradient $\mathbf{F}^{total}$ can be decomposed into the thermal deformation gradient $\mathbf{F}^T$ and the mechanical deformation gradient $\mathbf{F}^M$, which gives rise to stress:

$$\mathbf{F}^{total} = \mathbf{F}^T\mathbf{F}^M . \tag{75}$$

During phase evolution, μ_f gradually increases from 0 to a certain value. Typically, in this composite system, μ_f gradually increases from 0 to $\bar{\mu}_c$. μ_a and μ_b in Eq. (68) are also gradually changing from $\mu_a(0)=\dfrac{(1-\nu_f)}{(1+\nu_f)}\mu_m$ to $\mu_a(\bar{\mu}_c)=\dfrac{(1-\nu_f)\mu_m+(1+\nu_f)\bar{\mu}_c}{(1+\nu_f)\mu_m+(1-\nu_f)\bar{\mu}_c}\mu_m$, and from $\mu_b(0)=\dfrac{\nu_m\nu_f}{(1+\nu_f)}\mu_m$ to $\mu_b(\bar{\mu}_c)=\dfrac{(\bar{\mu}_c-\mu_m)^2\nu_m\nu_f}{(1+\nu_f)\mu_m+(1-\nu_f)\bar{\mu}_c}$, respectively.

Before phase evolution, at time $t=0$, $\mu_f=0$, and the mechanical deformation gradient is $\mathbf{F}_0^M$. Therefore, the Cauchy stress is:

$$\boldsymbol{\sigma}_0 = -p\mathbf{I}+\mu_a(0)\mathbf{F}_0^{\mathrm{M}}\left(\mathbf{F}_0^{\mathrm{M}}\right)^{\mathrm{T}}+\mu_b(0)\left(1-I_4^{-3/2}\right)\mathbf{F}_0^{\mathrm{M}}\mathbf{a}_0\otimes\mathbf{F}_0^{\mathrm{M}}\mathbf{a}_0 . \tag{76}$$

During phase evolution, at time $t=\Delta t$, as a crystalline phase with $\Delta v_{c,1}$ forms, the effective shear modulus of the fiber in the composite becomes $\bar{\mu}_{c,1}=\Delta v_{c,1}\mu_c$. μ_a and μ_b in Eq. (68) become $\mu_a\left(\bar{\mu}_{c,1}\right)$ and $\mu_b\left(\bar{\mu}_{c,1}\right)$, and the increments of μ_a and μ_b are:

$$\Delta\mu_{a,1}=\mu_a\left(\bar{\mu}_{c,1}\right)-\mu_a\left(0\right) \text{ and } \Delta\mu_{b,1}=\mu_b\left(\bar{\mu}_{c,1}\right)-\mu_b\left(0\right). \tag{77}$$

As the newly formed crystalline phase forming at the configuration where deformation gradient is $\mathbf{F}_0^M$ and it is stress-free, the modulus increments $\Delta\mu_{a,1}$ and $\Delta\mu_{b,1}$ are not associate with the deformation gradient $\mathbf{F}_0^M$. Meanwhile, accompanying with the creation of the new phase, an incremental deformation gradient $\Delta\mathbf{F}_1^M$ may be applied to the material. Therefore, the Cauchy stress at time $t=\Delta t$ is:

$$\begin{aligned}\boldsymbol{\sigma}_1=&-p\mathbf{I}+\mu_{a,0}\mathbf{F}_1^{\mathrm{M}}\left(\mathbf{F}_1^{\mathrm{M}}\right)^{\mathrm{T}}+\mu_{b,0}\left[1-I_4\left(\mathbf{F}_1^{\mathrm{M}},\mathbf{a}_0\right)^{-3/2}\right]\mathbf{F}_1^{\mathrm{M}}\mathbf{a}_0\otimes\mathbf{F}_1^{\mathrm{M}}\mathbf{a}_0\\&+\Delta\mu_{a,1}\mathbf{F}_{1\to1}^{\mathrm{M}}\left(\mathbf{F}_{1\to1}^{\mathrm{M}}\right)^{\mathrm{T}}+\Delta\mu_{b,1}\left[1-I_4\left(\mathbf{F}_{1\to1}^{\mathrm{M}},\mathbf{a}_1\right)^{-3/2}\right]\mathbf{F}_{1\to1}^{\mathrm{M}}\mathbf{a}_1\otimes\mathbf{F}_{1\to1}^{\mathrm{M}}\mathbf{a}_1,\end{aligned} \tag{78}$$

where $\mu_{a,0}=\mu_a\left(0\right)$, $\mu_{b,0}=\mu_b\left(0\right)$, $\mathbf{F}_1^{\mathrm{M}}=\Delta\mathbf{F}_1^{\mathrm{M}}\mathbf{F}_0^{\mathrm{M}}$, $\mathbf{F}_{1\to1}^{\mathrm{M}}=\Delta\mathbf{F}_1^{\mathrm{M}}$, $\mathbf{a}_1=\dfrac{\mathbf{F}_1^{\mathrm{M}}\mathbf{a}_0}{\left|\mathbf{F}_1^{\mathrm{M}}\mathbf{a}_0\right|}$ and $I_4\left(\mathbf{F},\mathbf{a}\right)=\mathbf{F}\mathbf{a}\cdot\mathbf{F}\mathbf{a}$. Extending the algorithm into the case at time $t=n\Delta t$, the Cauchy stress is:

$$\begin{aligned}\boldsymbol{\sigma}_n=&-p\mathbf{I}+\mu_{a,0}\mathbf{F}_n^{\mathrm{M}}\left(\mathbf{F}_n^{\mathrm{M}}\right)^{\mathrm{T}}+\mu_{b,0}\left[1-I_4\left(\mathbf{F}_n^{\mathrm{M}},\mathbf{a}_0\right)^{-3/2}\right]\mathbf{F}_n^{\mathrm{M}}\mathbf{a}_0\otimes\mathbf{F}_n^{\mathrm{M}}\mathbf{a}_0\\&+\sum_{i=1}^{n}\left\{\Delta\mu_{a,i}\mathbf{F}_{i\to n}^{\mathrm{M}}\left(\mathbf{F}_{i\to n}^{\mathrm{M}}\right)^{\mathrm{T}}+\Delta\mu_{b,i}\left[1-I_4\left(\mathbf{F}_{i\to n}^{\mathrm{M}},\mathbf{a}_i\right)^{-3/2}\right]\mathbf{F}_{i\to n}^{\mathrm{M}}\mathbf{a}_i\otimes\mathbf{F}_{i\to n}^{\mathrm{M}}\mathbf{a}_i\right\},\end{aligned} \tag{79}$$

where $\Delta\mu_{a,i}=\mu_a\left(v_{c,i}\bar{\mu}_c\right)-\mu_a\left(v_{c,i-1}\bar{\mu}_c\right)$, $\Delta\mu_{b,i}=\mu_b\left(v_{c,i}\bar{\mu}_c\right)-\mu_b\left(v_{c,i-1}\bar{\mu}_c\right)$, $\mathbf{F}_n^{\mathrm{M}}=\left(\prod_{i=1}^{n}\Delta\mathbf{F}_i^{\mathrm{M}}\right)\mathbf{F}_0^{\mathrm{M}}$, $\mathbf{F}_{i\to n}^{\mathrm{M}}=\left(\prod_{j=i}^{n}\Delta\mathbf{F}_i^{\mathrm{M}}\right)$, $\mathbf{a}_i=\dfrac{\mathbf{F}_{i-1}^{\mathrm{M}}\mathbf{a}_0}{\left|\mathbf{F}_{i-1}^{\mathrm{M}}\mathbf{a}_0\right|}$, $I_4\left(\mathbf{F},\mathbf{a}\right)=\mathbf{F}\mathbf{a}\cdot\mathbf{F}\mathbf{a}$ and $v_{c,i}=\sum_{j=1}^{i}\Delta v_{c,j}$.

4.3.5 Phase evolution rule

The modified Avrami's theory (M. Avrami, 1941, 1939, 1940, Ozawa, 1971) was use to describe the crystallinity during the isothermal crystallization. At time $t = i\Delta t$:

$$v_{c,i} = 1 - \exp\left[-k \cdot (t)^n\right], \tag{80}$$

where k is a constant related the growth rate of crystallization and n is a constant related to the dimension of the crystals.

4.4 Results

4.4.1 Shape memory behaviors

With 12 parameters listed in table 6, the model was able to predict the shape memory behaviors for the seven fiber orientation cases and for the case of the neat rubbery matrix material. Fig. 45 shows the comparison between experiments and model predictions. The model prediction shows good agreement with experiments. The major error occurs at three steps: at S2 and S3, the error might be due to the thermal expansion; at S4 (unloading), prediction shows better fixity than experiment, due to the plastic deformation that the model cannot characterize.

Table 6. List of material parameters

Parameter	Value	Description
Composition		
v_m	0.833	Volume fraction of Matrix
v_f	0.167	Volume fraction of Fiber
Mechanical behavior		
N	$0.822 kPa / K$	Polymer crosslinking density
$\bar{\mu}_c$	9MPa	The effective modulus of fibers in the composite
Thermal strains		
α_1^m	2×10^{-4}°C^{-1}	CTE at high temperature for the 0 ℃ case
α_2^m	2×10^{-4}°C^{-1}	CTE at high temperature for the 90 ℃ case

α_1^c	2×10^{-4}°C^{-1}	CTE at low temperature for the 0 ℃ case
α_2^c	2×10^{-4}°C^{-1}	CTE at low temperature for the 90 ℃ case
ε_1^{PT}	1.05×10^{-2}	Thermal strain due to crystallization for the 0 ℃ case
ε_2^{PT}	0.15×10^{-2}	Thermal strain due to crystallization for the 90 ℃ case
Kinetics of crystallization		
k	1×10^{-8} min^{-1}	Growth rate of the crystalline phases
n	3	Dimension of the crystalline phases

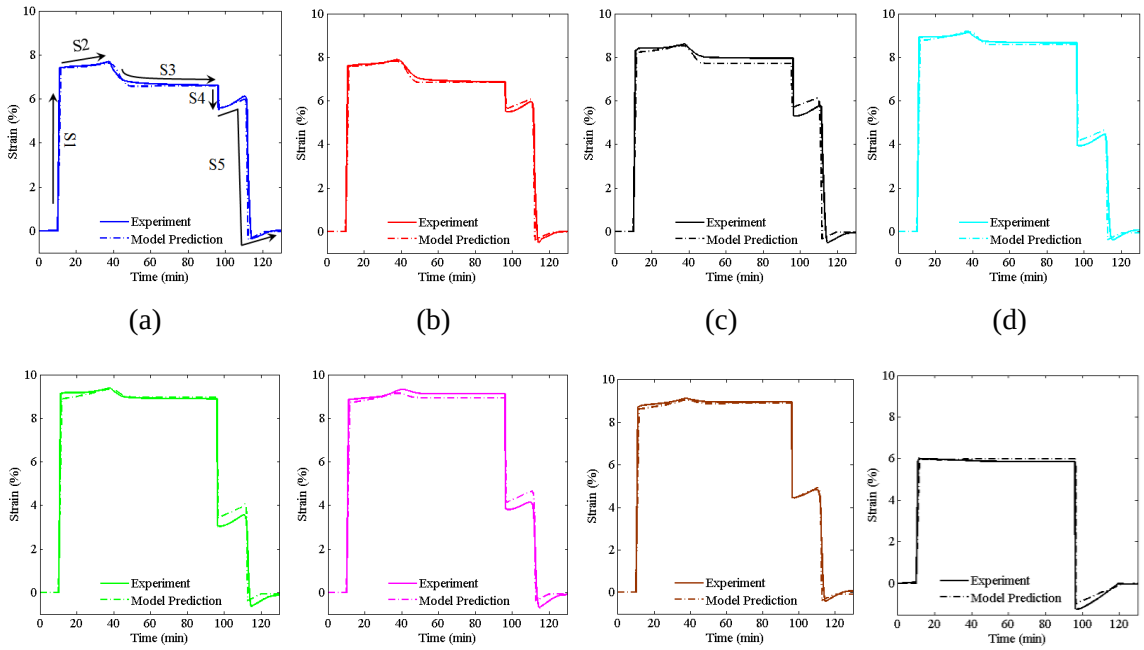

Fig. 45 Model predictions for shape memory behaviors: (a) the 0 ° fiber orientation case. (b) the 15 ° fiber orientation case. (c) The 30 ° fiber orientation case. (d) The 45 ° fiber orientation case. (e) The 60 ° fiber orientation case. (f) The 75 ° fiber orientation case. (g) The 90 ° fiber orientation case. (h) The rubbery matrix material.

4.4.2 Parametric study

Fixity can be improved by increasing volume fraction of fibers (v_f). In Fig. 46a, the fixity is enhanced by increasing v_f. It is also found that as $v_f = 0$, where it is actually the neat

rubbery matrix material, the "fixity" turns into negative, which is consistent with the experimental observation.

The effective shear modulus of fibers might be changed by changing the interface between the matrix and fibers or choosing different material with different stiffness as fiber. The changing of the effective shear modulus of fibers affects the fixity of the composite. Fig. 46b shows the fixity at arbitrary fiber orientation with different effective shear modulus ($\bar{\mu}_c$). As fiber orientation $\theta < 45°$, apparently, when $\bar{\mu}_c$ is increased, the fixity is improved. As fiber orientation $\theta > 45°$, the effect is still observed, but it is limited as $\bar{\mu}_c > 20\text{MPa}$.

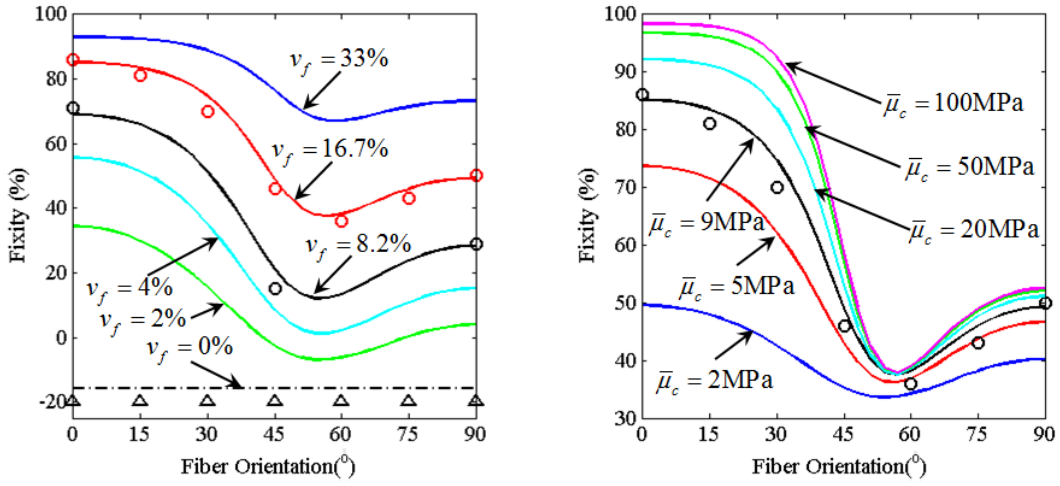

(a) (b)

Fig. 46 Parametric studies: (a) effect of volume fractions of fibers. (b) Effect of effective shear modulus of fiber crystals.

4.4.3 Effect of thermal strain

The model was used to investigate the effect of the thermal strain on memory behaviors. Fig. 47 shows the comparison of a shape memory cycle between experiment and model predictions with/without thermal strain for 0 ° fiber orientation case. For the case without thermal strain, during S2 (cooling), the strain goes up further than the one with thermal strain. During S2, as the matrix in the rubbery state and fiber melted, the modulus of the composite is decreased by

decreasing temperature due to entropic elasticity. In order to balance the constant load applied, the material deforms more at lower modulus. However, during cooling, thermal strain always decreases. This is the reason that the slope of the strain without thermal strain is larger than the one with thermal strain. At S3 (isothermal crystallization), for the case without thermal strain, the strain drop due the crystallization disappears. Based on Eq. (1), the fixity with thermal strain is $R_f = \frac{\varepsilon_u}{\varepsilon_m} \times 100\%$ and the one without thermal strain is $R_f' = \frac{\varepsilon_u'}{\varepsilon_m'} \times 100\%$. From Fig. 47, obviously, $\varepsilon_u = \varepsilon_u' + \varepsilon_T$ and $\varepsilon_m = \varepsilon_m' + \varepsilon_T$, where ε_T is the thermal strain at 30 ℃ and $\varepsilon_T < 0$. Therefore, we always have $\varepsilon_m - \varepsilon_u = \varepsilon_m' - \varepsilon_u'$ indicating that during unloading, only mechanical strain changes. We also always have that $R_f' > R_f$.

Fig. 47b also shows the same comparison for the rubbery matrix material. For the case without thermal strain, at S4 (unloading), the strain immediately drops to zero and the fixity for this case ($R_f' = \frac{\varepsilon_u'}{\varepsilon_m'} \times 100\%$) turns to zero. This is reasonable for the material doesn't have shape memory effect, whose fixity must be zero. For the case with thermal strain, after unloading turns ε_u to be negative, since it includes the thermal contraction. The negative ε_u makes the fixity $R_f = \frac{\varepsilon_u}{\varepsilon_m} \times 100\%$ to be negative.

ε_T

In Fig. 47c, the model predicts the fixity without the thermal strain for all cases. It shows that the fixity without thermal strain is always higher than the one with thermal strain. For the neat rubbery matrix case, once the thermal strain is not considered, the fixity turns to be zero.

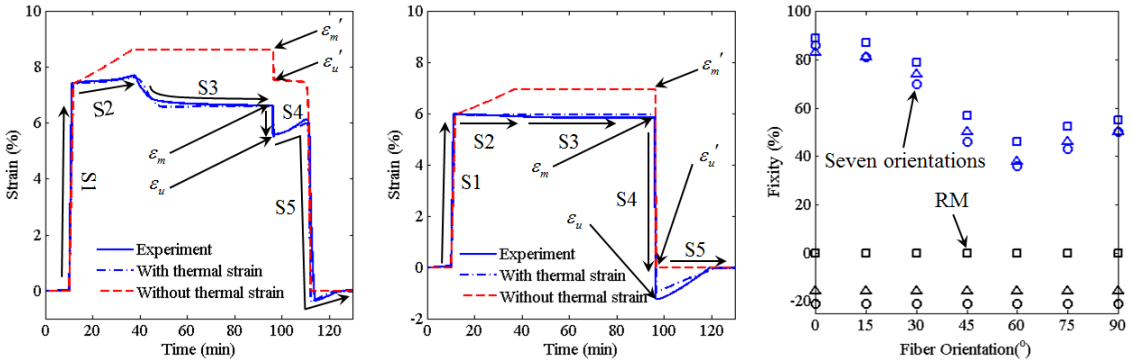

(a) (b) (c)

Fig. 47 Effect of thermal strain: (a) comparison of the 0 ° fiber orientation case with thermal strain and without thermal strain. (b) Comparison of the rubbery matrix material with thermal strain and without thermal strain. (c) Comparison of fixity with thermal strain and without thermal strain.

4.5 Conclusion

In this chapter, the fabrication of ASMECs by 3D printer is introduced. Experiments including DMA tests, uniaxial tensions, thermal strain tests and shape memory behavior tests show the ASMECs exhibit isotropic behaviors. A 3D anisotropic thermomechanical constitutive is developed to capture the anisotropic shape memory behaviors of the ASMEC. The parametric studies such as the effect of volume fractions and the effect of the effective shear modulus of fibers are investigated using the model.

BIBLIOGRAPHY

Alvarez, F., Alegria, A. and Colmenero, J.: Relationship between the Time-Domain Kohlrausch-Williams-Watts and Frequency-Domain Havriliak-Negami Relaxation Functions. Physical Review B 44(14), 7306-7312 (1991)

Angell, C.A., Ngai, K.L., McKenna, G.B., McMillan, P.F. and Martin, S.W.: Relaxation in glassforming liquids and amorphous solids. Journal of Applied Physics 88(6), 3113-3157 (2000)

Angelloz, C., Fulchiron, R., Douillard, A., Chabert, B., Fillit, R., Vautrin, A. and David, L.: Crystallization of isotactic polypropylene under high pressure (gamma phase). Macromolecules 33(11), 4138-4145 (2000)

Avrami, M.: Granulation, Phase Change, and Microstructure - Kinetics of Phase Change. III. Journal of Chemical Physics 9(2), 177-184 (1941)

Avrami, M.: Kinetics of phase change I - General theory. Journal of Chemical Physics 7(12), 1103-1112 (1939)

Avrami, M.: Kinetics of phase change II - Transformation-Time Relations for Random Distribution of Nuclei. Journal of Chemical Physics 8(212-224 (1940)

Barot, G. and Rao, I.J.: Constitutive modeling of the mechanics associated with crystallizable shape memory polymers. Zeitschrift Fur Angewandte Mathematik Und Physik 57(4), 652-681 (2006)

Barot, G., Rao, I.J. and Rajagopal, K.R.: A thermodynamic framework for the modeling of crystallizable shape memory polymers. International Journal of Engineering Science 46(4), 325-351 (2008)

Bellin, I., Kelch, S., Langer, R. and Lendlein, A.: Polymeric triple-shape materials. Proceedings of the National Academy of Sciences of the United States of America 103(48), 18043-18047 (2006)

Bellin, I., Kelch, S. and Lendlein, A.: Dual-shape properties of triple-shape polymer networks with crystallizable network segments and grafted side chains. Journal of Materials Chemistry 17(28), 2885-2891 (2007)

Caruthers, J.M., Adolf, D.B., Chambers, R.S. and Shrikhande, P.: A thermodynamically consistent, nonlinear viscoelastic approach for modeling glassy polymers. Polymer 45(13), 4577-4597 (2004)

Castro, F., Westbrook, K.K., Long, K.N., Shandas, R. and Qi, H.J.: Effects of thermal rates on the thermomechanical behaviors of amorphous shape memory polymers. Mechanics of Time-Dependent Materials 14(3), 219-241 (2010)

Chen, S., Hu, J. and Zhuo, H.: Properties and mechanism of two-way shape memory polyurethane composites. Composites Science and Technology 70(10), 1437-1443 (2010)

Chen, S., Hu, J., Zhuo, H. and Zhu, Y.: Two-way shape memory effect in polymer laminates. Materials Letters 62(25), 4088-4090 (2008)

Chen, Y.C. and Lagoudas, D.C.: A constitutive theory for shape memory polymers. Part I-Large deformations. Journal of the Mechanics and Physics of Solids 56(5), 1752-1765 (2008a)

Chen, Y.C. and Lagoudas, D.C.: A constitutive theory for shape memory polymers. Part II-A linearized model for small deformations. Journal of the Mechanics and Physics of Solids 56(5), 1766-1778 (2008b)

Chung, T., Rorno-Uribe, A. and Mather, P.T.: Two-way reversible shape memory in a semicrystalline network. Macromolecules 41(1), 184-192 (2008)

Clarson, S.J., Dodgson, K. and Semlyen, J.A.: Studies of Cyclic and Linear Poly(Dimethylsiloxanes) .19. Glass-Transition Temperatures and Crystallization Behavior. Polymer 26(6), 930-934 (1985)

Di Marzio, E.A. and Yang, A.J.M.: Configurational entropy approach to the kinetics of glasses. Journal of Research of the National Institute of Standards and Technology 102(2), 135-157 (1997)

Dunn, M.L.: One-dimensioal composite micromechanics. International Journal of Mechanical Engineering Education 26(38-50 (1998)
Evans, U.R.: The Laws of Expanding Circles and Spheres in Relation to the Lateral Growth of Surface Films and the Grain-Size of Metals. Transactions of the Faraday Society 41(7), 365-374 (1945)
Ge, Q., Luo, X.F., Rodriguez, E.D., Zhang, X., Mather, P.T., Dunn, M.L. and Qi, H.J.: Thermomechanical behavior of shape memory elastomeric composites. Journal of the Mechanics and Physics of Solids 60(1), 67-83 (2012)
Ge, Q., Yu, K., Ding, Y.F. and Qi, H.J.: Prediction of temperature-dependent free recovery behaviors of amorphous shape memory polymers. Soft Matter 8(11098-11105 (2012)
Guo, Z.Y., Peng, X.Q. and Moran, B.: A composites-based hyperelastic constitutive model for soft tissue with application to the human annulus fibrosus. Journal of the Mechanics and Physics of Solids 54(9), 1952-1971 (2006)
Guo, Z.Y., Peng, X.Q. and Moran, B.: Mechanical response of neo-Hookean fiber reinforced incompressible nonlinearly elastic solids. International Journal of Solids and Structures 44(6), 1949-1969 (2007)
H. Jerry Qi, Thao D. Nguyen, Francisco Castro, Christopher M. Yakacki and Robin Shandas: Finite deformation thermo-mechanical behavior of thermally induced shape memory polymers. Journal of the Mechanics & Physics of Solids 56(5), 1730-51 (2008)
Hoyle, C.E. and Bowman, C.N.: Thiol-Ene Click Chemistry. Angewandte Chemie-International Edition 49(9), 1540-1573 (2010)
Huang, W.M., Yang, B., An, L., Li, C. and Chan, Y.S.: Water-driven programmable polyurethane shape memory polymer: Demonstration and mechanism. Applied Physics Letters 86(11), 114105 (2005)
Ingrid A. Rousseau and Patrick T. Mather: Shape Memory Effect Exhibited by Smectic-C Liquid Crystalline Elastomers. Journal of the American Chemical Society 125(50), 15300-15301 (2003)
Isayev, A.I. and Catignani, B.F.: Crystallization and microstructure in quenched slabs of various molecular weight polypropylenes. Polymer Engineering and Science 37(9), 1526-1539 (1997)
Jiang, H.Y., Kelch, S. and Lendlein, A.: Polymers move in response to light. Advanced Materials 18(11), 1471-1475 (2006)
Koerner, H., Price, G., Pearce, N.A., Alexander, M. and Vaia, R.A.: Remotely actuated polymer nanocomposites - stress-recovery of carbon-nanotube-filled thermoplastic elastomers. Nature Materials 3(2), 115-120 (2004)
Kweon, H., Yoo, M.K., Park, I.K., Kim, T.H., Lee, H.C., Lee, H.S., Oh, J.S., Akaike, T. and Cho, C.S.: A novel degradable polycaprolactone networks for tissue engineering. Biomaterials 24(5), 801-808 (2003)
Lauritzen, J.I. and Hoffman, J.D.: Extension of Theory of Growth of Chain-Folded Polymer Crystals to Large Undercoolings. Journal of Applied Physics 44(10), 4340-4352 (1973)
Lendlein, A., Jiang, H.Y., Junger, O. and Langer, R.: Light-induced shape-memory polymers. Nature 434(7035), 879-882 (2005)
Lendlein, A. and Kelch, S.: Shape-memory polymers. Angew Chem Int Ed Engl 41(12), 2035-57 (2002)
Lendlein, A. and Kelch, S.: Shape-memory polymers as stimuli-sensitive implant materials. Clinical Hemorheology & Microcirculation 32(2), 105-116 (2005)
Lendlein, A. and Langer, R.: Biodegradable, elastic shape-memory polymers for potential biomedical applications. Science 296(5573), 1673-1676 (2002)
Li, M.H., Keller, P., Li, B., Wang, X.G. and Brunet, M.: Light-driven side-on nematic elastomer actuators. Advanced Materials 15(7-8), 569-572 (2003)
Lindsey, C.P. and Patterson, G.D.: Detailed Comparison of the Williams-Watts and Cole-Davidson Functions. Journal of Chemical Physics 73(7), 3348-3357 (1980)

Liu, C., Qin, H. and Mather, P.T.: Review of progress in shape-memory polymers. Journal of Materials Chemistry 17(16), 1543-1558 (2007)
Liu, H.X., Huang, Y.Y., Yuan, L., He, P.S., Cai, Z.H., Shen, Y.L., Xu, Y.M., Yu, Y. and Xiong, H.G.: Isothermal crystallization kinetics of modified bamboo cellulose/PCL composites. Carbohydrate Polymers 79(3), 513-519 (2010)
Liu, Y.P., Gall, K., Dunn, M.L., Greenberg, A.R. and Diani, J.: Thermomechanics of shape memory polymers: Uniaxial experiments and constitutive modeling. International Journal of Plasticity 22(2), 279-313 (2006)
Liu, Y.P., Gall, K., Dunn, M.L. and McCluskey, P.: Thermomechanics of shape memory polymer nanocomposites. Mechanics of Materials 36(10), 929-940 (2004)
Long, K.N., Dunn, M.L. and Qi, H.J.: Mechanics of soft active materials with phase evolution. International Journal of Plasticity 26(4), 603-616 (2010)
Long, K.N., Scott, T.F., Qi, H.J., Bowman, C.N. and Dunn, M.L.: Photomechanics of light-activated polymers. Journal of the Mechanics and Physics of Solids 57(7), 1103-1121 (2009)
Luo, X.F. and Mather, P.T.: Preparation and Characterization of Shape Memory Elastomeric Composites. Macromolecules 42(19), 7251-7253 (2009)
Luo, X.F. and Mather, P.T.: Triple-Shape Polymeric Composites (TSPCs). Advanced Functional Materials 20(16), 2649-2656 (2010)
M. Avrami: Granulation, Phase Change, and Microstructure - Kinetics of Phase Change. III. Journal of Chemical Physics 9(2), 177-184 (1941)
M. Avrami: Kinetics of phase change I - General theory. Journal of Chemical Physics 7(12), 1103-1112 (1939)
M. Avrami: Kinetics of phase change II - Transformation-Time Relations for Random Distribution of Nuclei. Journal of Chemical Physics 8(212-224 (1940)
Ma, R. and Negahban, M.: Simulation of Mechanical Response in Crystallizing Polymers - Crystallization under a Constant Shear Force. Acta Mechanica 112(1-4), 59-76 (1995a)
Ma, R.J. and Negahban, M.: Simulation of Mechanical Response during Polymer Crystallization around Rigid Inclusions and Voids - Homogeneous Crystallization. Mechanics of Materials 21(1), 25-50 (1995b)
Mohr, R., Kratz, K., Weigel, T., Lucka-Gabor, M., Moneke, M. and Lendlein, A.: Initiation of shape-memory effect by inductive heating of magnetic nanoparticles in thermoplastic polymers. Proc Natl Acad Sci U S A 103(10), 3540-5 (2006)
Negahban, M.: Simulation of Mechanical Response in Crystallizing Polymers - Crystallization under Constant Shearing Deformations. Mechanics of Materials 16(4), 379-399 (1993)
Negahban, M. and Wineman, A.S.: Modeling the Mechanical Response of a Material Undergoing Continuous Isothermal Crystallization. International Journal of Engineering Science 30(7), 953-962 (1992)
Negahban, M., Wineman, A.S. and Ma, R.J.: Simulation of Mechanical Response in Polymer Crystallization. International Journal of Engineering Science 31(1), 93-113 (1993)
Nguyen, T.D., Qi, H.J., Castro, F. and Long, K.N.: A thermoviscoelastic model for amorphous shape memory polymers: Incorporating structural and stress relaxation. Journal of the Mechanics and Physics of Solids 56(9), 2792-2814 (2008)
O'Connell, P.A. and McKenna, G.B.: Arrhenius-type temperature dependence of the segmental relaxation below T-g. Journal of Chemical Physics 110(22), 11054-11060 (1999)
Ortega, A.M., Kasprzak, S.E., Yakacki, C.M., Diani, J., Greenberg, A.R. and Gall, K.: Structure-property relationships in photopolymerizable polymer networks: Effect of composition on the crosslinked structure and resulting thermomechanical properties of a (meth)acrylate-based system. Journal of Applied Polymer Science 110(3), 1559-1572 (2008)
Ozawa, T.: Kinetics of Non-Isothermal Crystallization. Polymer 12(3), 150-& (1971)
Phillips, J.C.: Stretched exponential relaxation in molecular and electronic glasses. Reports on Progress in Physics 59(9), 1133-1207 (1996)

Qi, H.J., Nguyen, T.D., Castro, F., Yakacki, C.M. and Shandas, R.: Finite deformation thermo-mechanical behavior of thermally induced shape memory polymers. Journal of the Mechanics & Physics of Solids 56(5), 1730-51 (2008a)
Qi, H.J., Nguyen, T.D., Castro, F., Yakacki, C.M. and Shandas, R.: Finite deformation thermo-mechanical behavior of thermally induced shape memory polymers. Journal of the Mechanics and Physics of Solids 56(5), 1730-51 (2008b)
Rajagopal, K.R. and Srinivasa, A.R.: Mechanics of the inelastic behavior of materials - Part 1, theoretical underpinnings. International Journal of Plasticity 14(10-11), 945-967 (1998a)
Rajagopal, K.R. and Srinivasa, A.R.: Mechanics of the inelastic behavior of materials. Part II: Inelastic response. International Journal of Plasticity 14(10-11), 969-995 (1998b)
Rickert, D., Lendlein, A., Kelch, S., Fuhrmann, R. and Franke, R.P.: Detailed Evaluation of the Agarose Diffusion Test as a Standard Biocompatibility Procedure Using an Image Analysis System. Influence of plasma sterilization on the biocompatibility of a recently developed photoset-polymer. Biomedizinische Technik 47(11), 285-289 (2002)
Rousseau, I.A.: Challenges of Shape Memory Polymers: A Review of the Progress Toward Overcoming SMP's Limitations. Polymer Engineering and Science 48(11), 2075-2089 (2008)
Ryu, J., D'Amato, M., Cui, X.D., Long, K.N., Qi, H.J. and Dunn, M.L.: Photo-Origami – Bending and Folding Polymers With Light. Applied Physics Letters In Press (2012)
Scott, T.F., Draughon, R.B. and Bowman, C.N.: Actuation in crosslinked polymers via photoinduced stress relaxation. Advanced Materials 18(16), 2128-2132 (2006)
Scott, T.F., Schneider, A.D., Cook, W.D. and Bowman, C.N.: Photoinduced plasticity in cross-linked polymers. Science 308(5728), 1615-1617 (2005)
Srivastava, V., Chester, S.A. and Anand, L.: Thermally actuated shape-memory polymers: Experiments, theory, and numerical simulations. Journal of the Mechanics and Physics of Solids 58(8), 1100-1124 (2010)
Svanberg, C.: Correlation function for relaxations in disordered materials. Journal of Applied Physics 94(6), 4191-4197 (2003)
Tamagawa, H.: Thermo-responsive two-way shape changeable polymeric laminate. Materials Letters 64(6), 749-751 (2010)
Thomas, S.M. and Lendlein, A.: Solving a knotty problem - surgical sutures from shape memory polymers. Materials World 10(7), 29-32 (2002)
Tobushi, H., Hara, H., Yamada, E. and Hayashi, S.: Thermomechanical properties in a thin film of shape memory polymer of polyurethane series. Smart Materials & Structures 5(4), 483-491 (1996)
Tobushi, H., Hayashi, S., Ikai, A. and Hara, H.: Thermomechanical properties of shape memory polymers of polyurethane series and their applications. Journal De Physique Iv 6(C1), 377-384 (1996)
Weiss, R.A., Izzo, E. and Mandelbaum, S.: New Design of Shape Memory Polymers: Mixtures of an Elastomeric Ionomer and Low Molar Mass Fatty Acids and Their Salts. Macromolecules 41(9), 2978-2980 (2008)
Westbrook, K.K., Castro, F., Long, K.N., Slifka, A.J. and Qi, H.J.: Improved testing system for thermomechanical experiments on polymers using uniaxial compression equipment. Polymer Testing 29(4), 503-512 (2010)
Westbrook, K.K., Mather, P.T., Parakh, V., Dunn, M.L., Ge, Q., Lee, B.M. and Qi, H.J.: Two-way reversible shape memory effects in a free-standing polymer composite. Smart Materials & Structures 20(6), (2011)
Westbrook, K.K., Parakh, V., Chung, T., Mather, P.T., Wan, L.C., Dunn, M.L. and Qi, H.J.: Constitutive Modeling of Shape Memory Effects in Semicrystalline Polymers With Stretch Induced Crystallization. Journal of Engineering Materials and Technology-Transactions of the Asme 132(4), 041010.1-9 (2010)

Williams, G. and Watts, D.C.: Non-Symmetrical Dielectric Relaxation Behaviour Arising from a Simple Empirical Decay Function. Transactions of the Faraday Society 66(565P), 80-85 (1970)
Williams, M.L., Landel, R.F. and Ferry, J.D.: Temperature Dependence of Relaxation Mechanisms in Amorphous Polymers and Other Glass-Forming Liquids. Physical Review 98(5), 1549-1549 (1955)
Wineman, A.: Changes due to scission in an elastomeric cylinder undergoing circular shear and heat conduction. American Society of Mechanical Engineers, Applied Mechanics Division, AMD 236,(15 (1999)
Wineman, A.: Some comments on the mechanical response of elastomers undergoing scission and healing at elevated temperatures. Mathematics and Mechanics of Solids 10(6), 673-689 (2005)
Wineman, A. and Min, J.H.: Scission and cross-linking in an elastomeric cylinder undergoing circular shear and heat conduction. American Society of Mechanical Engineers, Applied Mechanics Division, AMD 244,(117 (2000)
Wineman, A. and Min, J.H.: Time dependent scission and cross-linking in an elastomeric cylinder undergoing circular shear and heat conduction. International Journal of Non-Linear Mechanics 38(7), 969-983 (2003)
Wineman, A. and Shaw, J.: Influence of thermally induced scission and crosslinking on the post-scission inflation of circular elastomeric membranes. International Journal of Engineering Science 46(8), 758-774 (2008)
Xie, T.: Tunable polymer multi-shape memory effect. Nature 464(7286), 267-270 (2010)
Xie, T., Xiao, X.C. and Cheng, Y.T.: Revealing Triple-Shape Memory Effect by Polymer Bilayers. Macromolecular Rapid Communications 30(21), 1823-1827 (2009)
Yakacki, C.M., Shandas, R., Lanning, C., Rech, B., Eckstein, A. and Gall, K.: Unconstrained recovery characterization of shape-memory polymer networks for cardiovascular applications. Biomaterials 28(14), 2255-2263 (2007)

APPENDIX A

PREDICTION OF TEMPERATURE-DEPENDENT FREE RECOVERY BEHAVIORS OF AMORPHOUS SHAPE MEMORY POLYMERS

1. Introduction

Shape memory polymers (SMPs) are active materials that can recover a pre-deformed shape in response to an environmental stimulus such as temperature (Di Marzio and Yang, 1997, Lendlein and Kelch, 2002, 2005, Liu, et al., 2007, Luo and Mather, 2009, Xie, 2010), light (Jiang, et al., 2006, Koerner, et al., 2004, Lendlein, et al., 2005, Li, et al., 2003, Long, et al., 2009, Ryu, et al., 2012, Scott, et al., 2006, Scott, et al., 2005, Westbrook,Castro, et al., 2010), moisture (Huang, et al., 2005), and magnetic field (Mohr, et al., 2006). The most attractive feature of SMPs is their capability of undergoing very large deformation. For example, deformation excess of 1100% was reported (Lendlein and Kelch, 2002). This advantage allows SMPs to be used in many applications such as actuation components in microsystem, biomedical devices, active surface patterning, aerospace deployable structure, and morphing structures (Lendlein and Kelch, 2002, 2005, Liu, et al., 2006, Liu, et al., 2004, Tobushi,Hara, et al., 1996, Williams, et al., 1955, Yakacki, et al., 2007). Among the SMPs developed recently, thermally triggered SMPs are the primary focus in the SMP research (Yakacki, et al., 2007).

For thermally triggered SMPs, they undergo a typical four-step thermomechanical shape memory (SM) cycle to achieve the SM behavior (Castro, et al., 2010, Di Marzio and Yang, 1997, Lendlein and Kelch, 2002, Liu, et al., 2006, Qi, et al., 2008a). At Step 1, the polymer is heated to a temperature above its phase transition temperature T_{trans} (the phase transition temperature can be either glass transition temperature T_g for amorphous SMPs or melting temperature T_m for semicrystalline SMPs. Specifically, in this paper, the simplified model is developed for amorphous SMPs, which include covalently cross-linked glassy thermoset networks and

physically cross-linked glassy copolymers(Liu, et al., 2007), and $T_{trans} = T_g$), then deformed to a desired shape. At Step 2, the polymer is cooled down to a temperature below T_{trans} , while maintaining the initial deformation constraint. At Step 3, the deformation constraint is removed and the temporary shape is fixed. At Step 4, as heating back to a temperature above T_{trans} , the polymer recovers into its permanent (initial) shape. Steps 1-3 are also referred to as the programming step and Step 4 is the recovery step. For certain applications where the shape recovery is important, Step 4 is under a free recovery condition, where the initial deformation constraint is removed during heating.

In the design of SMP applications, theoretical models are desired to predict the behaviors of targeted design. In the past, several models (Chen and Lagoudas, 2008a, b, Ge,Luo, et al., 2012, Liu, et al., 2006, Nguyen, et al., 2008, Qi, et al., 2008a, Srivastava, et al., 2010) were developed and most of them were used to predict the comprehensive behaviors of SMPs under three-dimension finite deformation. For example, recently, Westbrook et al. (Ge,Luo, et al., 2012) developed a model that considers finite deformation stress-strain behaviors (including yielding, post-yielding, and rate dependency), constrained recovery behaviors and free recovery behaviors. Because of the complicated thermo-mechanical properties of SMPs, it is not a surprise that these models involve a large number of material parameters (typically 20-30). In order to obtain these parameters, one has to conduct a series of experiments, some of which are time-consuming. For example, one has to conduct uniaxial experiments at several distinctive temperatures and strain rates; free recovery experiments have to be conducted and each of them could take about 4 to 8 hours, depending on the temperature rate used. After the experiments, material parameter fitting is also time-consuming as most of these models contain ~20-30 parameters. Finally, these models are only useful to design engineers when they are implemented into finite element codes. Certainly, once all these time-consuming works are completed, one can conduct high fidelity analysis to improve designs. However, for many engineers, an estimation of key features of shape

memory behaviors, such as free recovery time, can be very helpful, especially at the early stage of a material development or a device design. Such an estimation should be based on a simple model containing a limited amount of material parameters that can be easily identified experimentally. To our best knowledge, no such a model is currently available. This paper takes a first step toward this direction and provides a simple model to predict the temperature dependent free recovery behavior of SMPs. This model is based on a modified standard linear solid (SLS) model with Kohlrausch-Williams-Watts (KWW) stretched exponential function and requires only eight parameters that can be determined by stress relaxation tests. This paper is arranged in the following order: section 2 introduces materials synthesis, experiments including stress relaxation tests, and free recovery experiments; section 3 presents the modified standard linear solid model incorporating KWW stretched relaxation; in section 4, parameter identification, model predictions and parametric studies are introduced; finally, conclusions are made in section 5.

2. Materials and experiments

2.1 Materials

SMPs were synthesized following Yakacki et al. (2007) (Yakacki, et al., 2007). Briefly, tert-butyl acrylate (tBA) monomer and crosslinker poly (ethylene glycol) dimethacrylate (PEGDMA) were mixed according to a pre-calculated ratio, and 2,2-dimethoxy-2-phenylacetophenone was added as photoinitiator. The polymer solution was injected between two glass slides or into a glass tube, which then was placed under the UV lamp for polymerization. After 10 min, the SMP material was removed from the glass slides or tube and put into an oven for 1 hour at 80˚C. The SMP materials were machined into the proper shapes for different experiments, which include stress relaxation test and free recovery test.

2.2 Stress relaxations

Stress relaxations were conducted by using a Dynamic Mechanical Analysis (DMA) tester (TA Instruments, DMA Q800). A rectangular sheet with a dimension of 9.35mm×2.42mm×0.9mm was used for tests. Stress relaxation tests were performed at 13 different temperatures evenly distributed from 15 ℃ to 45 ℃ with 2.5 ℃ interval. The sample was preloaded by 1×10^{-3}N force to maintain the straightness. After reaching the testing temperature, it was allowed 30 min for the thermal equilibrium. Then a 1% strain was applied to the sample and the relaxation modulus was measured within 30 minutes. Fig. 48 shows the results of stress relaxation under 13 different temperatures. Base on the well-known time temperature superposition principle (TTSP) (Brinson, 2007, Rubinstein and Colby, 2003), a relaxation master curve at 27.5 ℃ can be constructed by shifting relaxation curves with shifting factors at different temperatures. The relaxation master curve and shifting factors are reported in section 4.

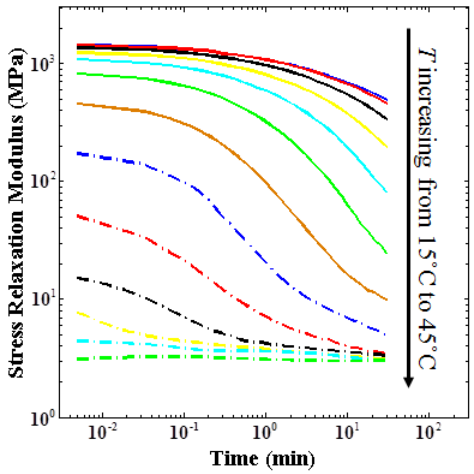

Fig. 48 Stress relaxations at temperatures varying from 15 ℃ to 45 ℃ with 2.5 ℃ interval.

2.3 Free recovery tests with ramping temperature

Free recovery tests were designed to validate the model and were not used for model parameter identification. The cylindrical specimens (10 mm diameter and 10 mm height) were tested using a MTS Universal Materials Testing Machine (Model Insight 10) equipped with a

customized thermal chamber (Thermcraft, Model LBO). The tests were conducted following the four-step thermo-mechanical shape memory cycle described above and were presented in detail in Westbrook et al. [25]. At the programming temperature T_{H1} (40 ℃), the specimen was initially compressed by 20% at a strain rate of 0.01/s. The specimen was then allowed 10 min to relax before being cooled to the shape fixing temperature T_L (20 ℃) at a linear rate of 2.5 ℃/min. Since the temperature rate was low, it was estimated that the temperature distribution in the sample was uniform. Once T_L was reached, the specimen was held for one hour then the compressive constraint was removed. During the free recovery, the temperature was increased to a high temperature T_{H2} at the same rate of cooling and once the temperature reached T_{H2}, the specimen recovered into its permanent shape. The shape (or strain) recovery in the specimen was measured using a laser extensometer (EIR, Model LE-05). Four high temperatures (T_{H2}) for free recovery were chosen as 30 ℃, 35 ℃, 40 ℃ and 50 ℃. The results of free recovery tests were plotted in section 4 for the comparison between model predictions and experiments.

3. Model description

As studied by Castro et al. (Castro, et al., 2010), a standard linear solid (SLS) model modified with Kohlrausch-Williams-Watts (KWW) stretched exponential relaxation can capture the SM behavior of an SMP. Below we use SLS-KWW model and seek an analytical solution for free recovery. We start with modeling the isothermal free recovery with the SLS model, then extend it to the nonisothermal case, and finally incorporate the KWW stretched exponential.

3.1 Isothermal free recovery

A standard linear solid model is used to describe the equilibrium and nonequilibrium behaviors of an SMP. As shown in Fig. 49, a linear spring with Young's modulus E_0 is used to represent the equilibrium behavior; for the nonequilibrium viscoelastic response, the spring with

Young's modulus E_1 is used to represent the elastic response and the dashpot with viscosity η represents the viscous behavior. The combination of spring and dashpot gives rise to a corresponding relaxation time $\tau = \eta / E_1$. The nonequilibrium branch is also referred to as Maxwell model with a stress relaxation modulus:

$$E(t) = E_1 \exp\left(-\frac{t}{\tau}\right). \tag{A1}$$

The total deformation is e_m and the deformation in the nonequilibrium branch can be decomposed into the elastic deformation e_e and the viscous deformation e_v .

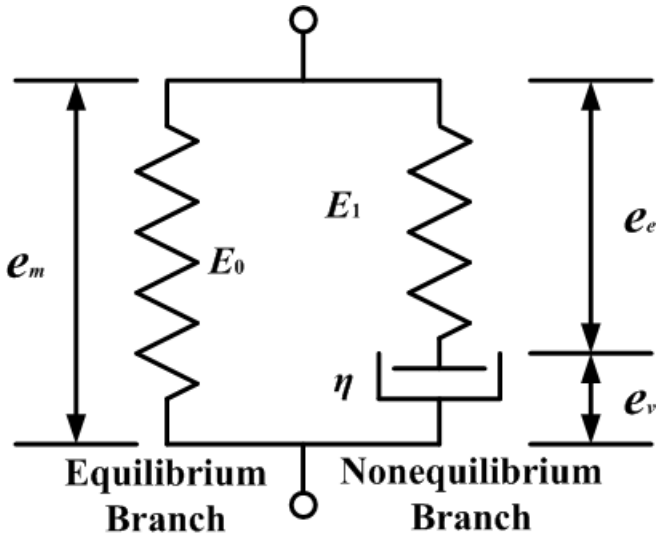

Fig. 49 A schematics of the standard linear solid model: a linear spring on the left with Young's modulus E_0 represents the equilibrium behavior; on the right, the nonequilibrium branch consists of a spring with Young's modulus E_1 representing the elastic response and a dashpot with viscosity η representing the viscous behavior.

During the free recovery, the total stress should be zero, i.e.

$$\sigma_{total} = \underset{Equilibrium}{E_0 e_m} + \underset{Nonequilibrium}{E_1 e_e} = 0 . \tag{A2}$$

From Eq. (A2), the relation between the total deformation e_m and the elastic deformation in the nonequilibrium branch e_e can be obtained as:

$$e_e = -\frac{E_0}{E_1} e_m . \tag{A3}$$

In addition, the deformations and deformation rates in each branch have the following relationship:

$$e_m = e_e + e_v , \tag{A4a}$$

$$\dot{e}_m = \dot{e}_e + \dot{e}_v . \tag{A4b}$$

In the nonequilibrium branch, the stress in the dashpot should be equal to the stress in the spring, i.e.

$$\underset{Dashpot}{E_1 \tau \dot{e}_v} = \underset{Spring}{E_1 e_e} . \tag{A5}$$

Combing Eq. (A3) and Eq. (A5), one finds,

$$\dot{e}_v = -\frac{E_0}{E_1 \tau} e_m . \tag{A6}$$

Considering Eq. (A3), Eq. (A4b) and Eq. (A6), one obtains,

$$\frac{de_m}{e_m} = -\frac{E_0}{E_1 \tau}\left(1 + \frac{E_0}{E_1}\right)^{-1} dt . \tag{A7}$$

We denote the total deformation at the beginning of the free recovery as e^0 and the deformation during the free recovery as ζe^0, where $\zeta = e(t)/e^0 = 1 - r(t)$. $r(t)$ is the strain recovery ratio, and is defined as

$$r(t) = 1 - e(t)/e_{\max} , \tag{A8}$$

where $e_{\max}$ is the strain measured at the beginning of the free recovery step and $e(t)$ is the instantaneous strain during the free recovery. $r(t)$ was originally proposed by Lendlein and Langer (Lendlein and Langer, 2002) to quantify the amount of the initial fixed deformation that is recovered during a free recovery test.

Integrating of Eq. (A7) on both sides, it follows:

$$\int_{e^0}^{\zeta e^0} \frac{de_m}{e_m} = -\int_0^t \frac{E_0}{E_1 \tau}\left(1+\frac{E_0}{E_1}\right)^{-1} dt\,. \tag{A9}$$

Solving Eq. (9), one has the relation between t and ζ:

$$\ln \zeta = -\frac{t}{\tau}\frac{E_0}{E_1}\left(1+\frac{E_1}{E_0}\right)^{-1}. \tag{A10}$$

3.2 Nonisothermal free recovery

During the nonisothermal free recovery, the SMP is heated at a rate of Q ℃/min from a low temperature T_L. After t min, the temperature is $T = T_L + Qt$. Note here, we assuming the heating rate to be low and therefore the temperature distribution is uniform within the sample. Under the nonisothermal condition, the relaxation time (or viscosity) of the SMP strongly depends on temperatures. For a rheologically simple polymer, this variation should follow the time temperature superposition principle (TTSP) with a shifting factor:

$$\tau(T) = a_T(T)\tau_0\,, \tag{A11}$$

where τ_0 is a reference relaxation time. It was found that depending on whether temperature is above and near or below T_g, the shifting factor a_T can be calculated by two different methods (O'Connell and McKenna, 1999). For temperature above and near T_g, the WLF (Williams-Landel-Ferry) equation (Williams, et al., 1955) is used:

$$\log a_T = -\frac{C_1\left(T - T_r\right)}{C_2 + \left(T - T_r\right)}, \tag{A12}$$

where C_1 and C_2 are material constants, and T_r is a reference temperature. For the temperatures below T_g, an Arrhenius-type behavior developed by Di Marzio and Yang et al. (1997) (Di Marzio and Yang, 1997) is used:

$$\ln a_T = -\frac{AF_C}{k}\left(\frac{1}{T} - \frac{1}{T_r}\right), \tag{A13}$$

where A is material constant, F_c is the configuration energy and k is Boltzmann's constant.

Considering Eq. (A9) and Eqs. (A11)-(A13), for the temperatures below T_r (or $T_L + Qt \le T_r$), one have:

$$\int_{e^0}^{\zeta e^0} \frac{de_m}{e_m} = -\frac{E_0}{E_1\tau_0}\left(1 + \frac{E_0}{E_1}\right)^{-1} \int_0^t \exp\left[\frac{AF_c}{k_b}\left(\frac{1}{T_L + Qt} - \frac{1}{T_r}\right)\right] dt\,. \tag{A14a}$$

As the temperature is raised above T_r (or $T_L + Qt > T_r$), one have

$$\int_{e^0}^{\zeta e^0} \frac{de_m}{e_m} = -\frac{E_0}{E_1\tau_0}\left(1 + \frac{E_0}{E_1}\right)^{-1} \left\{ \int_0^{\frac{T_r - T_L}{Q}} \exp\left[\frac{AF_c}{k_b}\left(\frac{1}{T_L + Qt} - \frac{1}{T_r}\right)\right] dt + \int_{\frac{T_r - T_L}{Q}}^t 10^{\frac{C_1\left(T_L + Qt - T_r\right)}{C_2 + \left(T_L + Qt - T_r\right)}} dt \right\}. \tag{A14b}$$

Therefore, the relation between t and ζ becomes, for the temperatures below T_r,

$$\ln \zeta = -\frac{E_0}{E_1\tau_0}\left(1 + \frac{E_0}{E_1}\right)^{-1} \int_0^t \exp\left[\frac{AF_c}{k_b}\left(\frac{1}{T_L + Qt} - \frac{1}{T_r}\right)\right] dt\,, \tag{A15a}$$

and for the temperatures above T_r,

$$\ln\zeta = -\frac{E_0}{E_1\tau_0}\left(1+\frac{E_0}{E_1}\right)^{-1}\left\{\int_0^{\frac{T_r-T_L}{Q}}\exp\left[\frac{AF_c}{k_b}\left(\frac{1}{T_L+Qt}-\frac{1}{T_r}\right)\right]dt+\int_{\frac{T_r-T_L}{Q}}^{t}10^{\frac{C_1\left(T_L+Qt-T_r\right)}{C_2+\left(T_L+Qt-T_r\right)}}dt\right\}. \quad \text{(A15b)}$$

3.3 KWW stretched exponential

In most polymers, the relaxation behavior is non-symmetrical, non-exponential, non-Debye process, which cannot be captured by a single exponential function described by Eq. (A1) (Alvarez, et al., 1991, Lindsey and Patterson, 1980, Svanberg, 2003). The well-known Kohlrausch, Williams and Watts (KWW) (Williams and Watts, 1970) stretch exponential function is most popular and widely used to describe stress relaxation in polymers. In the KWW model, the parameter β ($0<\beta\le 1$) is used to 'stretch' the stress relaxation time. The exact origin of this stretched exponential relaxation behaviors in glass-forming systems remain unclear. It is often viewed as a consequence of the dynamic heterogeneity of the system, meaning that the stretching behavior is caused by the distribution of a series single exponential relaxation processes. However, studies have also shown that such a stretching behavior could be intrinsic to certain relaxation processes. (Angell, et al., 2000, Phillips, 1996)

Regardless of the physical origin, the stress relaxation modulus in Eq. (A1) can be rewritten as:

$$E\left(t\right)=E_1\exp\left[-\left(\frac{t}{\tau}\right)^{\beta}\right]. \quad \text{(A16a)}$$

Eq. (A16a) can also be interpreted as a regular relaxation in the stretched time space t' with the time mapping of $t'=t^{\beta}$. This new time space is also called material clock (Caruthers, et al., 2004,

McKenna, 1989). Eq. (A16a) then recovers into a simple exponential relaxation behavior in the material clock t' :

$$E(t) = E_1 \exp\left[-\frac{t'}{\tau'}\right], \tag{A16b}$$

where $\tau' = \tau^{\beta}$. It can be shown that Eq. (A10) is also valid in the material clock:

$$\frac{de_m}{e_m} = -\frac{E_0}{E_1\tau'}\left(1+\frac{E_0}{E_1}\right)^{-1} dt' . \tag{A17}$$

Since $t' = t^{\beta}$, dt' with $dt' = \beta t^{\beta-1}dt$. Eq. (A17) becomes:

$$\frac{de_m}{e_m} = -\frac{E_0}{E_1\tau^{\beta}}\left(1+\frac{E_0}{E_1}\right)^{-1} \beta t^{\beta-1}dt . \tag{A18}$$

When a SMP is under the isothermal free recovery, the relation between the recovery ratio and time is:

$$\ln\zeta = -\frac{E_0}{E_1}\left(1+\frac{E_0}{E_1}\right)^{-1} \beta\int_0^t \frac{1}{\tau^{\beta}} t^{\beta-1}dt . \tag{A19}$$

When a SMP is under the nonisothermal free recovery, for temperatures below T_r , the relation between the recovery ratio and time is:

$$\ln\zeta = -\frac{E_0}{E_1}\left(1+\frac{E_0}{E_1}\right)^{-1} \frac{\beta}{\tau_0^{\beta}}\int_0^t \exp\left[\frac{AF_c}{k_b}\left(\frac{1}{T_L+Qt}-\frac{1}{T_r}\right)\right] t^{\beta-1}dt ; \tag{A20a}$$

For temperatures above T_r , the relation between t and ζ becomes:

$$\ln\zeta = -\frac{E_0}{E_1}\left(1+\frac{E_0}{E_1}\right)^{-1} \frac{\beta}{\tau_0^{\beta}}\left\{\int_0^{\frac{T_r-T_L}{Q}} \exp\left[\frac{AF_c}{k_b}\left(\frac{1}{T_L+Qt}-\frac{1}{T_r}\right)\right] t^{\beta-1}dt + \int_{\frac{T_r-T_L}{Q}}^t 10^{\frac{C_1(T_L+Qt-T_r)}{C_2+(T_L+Qt-T_r)}} t^{\beta-1}dt\right\}. \tag{A20b}$$

4. Results and discussion

4.1 Parameter identification

In Eq. (A20a) and Eq. (A20b), which are used to predict free recovery behaviors, there are eight parameters in total and they are listed in Table 7. All of them are determined by stress relaxation tests. Base on the time-temperature superposition principle, a relaxation master curve at 27.5℃ (Fig. 50a) can be constructed by shifting individual relaxation curves in Fig. 48 with shifting factors at different temperatures (Fig. 50b) (Brinson, 2007, Rubinstein and Colby, 2003). The mater relaxation curve can be described by a modified standard linear solid model with KWW stretch exponential, where the stress relaxation modulus is:

$$E(t) = E_0 + E_1 \exp\left[-\left(\frac{t}{\tau_0}\right)^{\beta}\right]. \tag{A21}$$

In Eq. (A21), at time $t = 0$, $E(0) = E_0 + E_1$, and as t approaches ∞, $E(\infty) = E_0$. From Fig. 50a, we have $E_0 = 3.5\text{MPa}$ ($E(\infty)$) and $E_1 = 1420\text{MPa}$ ($E(0) - E_0$). Using Eq. (A21) to fit the stress relaxation master curve at 27.5℃, parameters τ_0 and β are determined as 2.5sec and 0.6, respectively. The model fitting of the stress relaxation can be improved better by introducing one simple exponential branch (or Maxwell branch). However, by introducing this additional branch, it is impossible to make the relatively simple solution in the form Eq. (A20b). As introduced in Section 3.2, the shifting factor as a function of temperature can be described by WLF and Arrhenius equations at different temperature ranges. In Fig. 50b, by fitting shifting factors with these two equations, parameters in Eq. (A12) and (A13) are determined as C_1=51.6, C_2=17.44, T_r=27.5℃ and AF_c/k=-40000. Compared with a reported similar model (Castro, et al., 2010), parameters identified by stress relaxation tests are in the range of those in the reported paper.

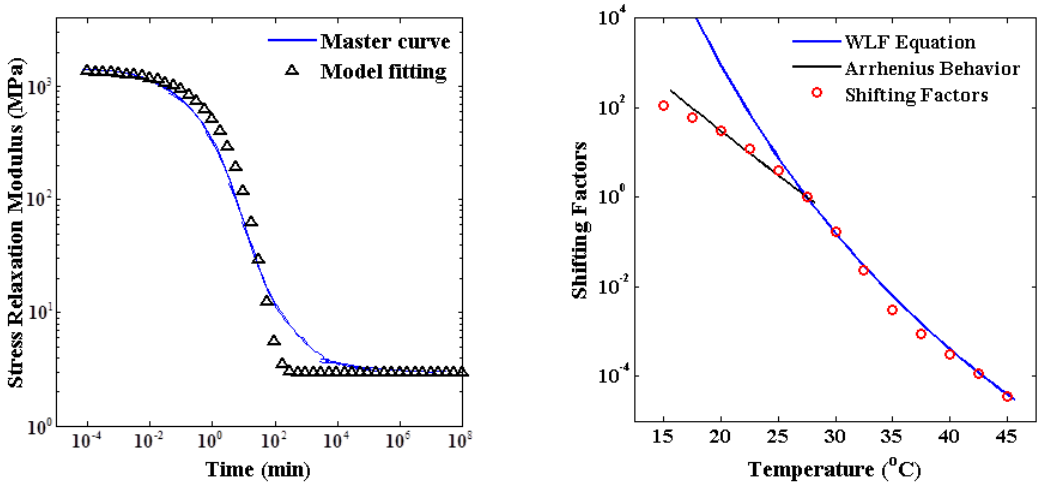

(a) (b)

Fig. 50 Parameter fitting for stress relaxation. (a) The stress relaxation master curve at 27.5 ℃. (b) The shifting factors with temperature.

Table 7 Parameters for model prediction

Parameter	Value	Description
E_0	3.5MPa	Elastic modulus in equilibrium branch
E_1	1420MPa	Elastic modulus in nonequilibrium branch
β	0.6	KWW stretching parameter
τ_0	2.5s	Relaxation time at reference temperature
T_r	27.5°C	Reference temperature
C_1	17.44	Parameter for WLF equation
C_2	51.6°C	Parameter for WLF equation
AF_c/k_b	–40000K	Pre-exponential parameter for the Arrhenius-Type behavior

4.2 Model predictions for free recovery behaviors

Fig. 51 shows the nonisothermal free recovery behaviors from experiments introduced in Section 2. The strain recovery ratio $r(t)$ defined in Eq. (A8) was used to characterize free recovery behaviors. Clearly, the recovery rate and degree of recovery are faster and larger at higher recovery temperatures.

Using parameters in Table 7, the model is able to predict free recovery behaviors. Fig. 51 shows the comparison between model predictions and experiments for free recovery behaviors. Overall, the model is able to predict the recovery time under different recovery temperatures and

model predictions show good agreement with experiments. The recovery rate in predictions is slightly higher than the one in experiments, especially at T_{H2}=30 ℃ and 35 ℃. The main reason for this error is that in the stress relaxation fitting in Fig. 50a, the modulus in the model fitting is relaxed faster than the experimental data.

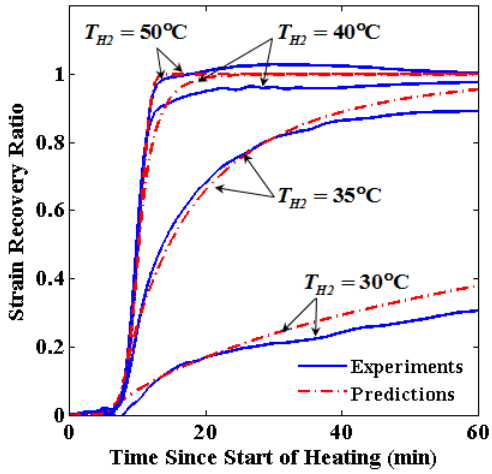

Fig. 51 Comparison between experiments for free recovery.

The model also predicts free recovery behaviors under infinite heating rate, where temperatures instantaneously reach recovery temperatures. This represents the fastest recovery a SMP can achieve. Here, in order to compare the recovery rates, we define the recovery time as the time needed for 95% of recovery. In Fig. 52, for $T_{H2} = 50°C$, the recovery time is 5 seconds. For $T_{H2} = 40°C$, it takes ~2.5 min to recover. For $T_{H2} = 35°C$, the recovery time is extended to ~36 min. For $T_{H2} = 30°C$, it needs ~908 min (15.1 hours) to recover, as the recovery temperature is close to T_g.

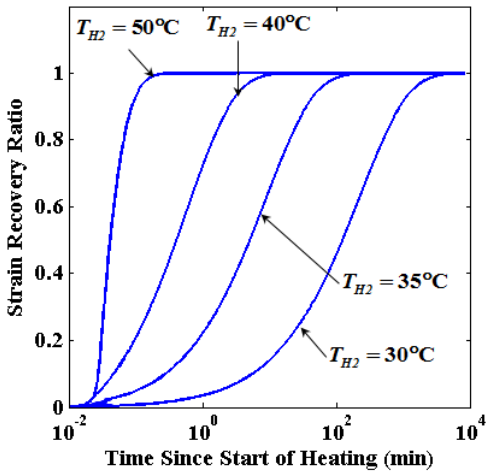

Fig. 52 Model predictions for free recovery behaviors under infinite heating rate.

4.3 Parametric study

In some SMP applications, such as cardiovascular stents (Yakacki, et al., 2007), recovery time is an important feature of SMPs, as the faster it recovers, the shorter time an operation takes and the less pain patients suffer. Here, parametric studies are explored using the model to investigate how to improve the recovery time by changing material properties. All of these predictions are under infinite heating rate with the recovery temperature of $T_{H2}=35°C$. In Fig. 53, the recovery time is decreased by increasing the equilibrium modulus (E_0), or KWW stretching parameter (β), or decreasing the nonequilibrium modulus (E_1), or the relaxation time (τ_0). Table 2 gives the comparison of recovery time (the time needed for the 95% recovery) by changing material parameters by the same percentages. As indicated in the table, the recovery is more sensitive to β rather than other parameters. When $\beta=0.6$, the recovery time is 36min. If β is reduced by 40% to $\beta=0.36$, the recovery time is 83.8 days. If β is increased by 60% to $\beta=0.96$, the recovery time is only 2.5sec.

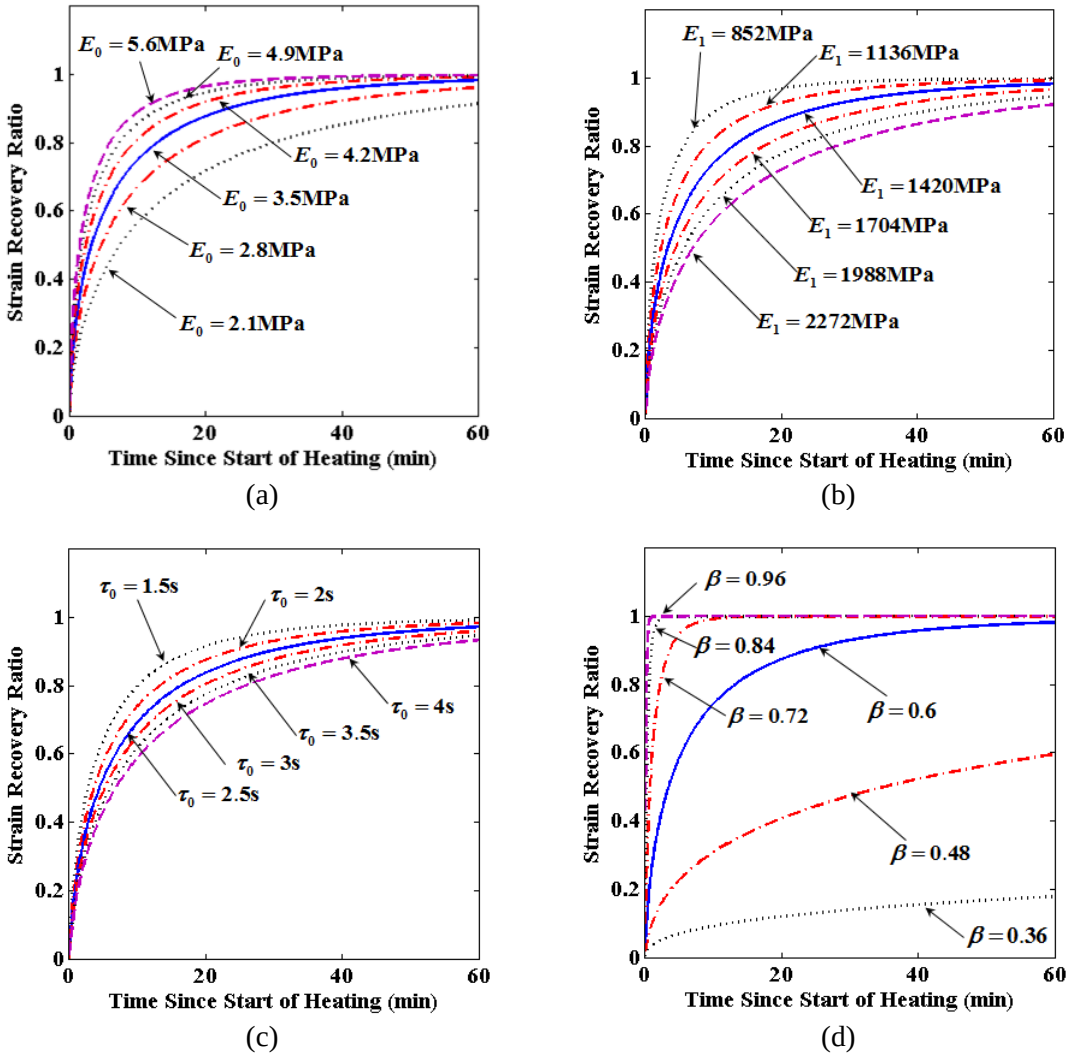

Fig. 53 Predictions for free recovery at 35 ℃ with different material parameters. (a) By changing E_0. (b) By changing E_1. (c) By changing τ_0. (d) By changing β.

Table 8 Free recovery time with different material parameters. In each case, only one parameter was varied to the percentage indicated in the table whilst the rest of the parameters were the same as those in Table 7.

Parameters	60%	80%	100%	120%	140%	160%
E_0	83.6 min	52 min	36 min	26.7 min	20.7 min	16.6 min
E_1	15.5 min	24.8 min	36 min	48.6 min	62.7 min	78.2 min
τ	21.6 min	28.7 min	36 min	42.9 min	50.1 min	57.2 min
β	83.8 days	708 min	36 min	5 min	1.2 min	2.5 s

Above findings provide valuable insights on controlling the free recovery of a given SMP by tuning materials properties. For example, both E_0 and E_1 can be controlled via the choices of monomer and crosslinkers as well as their molar ratios. As shown by the WLF and Arrhenius relationships, the relaxation time at a given temperature depends strongly on the T_g of the SMP, which can be controlled via the formulations of the SMPs. Lastly, the KWW exponent β can also be synthetically controlled. For polymers, it is known that β characterizes the distribution of the relaxation processes, and is thus related to the heterogeneity (both structurally and dynamically) of the polymer. For example, the network structures of thiolene-based SMPs are much more homogenous than that of the (meth) acrylate-based SMPs, because of their unique free-radical-mediated step-growth polymerization mechanism (Hoyle and Bowman, 2010). By mixing thiolene with (meth) acrylate monomers, systematical variations in β can be achieved.

5. Conclusion

In this paper, a modified standard linear solid model with KWW stretched relaxation exponential is used to obtain an analytical solution for capturing the nonisothermal free recovery behaviors of SMP. This solution requires only eight parameters that can be obtained from stress relaxation experiments. The theoretical predictions of free recovery behavior show a good agreement with experimental results for an acrylate-based SMP. Parametric studies using this solution reveal that the free recovery time can be reduced by increasing the equilibrium modulus (E_0) or KWW stretching parameter (β), or by decreasing the nonequilibrium modulus (E_1) or the relaxation time (τ_0) and is most sensitive to the KWW stretching parameter β.

APPENDIX B

THERMOMECHANICAL BEHAVIORS OF A TWO-WAY SHAPE MEMORY COMPOSITE ACTUATOR

1. Introduction

Shape memory polymers (SMPs) are a class of emerging smart materials, which are capable of fixing their temporary shape and recovering their permanent shape in response to environmental stimulus such as temperature (Di Marzio and Yang, 1997, Ge,Luo, et al., 2012, Ge,Yu, et al., 2012, Lendlein and Kelch, 2002, 2005, Lendlein and Langer, 2002, Liu, et al., 2007, Nguyen, et al., 2008, O'Connell and McKenna, 1999, Qi, et al., 2008a, Westbrook, et al., 2011, Williams, et al., 1955, Xie, 2010, Xie, et al., 2009), light (Jiang, et al., 2006, Koerner, et al., 2004, Lendlein, et al., 2005, Li, et al., 2003, Long, et al., 2009, Rickert, et al., 2002, Scott, et al., 2006, Scott, et al., 2005, Thomas and Lendlein, 2002, Westbrook,Castro, et al., 2010), moisture (Huang, et al., 2005) or magnetic field (Mohr, et al., 2006). SMPs can be further categorized as one-way SMPs (1W-SMPs) and two-way SMPs (2W-SMPs), based on whether the actuation is reversible or not. In the first kind, the transition from the temporary shape to the permanent shape cannot be reversed by simply reversing the stimulus, or in order to achieve the temporary shape again after recovery, a new programming step is necessary. In the second kind, the transition between the temporary shape and the permanent shape is reversible. Both one-way shape memory (1W-SM) effect and two-way shape memory (2W-SM) effect can find their applications. However, from material processing and fabrication point of view, it is relatively more difficult to achieve the 2W-SM effect. Several attempts were made in the past to achieve a free-standing 2W-SM effect by developing a SMP composite such as a polymeric laminate developed by Tamagawa (Tamagawa, 2010); a bilayer polymeric laminate was introduced by Chen et al. (Chen, et al., 2010, Chen, et al., 2008). Recently, Chung reported a SMP, poly(cyclooctene) (PCO), which is capable of exhibiting both 1W- and 2W-SM effects (Chung, et al., 2008). However, in order to achieve the 2W-SM

effect, a constant load (such as a dead weight) has to be applied to assist the reversible actuation. In typical SMP applications, it might not be desirable to apply a constant external load to achieve the 2W-SM effect. To overcome this disadvantage, we developed a PCO based composite actuator that demonstrated a nonlinear reversible actuation under the temperature stimulus (Bellin, et al., 2006). This composite was fabricated by embedding a PCO strip in its pre-stretched temporary shape into an elastomer matrix. Upon a heating and cooling cycle, the composite actuator could be actuated from a straight shape to a bent shape, and then be returned to its straight shape. Fig. 1a shows the actuation during a heating-cooling cycle and Fig. 54b shows the transverse displacement of the end of the composite actuator as a function of temperatures. In Fig. 54b, there are three key features of the free-standing 2W-SM effect: 1) the actuation is a highly nonlinear function of temperatures with a large hysteresis loop. 2) The training cycle of heating-cooling leads to an actuation different from other cycles. After the training cycle, the amount of actuation is stabilized to a smaller actuation. 3) During heating, the actuator first moves in a direction opposite to the actuation direction then moves back along the actuation direction.

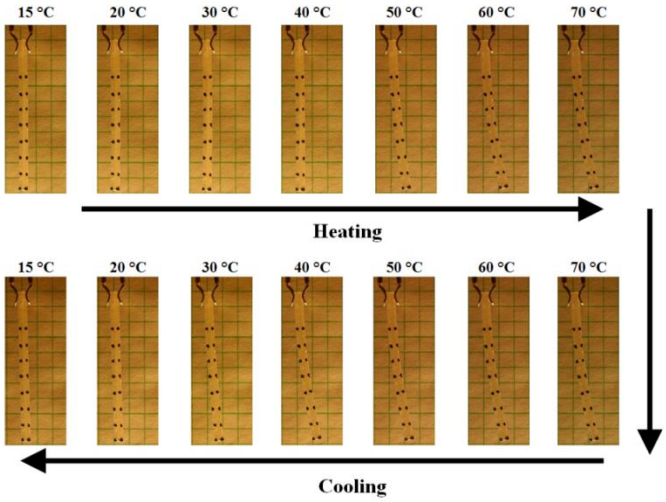

(a)

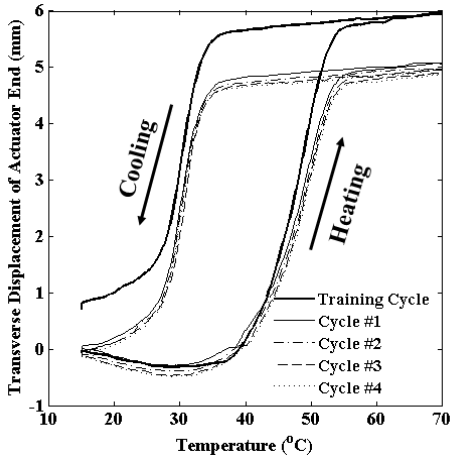

(b)

Fig. 54 An actuation during a heating-cooling cycle: (a) the actuation shows the free-standing 2W-SM effects; (b) transverse displacement of the actuator end for five thermal cycles (Bellin, et al., 2006).

The goal of this paper is to theoretically investigate the thermomechanical behaviors of this 2W-SMP composite actuator and the mechanisms for the observed phenomena during the actuation cycles, and to provide insight into how to improve designs. The paper is arranged in the following manner. In section 2, materials and fabrication for the actuator are briefly introduced, and the thermomechanical behavior for the PCO SMP is presented. In section 3, the existing thermomechanical constitutive model for the PCO SMP is reviewed. The model for the actuator is developed in section 4 by integrating the constitutive models for the PCO SMP into a laminate composite theory. In section 5, predictions from the analytic model are presented and the characterization of actuator is analyzed. Several parametric studies such as effects of width ratio, modulus of the matrix and programming stress are discussed.

2. Materials and experiments

2.1 Materials

The programmed 2W-SMP serving as a strip embedded into the matrix. The 2W-SMP was synthesized by using Poly(cyclooctene) (PCO) (Evonik-Degussa Corporation, Vestenamer

8012 with a trans content of 80% and dicumyl peroxide (DCP) (>98% purity, Aldrich). Details about the preparation of the sample were discussed by Chung et al (Chung, et al., 2008).

Fig. 55a shows the 1W-SM effect for PCO: the sample was stretched by an external load (700kPa) at T_H (here $T_H = 70°C$). Then, the temperature decreased from T_H to T_L (here $T_L = 15°C$), while the external load was maintained. After unloading at T_L, PCO was capable of staying at the temporary shape. Finally, the sample recovered the permanent shape as being heated back from T_L to T_H (Chung, et al., 2008, Westbrook,Parakh, et al., 2010). The 2W-SM effect can be achieved essentially by following the same steps as those in 1W-SM effect, except that the external load was maintained during heating. The actuation strain $R_{act}(T)$, which was used to characterize the 2W-SM effect, is defined as:

$$R_{act}(T) = \frac{L(T) - L(T_H)}{L(T_H)}, \tag{B1}$$

where $L(T_H)$ is the length of the sample at T_H, L is the length as temperature varies. Fig. 55b shows $R_{act}(T)$ temperature plot for 2W-SM behaviors of PCO under three different external loads (500 kPa, 600 kPa and 700 kPa). During cooling, at the temperature above ~35 ℃, the actuation strain increases almost linearly at a relatively small slope. At the temperature between ~35 ℃ to ~30 ℃, the actuation strain increases dramatically during crystallization. At the temperature below ~30 ℃, the actuation strain saturates to ~25%. The magnitude of the actuation strain strongly depends on external load, i.e., higher external load results in higher actuation strain. During heating, at the temperature below ~50 ℃, the actuation strain increases slightly. At the temperature between ~50 ℃ to ~55 ℃, the actuation strain decreases dramatically due to melting of crystalline phase. Finally, at the temperature above ~55 ℃, the actuation strain decreases at a relatively small slope similar to that of cooling first region's slope (Chung, et al., 2008, Westbrook,Parakh, et al., 2010).

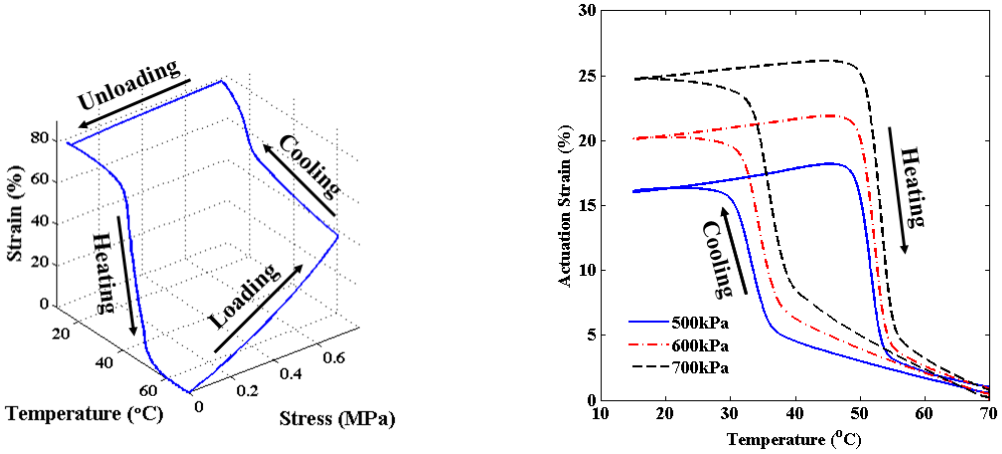

(a) (b)

Fig. 55 PCO exhibits both 1W- and 2W-SM behaviors: (a) Stress-Temperature-Strain plot for 1W-SM behavior under an external load 700 kPa. (b) Actuation Strain-Temperature plot for 2W-SM behaviors under three different external loads (Chung, et al., 2008, Westbrook,Parakh, et al., 2010).

An acrylate-based polymer was chosen as the matrix for the actuator. It was synthesized by 55 wt% poly(ethylene glycol) dimethacrylate (PEGDMA), $M_n = 750$ (PEGDMA 750, Aldrich) and 45 wt% tert-butyl acrylate (tBA) (98% purity, Aldrich) and 2,2-dimethoxy-2-phenylacetophenone (99% Purity, Aldrich) was added as the photoinitiator. The glass transition temperature of this polymer is $T_g = -10°C$, below the temperature range of the actuator heating-cooling cycle (15˚C~70˚C). Details were introduced by Ortega et al. (Ortega, et al., 2008).

2.2 Actuator fabrication and characterization

The polymer composite actuator was fabricated by using PCO and PEGDMA. The details of fabrication were provided in Westbrook, et al. (Bellin, et al., 2006). Briefly, the PCO strip was first programmed into a stretched shape under a stress of 700 kPa at 70 ℃, followed by cooling to T_L =15 ℃ then unloading. The programmed PCO strip was immediately placed into an aluminum mold. After sealing the mold by two glass slides, the PEGDMA solution was injected into the

mold using a syringe. After polymerization and curing, the composite material was removed from the mold and sectioned into the required actuator dimensions.

The actuator characterization experiments followed five heating-cooling cycles with each cycle as the following: first, the temperature was held constant at $T_L = 15°C$ for 5 min and then heated to T_H =70 ℃ at a rate of 2 ℃/min. Once T_H was reached, the temperature was held constant at T_H for 10 min and then cooled to T_L at a rate of 2 ℃/min. Lastly, the temperature was held constant at T_L for an additional 5 min. The results of the characterization experiments were presented in introduction (Fig. 54).

3. Constitutive models for PCO and PEGDMA

3.1 Constitutive model for the 2W-SMP

The constitutive model for the PCO SMP to capture both 1W- and 2W-SM behaviors was studied by Westbrook (Westbrook,Parakh, et al., 2010). A brief review of this model is provided below.

3.1.1 Mechanics for the PCO SMP

PCO is a crystalizable crosslinking polymer. Therefore, it is assumed that the PCO is a mixture of a rubbery phase and a crystalline phase. The volume fraction of each phase is determined by the instantaneous temperature, deformation, and corresponding rate and history. A simple large deformation elasticity model is adopted by assuming that both the rubbery phase and the crystalline phase follow the similar form of stress-strain behavior:

$$\sigma_R(\lambda_R) = N_R kT \ln \lambda_R,\ \sigma_C(\lambda_C) = \mu \ln \lambda_C, \tag{B2}$$

where the subscript ‘R’ and ’C’ represent the rubbery phase and the crystalline phase, respectively. N_R is the cross-link density, k is Boltzmann’s constant and T is the absolute

temperature. $N_{\mathrm{R}}kT$ gives the shear modulus for the rubbery phase of 2W-SMP and μ is the shear modulus for the crystalline phase. λ is the stretch ratio, and $\ln\lambda$ is the Hencky strain, which is used as it conveniently converts the multiplication of stretches into additive strains and thus simplifies the work of tracking deformation in individual crystalline phases (Westbrook,Parakh, et al., 2010). It should be noted that the stretch in the rubbery phase λ_{R} generally is different from the stretch in the crystalline phase λ_{C}.

Assuming that the thermomechanical loading starts at a high temperature, at time $t=0$, PCO consists of 100% rubbery phase. If a certain load $\sigma_{\mathrm{total}}^{0}$ applied to 2W-SMP, the rubbery phase should deform by λ_{R}^{0}, therefore:

$$\sigma_{\mathrm{total}}^{0}=\sigma_{\mathrm{R}}\left(\lambda_{\mathrm{R}}^{0}\right). \tag{B3}$$

As the temperature is lowered to below crystallization temperature, crystallization starts. Since polymer crystallization is a relatively slow and continuous process, one important assumption is that when a small fraction of polymer crystals is formed, it is in a stress-free state (Long, et al., 2010). This stress-free state for newly formed crystalline phases was referred as natural configuration by Rajagapol (Rajagopal and Srinivasa, 1998a, b). In the case PCO, this evolution of polymer crystal phase also affects the mechanical deformation and is attributed to underlying mechanism for the 2W SM effect. More details about effects of crystal phase evolution on the mechanics were discussed by Westbrook (Westbrook,Parakh, et al., 2010). By considering the volume fractions of the rubbery phase and individual crystalline phase formed at different times, the total stress at time t becomes:

$$\sigma_{\mathrm{total}}^{m}=\left(1-f_{m}\right)\sigma_{\mathrm{R}}\left(\lambda_{\mathrm{R}}^{m}\right)+\sum_{i=1}^{m}\left[\Delta f_{i}\sigma_{\mathrm{C}}\left(\lambda_{i}^{m}\right)\right], \tag{B4}$$

where $f_{m}=\sum_{i=1}^{m}\Delta f_{i}$. Note that Eq. (B4) can also be applied to the case where there is no new crystalline phase forms by simply setting $\Delta f_{i}=0$.

During heating, the existing crystalline phases start to melt and recover to the rubbery state. At time $t = t_m + \Delta t$, it is assumed that the last formed crystalline phase with Δf_{m_e} melts. Concurrently to melting, a small deformation $\Delta\lambda_{\text{melt}}^{1}$ is induced . Following the same assumption for mechanical deformation during crystallization, at time $t = t_m + n\Delta t$,(t_m is the time when melting starts) the crystalline phase with volume fraction Δf_{m_e-n+1} melts and the deformation is induced by $\Delta\lambda_{\text{melt}}^{n}$. The total stress is:

$$\sigma_{\text{total}}^{n} = \left(1 - f_{m_e-n}\right)\sigma_{\text{R}}\left[\left(\sum_{k=1}^{n}\Delta\lambda_{\text{melt}}^{k}\right)\lambda_{\text{R}}^{m_e}\right] + \sum_{i=1}^{m_e-n}\left\{\Delta f_i\sigma_{\text{C}}\left[\left(\sum_{k=1}^{n}\Delta\lambda_{\text{melt}}^{k}\right)\lambda_{i}^{m_e}\right]\right\}, \tag{B5}$$

where $f_{m_e-n} = \sum_{i=1}^{m_e-n}\Delta f_i$.

3.1.2 Thermal expansion coefficient

Westbrook (2010) presented the effective coefficient of thermal expansion (CTE) at time $t = t_c + m\Delta t$:

$$\alpha^{m}(T) = \left(1 - \sum_{i=1}^{m}\Delta f_i\right)\alpha_{\text{R}} + \sum_{i=1}^{m}\Delta f_i\alpha_{\text{C}} + \alpha_{\text{tran}}\frac{\Delta f_i}{\Delta T^{m}}, \tag{B6}$$

where α_{R} is the CTE of the rubbery phase, α_{C} is the CTE of the crystalline phase, and α_{tran} is the volume expansion ratio during phase transition from the rubbery phase to the crystalline phase; ΔT^{m} is the temperature increment at the m-th time increment. Thus, the thermal strain of 2W-SMP at time $t = t_c + m\Delta t$ is:

$$\varepsilon_T = \sum_{i=1}^{m}\alpha^{i}(T)\Delta T^{i} . \tag{B7}$$

3.1.3 Evolution rule for the 2W-SMP

Westbrook (2010) introduced the evolution rule for the 2W-SMP, based on Avrami's phase transition theory modified by Gent (Westbrook,Parakh, et al., 2010). Crystallization occurs after the temperature is lower than the crystallization temperature T_c and the crystallization rate is:

$$\dot{f}_c = k_c\left(f_\infty - f\right)\left(T_c - T\right)\left(\lambda - \lambda_{crit}\right), \text{ if } (T < T_c \text{ and } \lambda > \lambda_{crit}), \tag{B8}$$

where f is the volume fraction of the crystalline phase, k_c is the crystallization efficiency factor and f_∞ is the saturated volume fraction. Similar to the melting process, melting starts as the temperature above the melting temperature and the melting rate is:

$$\dot{f}_m = k_m f\left(T - T_m\right), \text{ if } (T > T_m), \tag{B9}$$

where k_m is the melting efficiency factor. The total rate of crystalline formation is:

$$\dot{f} = \dot{f}_c - \dot{f}_m. \tag{B10}$$

More details about the evolution rule were presented by Westbrook (Westbrook,Parakh, et al., 2010).

3.2 Constitutive model for the matrix material

For the sake of simplicity, the matrix material follows the same stress-strain behavior with the 2W-SMP rubbery phase:

$$\sigma_{Ma}\left(\lambda_{Ma}\right) = N_{Ma}kT\ln\lambda_{Ma} \tag{B11}$$

where N_{Ma} is the cross-link density and $N_{Ma}kT$ is the shear modulus for PEGDMA.

The thermal strain of the matrix material follows:

$$\varepsilon_{MaT} = \alpha_{Ma}\left(T - T_H\right) \tag{B12}$$

where α_{Ma} is CTE for the matrix material.

4. Model for the 2W-SMP composite actuator

In this section, the model for the actuator is developed by integrating the constitutive models for the 2W-SMP into a laminate composite theory. For the sake of simplicity, heat transfer is not considered in this case and we assume the temperature is uniformly distributed inside and outside the actuator. This is a close approximation as the actuator is generally thin.

4.1 Geometry

The actuator is treated as a laminate. Fig. 56a shows the dimensions of the cross section of the actuator (dimensions listed in Table. 9). The xy plane passes through the middle of the 2W-SMP strip where the z-coordinate defines the thickness. The top surface is z_1 and the bottom is $-z_2$, so $z_1 = h_T + h_2/2$, $z_2 = h_B + h_2/2$ and $z_1 + z_2 = h_1$. Based on the Euler-Bernoulli beam theory, taking the strain at $z = 0$ is ε_o ($\varepsilon(0) = \varepsilon_o$), the strain due to bending along the z-axis follows:

$$\varepsilon(z) = \varepsilon_o + \kappa \cdot z \tag{B13}$$

where κ is the curvature of the beam (Fig. 56b). It is emphasized here that $z = 0$ is not the neutral axis and ε_o is not necessary to be zero. During actuation, the strain due to bending is generally small ($\varepsilon < 1.5\%$), which is proved by the simulation shown later. Therefore, during actuation, we approximate the Hencky strain equal to the engineering strain and in Eq. (B13), the engineering strain ε is replaced by the Hencky strain:

$$\ln\lambda(z) = \ln\lambda_o + \kappa \cdot z, \tag{B14}$$

where λ_o is the stretch in the xy plane and $\lambda(z)$ is the stretch along z-axis. Eq. (B15) helps to unify the strain description in the 2W-SMP and the incremental strain during actuation. The transverse displacement d is related the curvature of the actuator during bending through the relationship:

$$d = \left[1 - \cos(L\kappa)\right]/\kappa \tag{B15}$$

where L is the length of the actuator and listed in Table 9.

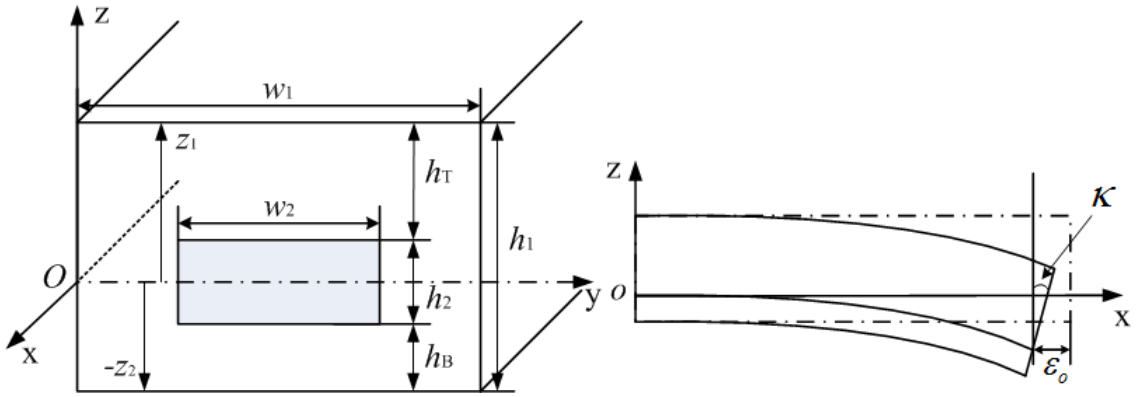

(a) (b)

Fig. 56 The geometry of the actuator: (a) dimensions of the cross section. (b) The schematic of the bending of the actuator.

Table 9. Dimensions of the cross section of the actuator

Parameter	Value	Description
Actuator		
h_1	2.76mm	Thickness
w_1	4.85mm	Width
L	46.73mm	Length
Embedded PCO Specimen		
h_2	0.81mm	Thickness
w_2	1.72mm	Width
h_B	0.63mm	Offset

4.2 Analysis during actuation

In this section, deformations during actuation including deformations on the 2W-SMP strip and the matrix are analyzed. We first investigate the material points on the xy plane ($z = 0$). For portions out of the xy plane, the Hencky strain follows Eq. (B14). Therefore, in following, if it is not noted, all stretches and stresses discussed are those in the xy plane.

Before actuation, since the 2W-SMP strip is embedded under a load free condition, based on Eq. **Error! Reference source not found.**, the total stress on the 2W-SMP strip is:

$$\sigma_{\text{total}}^{\text{A}} = \left(1 - f_{\infty}\right)\sigma_{\text{R}}\left(\lambda_{\text{R}}^{\text{A}_0}\right) + \sum_{i=1}^{m_e}\left[\Delta f_i \sigma_{\text{C}}\left(\lambda_i^{\text{A}_0}\right)\right] = 0, \tag{B16}$$

where $f_{\infty} = \sum_{i=1}^{m_e} \Delta f_i$, $\lambda_{\text{R}}^{\text{A}_0}$ is the strain in rubbery phase and $\lambda_i^{\text{A}_0}$ the strain in the crystalline phase formed at $t = t_{\text{c}} + i\Delta t$.

During actuation, raising the temperature to above the melting temperature triggers the shape recovery of the 2W-SMP strip, which tends to contract. However, due to the existence of the matrix, the contraction of the 2W-SMP strip is constrained. Considering thermal expansion, the deformation on the 2W-SMP strip can be decomposed into:

I. The mechanical deformation λ_{SM} (Fig. 57), which gives rise to stress acting on the 2W-SMP strip.

II. The thermal expansion λ_{T}, where $\lambda_{\text{T}} = 1 + \varepsilon_{\text{T}}$ and $\lambda_{\text{T}} = 1$ at $T_{\text{L}} = 15°\text{C}$ (Fig. 57).

Therefore, at time $t = t_{\text{A}} + n\Delta t$ during actuation, for the portion of the 2W-SMP in the xy plane, the total deformation including programing is $\lambda_{\text{T}}^n \lambda_{\text{SM}}^n \lambda_{\text{R}}^{\text{A}_0}$ and the total stress is:

$$\sigma_{\text{total}}^{\text{A}\to n} = \left(1 - f_{m_e - n}\right)\sigma_{\text{R}}\left(\lambda_{\text{SM}}^n \lambda_{\text{R}}^{\text{A}_0}\right) + \sum_{i=1}^{m_e - n}\left[\Delta f_i \sigma_{\text{C}}\left(\lambda_{\text{SM}}^n \lambda_i^{\text{A}_0}\right)\right], \tag{B17}$$

where $f_{m_e - n} = \sum_{i=1}^{m_e - n} \Delta f_i$. For the portion of the 2W-SMP out of the xy plane, the total stress is:

$$\sigma_{\text{total}}^{\text{A}\to n}(z) = \left(1 - f_{m_e - n}\right)\sigma_{\text{R}}\left[\lambda_{\text{SM}}^n(z)\lambda_{\text{R}}^{\text{A}_0}\right] + \sum_{i=1}^{m_e - n}\left\{\Delta f_i \sigma_{\text{C}}\left[\lambda_{\text{SM}}^n(z)\lambda_i^{\text{A}_0}\right]\right\}, \tag{B18}$$

where $\lambda_{\text{SM}}^n(z)$ follows Eq. (B14):

$$\ln \lambda_{\text{SM}}^n(z) = \ln \lambda_{\text{SM}}^n + \kappa \cdot z \tag{B19}$$

In the matrix, as it constrains the recovery of the 2W-SMP strip, it is pulled back by the 2W-SMP strip with λ_{Ma}^n correspondingly and the stress on the matrix should be:

$$\sigma_{\text{Ma}}^{\text{A}\to n} = \sigma_{\text{Ma}}\left(\lambda_{\text{Ma}}^n\right). \tag{B20}$$

For portions out of the xy plane, based on Eq. (B14), the Hencky strain of the matrix follows:

$$\ln \lambda_{\mathrm{Ma}}^{n}(z) = \ln \lambda_{\mathrm{Ma}}^{n} + \kappa \cdot z \,. \tag{B21}$$

By adding the thermal expansion of the matrix $\lambda_{\mathrm{MaT}}^{n}$, the total strain of the matrix is $\lambda_{\mathrm{MaT}}^{n}\lambda_{\mathrm{Ma}}^{n}$ (in Fig. 57), and $\lambda_{\mathrm{MaT}}^{n} = 1 + \varepsilon_{\mathrm{MaT}}^{n}$, $\lambda_{\mathrm{MaT}}^{n} = 1$ at $T_{\mathrm{L}} = 15°\mathrm{C}$.

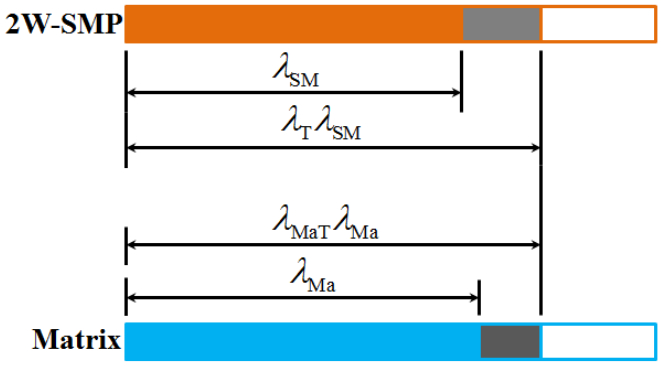

Fig. 57 Schematic of deformations of the actuator: the brown bar represents the 2W-SMP strip and the blue bar represents the matrix. Before actuation, the 2W-SMP strip and the matrix have the same length. During actuation, the deformation of the 2W-SMP strip can be decomposed into the mechanical deformation λ_{SM} due to the SM effect and the constraint from the matrix, and the thermal deformation λ_{T}, and the deformation of the matrix could be decomposed into the mechanical deformation λ_{Ma} stretched by the 2W-SMP strip and the thermal expansion λ_{MaT}. Considering the geometric compatibility, the 2W-SMP strip and the matrix should still have the same length, that is $\lambda_{\mathrm{T}}\lambda_{\mathrm{SM}} = \lambda_{\mathrm{MaT}}\lambda_{\mathrm{Ma}}$.

Considering the geometric compatibility, in the xy plane, the length of the 2W-SMP strip should be always equal to the length of matrix (Fig. 57). Therefore, during actuation, the deformation on the 2W-SMP strip should be equal to the deformation on the matrix (Fig. 57):

$$\lambda_{\mathrm{T}}\lambda_{\mathrm{SM}} = \lambda_{\mathrm{MaT}}\lambda_{\mathrm{Ma}} \,. \tag{B22}$$

According to Eq. (B22), the Hencky strain of the matrix in the xy plane can be calculated directly as following:

$$\ln \lambda_{\mathrm{Ma}} = \ln\left(\lambda_{\mathrm{T}}\lambda_{\mathrm{SM}}\right) - \ln \lambda_{\mathrm{MaT}} \,. \tag{B23}$$

Based on Eq. (B21) and Eq. (B23), any Hencky strain on the matrix along z-axis is:

$$\ln \lambda_{\mathrm{Ma}}(z) = \ln\left(\lambda_{\mathrm{T}}\lambda_{\mathrm{SM}}\right) - \ln \lambda_{\mathrm{MaT}} + \kappa \cdot z\,. \tag{B23}$$

4.3 Solutions

During actuation, there is no external load and moment applied to the actuator. Therefore, at $t = t_{\mathrm{A}} + n\Delta t$, we have:

$$\begin{aligned} \mathrm{F}_{\mathrm{total}}^{\mathrm{A}\to n} &= \mathrm{F}_{\mathrm{S}}^{\mathrm{A}\to n} + \mathrm{F}_{\mathrm{Ma}}^{\mathrm{A}\to n} = 0, \\ \mathrm{M}_{\mathrm{total}}^{\mathrm{A}\to n} &= \mathrm{M}_{\mathrm{S}}^{\mathrm{A}\to n} + \mathrm{M}_{\mathrm{Ma}}^{\mathrm{A}\to n} = 0, \end{aligned} \tag{B25}$$

where $\mathrm{F}_{\mathrm{S}}^{\mathrm{A}\to n}$ and $\mathrm{F}_{\mathrm{Ma}}^{\mathrm{A}\to n}$ are the forces acting on the cross section of the 2W-SMP strip and the matrix, respectively:

$$\begin{aligned} \mathrm{F}_{\mathrm{S}}^{\mathrm{A}\to n} &= w_2 \int_{-\frac{h_2}{2}}^{\frac{h_2}{2}} \sigma_{\mathrm{total}}^{\mathrm{A}\to n}\left(\lambda_{\mathrm{SM}}^{n}, \kappa, z\right) dz, \\ \mathrm{F}_{\mathrm{Ma}}^{\mathrm{A}\to n} &= w_1 \int_{-z_2}^{z_1} \sigma_{\mathrm{Ma}}^{\mathrm{A}\to n}\left(\lambda_{\mathrm{Ma}}^{n}, \kappa, z\right) dz - w_2 \int_{-\frac{h_2}{2}}^{-\frac{h_2}{2}} \sigma_{\mathrm{Ma}}^{\mathrm{A}\to n}\left(\lambda_{\mathrm{Ma}}^{n}, \kappa, z\right) dz, \end{aligned} \tag{B26}$$

$\mathrm{M}_{\mathrm{S}}^{\mathrm{A}\to n}$ and $\mathrm{M}_{\mathrm{Ma}}^{\mathrm{A}\to n}$ are moments,

$$\begin{aligned} \mathrm{M}_{\mathrm{S}}^{\mathrm{A}\to n} &= w_2 \int_{-\frac{h_2}{2}}^{\frac{h_2}{2}} \sigma_{\mathrm{total}}^{\mathrm{A}\to n}\left(\lambda_{\mathrm{SM}}^{n}, \kappa, z\right) z dz, \\ \mathrm{M}_{\mathrm{Ma}}^{\mathrm{A}\to n} &= w_1 \int_{-z_2}^{z_1} \sigma_{\mathrm{Ma}}^{\mathrm{A}\to n}\left(\lambda_{\mathrm{Ma}}^{n}, \kappa, z\right) z dz - w_2 \int_{-\frac{h_2}{2}}^{-\frac{h_2}{2}} \sigma_{\mathrm{Ma}}^{\mathrm{A}\to n}\left(\lambda_{\mathrm{Ma}}^{n}, \kappa, z\right) z dz. \end{aligned} \tag{B27}$$

Totally, there are three unknown quantities: $\lambda_{\mathrm{SM}}^{n}$, $\lambda_{\mathrm{Ma}}^{n}$ and κ. They can be solved by Eq. (B21) and Eqs. (B25)-(B27).

5. Results

5.1 Prediction for the actuator characterization experiment

As κ is solved during heating-cooling actuation, based on Eq. (B15), the analytic model presents the transverse displacement varying with temperatures under five thermal cycles. In the model, there are 13 parameters in total (listed in Table 10), including 5 parameters for the thermomechanical behavior of the 2W-SMP (PCO), 6 parameters for the evolution rule of the 2W-SMP, and 2 parameters for the thermomechanical behavior of the matrix (PEGDMA). Parameters for 2W-SMP (PCO) are directly from Westbrook (Westbrook,Parakh, et al., 2010) and parameters for the matrix (PEGDMA) were identified by simple tests including uniaxial tension and stress free thermal expansion test. Fig. 58 presents the model prediction for the heating-cooling actuation cycles, which shows a good agreement with the experimental results.

Table 10 Parameters for Analytic Model

Description	Parameter	Value
Mechanical Behavior for the 2W-SMP (PCO)		
Polymer Crosslinking Density for Rubbery Phase	$N_R k$ (Pa/K)	4.7×10^{3}
Crystalline Phase Modulus	μ_c (MPa)	16
CTEs for the 2W-SMP (PCO)		
Rubbery Phase CTE	α_R ($^{\circ}C^{-1}$)	1×10^{-4}
Crystalline Phases CTE	α_C ($^{\circ}C^{-1}$)	5×10^{-4}
Phase transition volume expansion ration	α_{tran} ($^{\circ}C^{-1}$)	3×10^{-4}
Evolution Rule for the 2W-SMP (PCO)		
Crystallization Temperature	T_c ($^{\circ}C$)	42
Melting Temperature	T_m ($^{\circ}C$)	47
Volume Fraction at Time t=∞	f_∞ (-)	0.8
Critical Stretch for Crystalline Phase	λ_{crit} (-)	1.05
Crystallization Efficiency Factor	k_c (-)	1.0×10^{-3}
Melting Efficient Factor	k_m (-)	5.5×10^{-3}
Thermomechanical Behavior for the Matrix (PEGDMA)		
Polymer Crosslinking Density for the Matrix	$N_{Ma} k$ (Pa/K)	35.6×10^{3}
Matrix CTE	α_{Ma} ($^{\circ}C^{-1}$)	1×10^{-4}

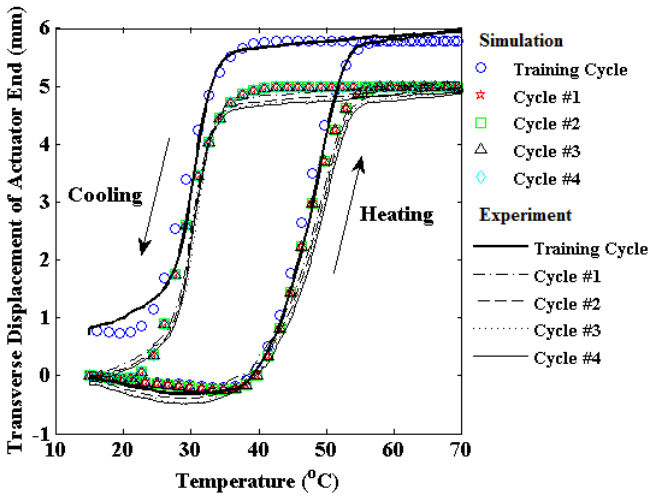

Fig. 58 Predictions for the heating-cooling actuation cycles.

The model successfully predicts three key features characterized in the Introduction. For the large hysteresis loop during actuation, this is attributed to the hysteresis of crystallization and melting for the 2W-SMP. For the actuation difference between the training cycle and others, it is essentially because of different loading histories on the 2W-SMP strip between the programming cycle and later cycles. In Fig. 59, in the programming step, a constant load (700kPa) was applied to achieve stretched shape ($\varepsilon = 95\%$, in Fig. 8a) during cooling. After unloading at $T_{\mathrm{L}} = 15°\mathrm{C}$, the stretched 2W-SMP strip returned to 73.95% (Fig. 60b) and the strip was immediately placed into an aluminum mold for the actuator fabrication. Therefore, at the beginning of the training cycle, the strain on the 2W-SMP strip was 73.95%. During heating in the training cycle, the constrained recovery of the 2W-SMP strip (from 73.95% to 72.85% in Fig. 60b) led to the bending of the actuator. During cooling in the training cycle, the crystallization was triggered as the temperature below crystallization temperature. Differently from the programming cycle, however, the stress acted on the 2W-SMP strip was maintained by the matrix, therefore was a variable with temperature (Fig. 59) and dependent on the actuator bending. As a result, the strain of the 2W-SMP strip was 73.79% at the end of the train cycle (in Fig. 60). Therefore, the strain at the beginning of the first cycle is 73.79%, which is different from the one at the beginning of the

training cycle (73.95%). For the opposite moving at the early stage during heat, where the melting of the 2W-SMP does not start, based on Eq. **Error! Reference source not found.**, the effective CTE is $4.2\times10^{-4}/℃$, which is higher than the CTE of the matrix material ($1\times10^{-4}/℃$). Thus, PCO strip expands more than the matrix, which leads the actuator to bend to the opposite direction to the actuation(Fig. 61b). Once melting starts, the SM effect leads the 2W-SMP strip to contract and the actuator bends to the positive direction (Fig. 9c).

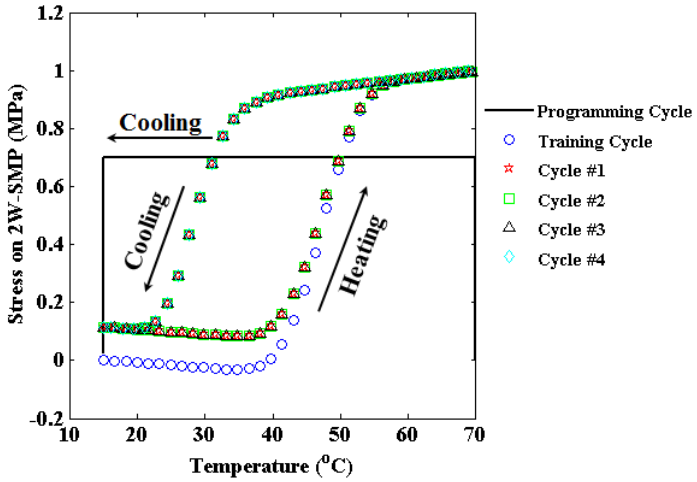

Fig. 59 Stress vs temperature on the 2W-SMP strip during actuation including programming

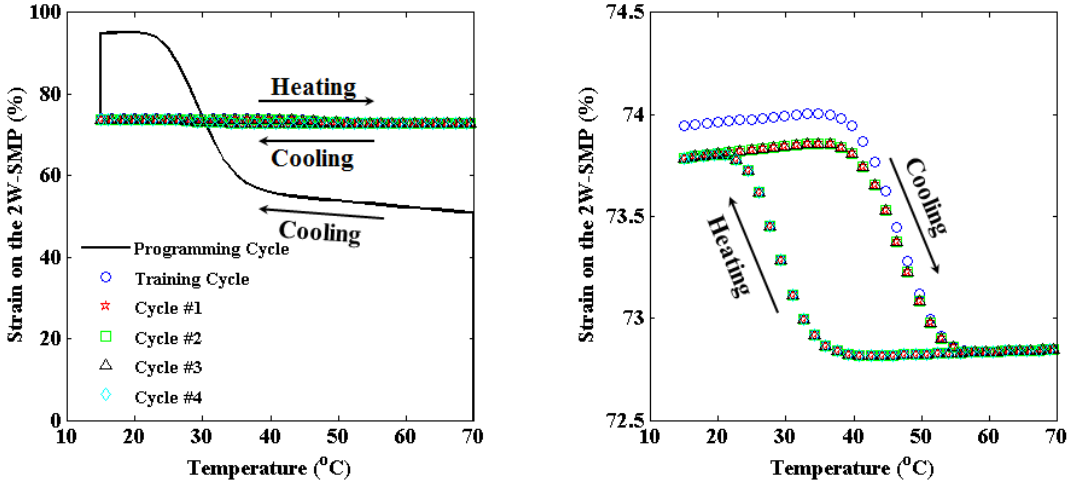

(a) (b)

Fig. 60 Strain on the 2W-SMP strip during programming and actuation: (a) including programming; (b) during actuation.

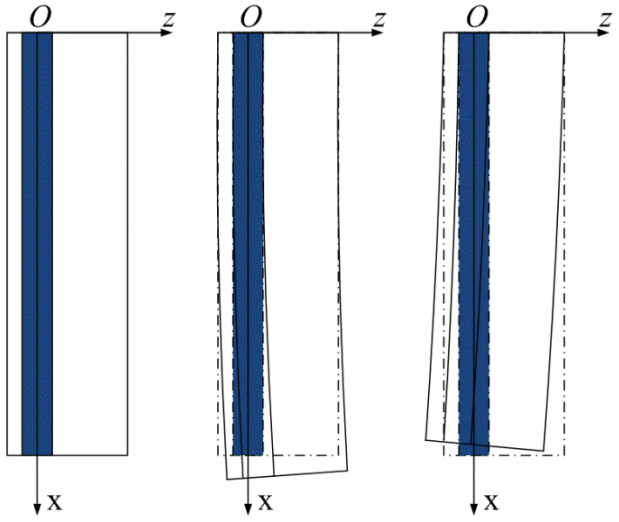

(a) (b) (c)

Fig. 61 Schematics of actuation (blue strip inside is the 2W-SMP strip and the white part around is the matrix): (a) original position of the actuator; (b) when the 2W-SMP strip expands more than the matrix, it is defined that the actuator bends to the "negative" direction; (c) as the 2W-SMP strip contracts due to the SM effect, it is defined that the actuator bends to the "positive" direction.

5.2 Parametric studies

The model provides also a good tool to explore the actuator design space which is constrained by the mold geometry, programming and fabrication. In general, the maximum transverse displacement can be improved by reducing the actuator width, using softer matrix material or increasing the programming stress.

In Fig. 62, the 3D plots show the normalized transverse displacement at $T_{\mathrm{H}} = 70°\mathrm{C}$ varies with modulus of the matrix (E_{Ma} from 5MPa to 15MPa) and the programming stress (σ_{P} from 500kPa to 2000kPa) under three different width ratios (R_w=2, 2.82 and 4. Here, $R_w = w_1/w_2$). It clearly shows that the transverse displacement at 70 ℃ is enhanced by decreasing the width ratio, choosing softer matrix and increasing the programming stress. However, in Fig. 62a, when the modulus of the matrix is close to 5MPa and the programming stress is larger than ~1700kPa, the transverse displacement is decreasing, instead of increasing, by increasing the programming stress.

Based on Eq. (B15), the maximum transverse displacement occurs at $\kappa_{\text{crit}} L = 0.74\pi$, where $\kappa_{\text{crit}} = 0.05\text{mm}^{-1}$. When κ is larger than κ_{crit}, the tip of the actuator bends back and the transverse displacement decreases when κ is still increasing. In other word, where the width ratio and the modulus of the matrix are low and the programming stress is high such as the case in Fig. 62a, the maximum transverse displacement does not occur at T_{H}, although the maximum κ does. When the width ratio is high enough such as the case in Fig. 62b and c, both the maximum transverse displacement and the maximum κ occur at T_{H}.

Fig. 63 shows the bending angle (κL) of the actuator under extreme conditions: low width ratio ($R_w = 2$), low modulus of the matrix ($E_{\text{Ma}} = 1 \sim 5\text{MPa}$) and high programming stress ($\sigma_{\text{P}} = 1500 \sim 2000\text{kPa}$). Similar tendency with the normalized transverse displacement, the increase of the programming stress results in increase of the bending angle under constant width ratio and modulus of the matrix; the decrease of the modulus leads to the increase of the bending angle under constant width ratio and programming stress. The green grid plane marks $\kappa L = 2\pi$, where the actuator curls a completely closed circle.

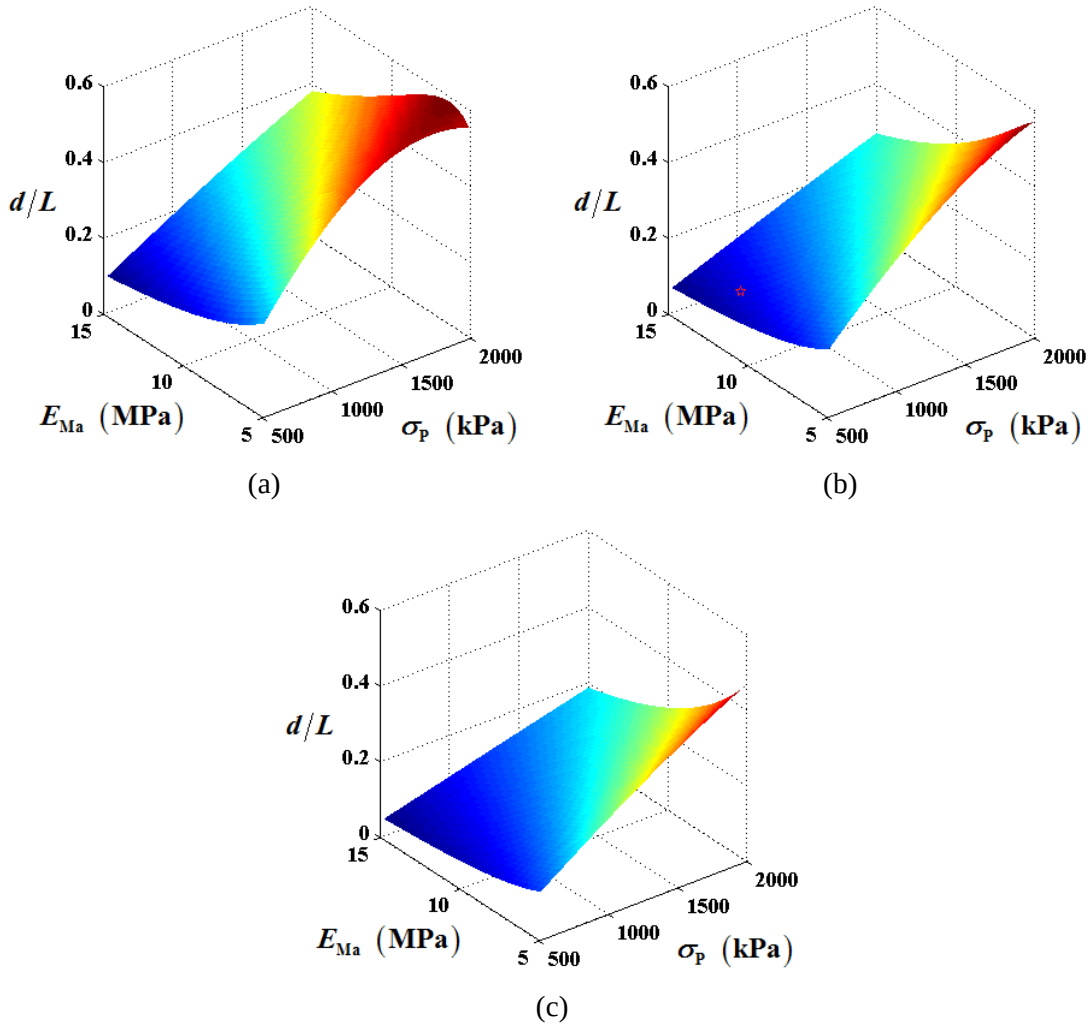

Fig. 62 3D plots showing the normalized transverse displacement (d/L) at 70˚C varying with modulus of the matrix (E_{Ma}) and the programming stress (σ_{P}) under three different width ratios: (a) $R_w = 2$; (b) $R_w = 2.82$, the red star represents the current actuator; (c) $R_w = 4$.

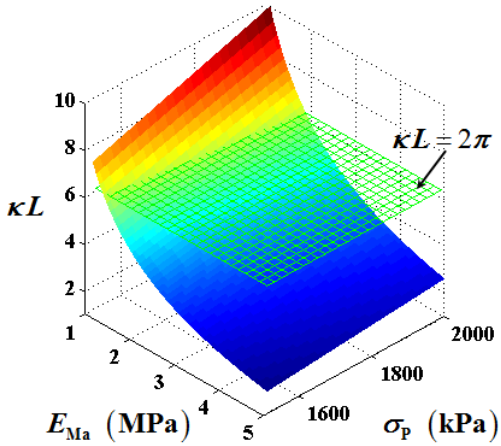

Figure 63. The bending angle (κL) of the actuator under extreme conditions ($R_w = 2$, $E_{Ma} = 1 \sim 5\text{MPa}$ and $\sigma_P = 1500 \sim 2000\text{kPa}$), where the green grid plane represents $\kappa L = 2\pi$ and the actuator curls a completely closed circle.

6. Conclusions

An analytic model for the free-standing polymer composite actuator is developed. The actuator consists of a programmed 2W-SMP strip embedded into a rubbery matrix. The actuation is triggered by the SM effect and the external load is provided by the bending of the matrix. In this paper, by taking advantage of existing constitutive for the 2W-SMP, an analytic model is built to solve a bending problem for the composite actuator during heating-cooling cycles. The model successfully captures actuation behaviors and helps better understand phenomena during actuation. As a good design tool, the model explores the actuator design space. The model quantitatively presents the increase of the maximum transverse displacement by reducing the actuator width, using softer matrix material or increasing the programming stress.